

Phantom fluid cosmology: Impact of a phantom hidden sector on cosmological observables

James M. Cline,¹ Matteo Puel,¹ Takashi Toma,^{2,3} and Qiu Shi Wang¹

¹*McGill University, Department of Physics, 3600 University Street, Montréal, QC H3A 2T8, Canada*

²*Institute of Liberal Arts and Science, Kanazawa University, Kanazawa, Ishikawa 920-1192 Japan*

³*Institute for Theoretical Physics, Kanazawa University, Kanazawa, Ishikawa 920-1192 Japan*

(Dated: November 7, 2023)

Phantom scalar theories are widely considered in cosmology, but rarely at the quantum level, where they give rise to negative-energy ghost particles. These cause decay of the vacuum into gravitons and photons, violating observational gamma-ray limits unless the ghosts are effective degrees of freedom with a cutoff Λ at the few-MeV scale. We update the constraints on this scale, finding that $\Lambda \lesssim 19$ MeV. We further explore the possible coupling of ghosts to a light, possibly massless, hidden sector particle, such as a sterile neutrino. Vacuum decays can then cause the dark matter density of the universe to grow at late times. The combined phantom plus dark matter fluid has an effective equation of state $w < -1$, and functions as a new source of dark energy. We derive constraints from cosmological observables on the rate of vacuum decay into such a phantom fluid. We find a mild preference for the ghost model over the standard cosmological one, and a modest amelioration of the Hubble and S_8 tensions.

CONTENTS

I. Introduction	1	C. Correlations between parameters	31
II. Constraint on Λ	2	1. Massless ν_s case	31
III. Ghost/dark matter models	3	2. Massive ν_s case	31
III.1. Gravitational coupling	3	References	32
III.2. Scalar or vector coupling	3		
III.3. Phantom sector spectra	4		
III.4. Phantom fluid evolution	5		
III.5. Constraints from type Ia Supernovae	7		
IV. CMB and large scale structure	9		
IV.1. Massless ν_s case	9		
IV.1.1. Method and Results	12		
IV.2. Massive ν_s case	13		
IV.2.1. Acoustic peak shift	14		
IV.2.2. Late ISW enhancement	15		
IV.2.3. Spatial curvature	15		
IV.2.4. Matter power spectrum	15		
IV.2.5. Results	16		
IV.3. Cosmological tensions	19		
V. Conclusions	20		
A. Computation of vacuum decay rate per unit volume	21		
B. Derivation of Boltzmann equations and hierarchies	23		
1. Relativistic sterile neutrinos	25		
a. Qualitative features of the perturbed massless equations	28		
2. Massive sterile neutrinos	29		

I. INTRODUCTION

Ghosts, or phantoms, are scalar fields with a wrong-sign kinetic term. They have been widely studied in cosmology, as a source of matter with equation of state $w < -1$, as was suggested in early determinations of the dark energy equation of state [1–4]. If such an object exists in nature, it must have not only classical behavior, but also quantum mechanical: negative energy particles which are the quanta of the ghost field.¹

Even if such exotic particles have no direct couplings to the standard model (SM), they cannot avoid being gravitationally coupled. As a result, through virtual graviton exchange, the vacuum is unstable to decay into pairs of ghosts plus positive-energy particles [5], and the rate for such processes is unbounded unless there is an ultraviolet cutoff Λ on the phase space of the ghosts: in other words, any consistent theory of ghosts must be a low-energy approximation that breaks down at momenta larger than Λ . Non-observation of excess gamma rays from vacuum decay leads to a bound that was roughly estimated as $\Lambda \lesssim 3$ MeV [6].

¹ They are unlike the Faddeev-Popov ghosts for fixing gauge symmetries in quantum field theory, which carry positive energy but with negative probability.

As pointed out in Ref. [6], the low-energy effective theory of ghosts must be Lorentz-violating, since Λ is a bound on the magnitude of the 3-momenta of the ghosts, which implies a preferred reference frame. Explicit, UV-complete models that give such a momentum cutoff were constructed in Refs. [7–9]. In the present work, we will not be concerned with the microphysics underlying such ghost models, but rather with the late-time cosmological implications of the low-energy effective theory.

Another possible signature of phantom theories could be decay of the vacuum into ghosts plus dark matter (DM). If both types of particles had the same dispersion relation, apart from the overall sign, there would be no net cosmological effect, at the homogeneous level, due to the cancellation of stress-energies of the two components. Here we will consider the case of massless ghosts, which can have a nonvanishing effect, since the negative-energy density of the ghosts redshifts faster than that of the created dark matter. The result is a net creation of DM at late times. We will show that for purely gravitationally coupled ghosts, this process is too slow to give detectable results. But it is consistent to couple the ghosts and the DM more strongly, for example by exchange of a heavy gauge boson, allowing for significant late-time DM creation.

In the present work, we examine the effect of such late-time DM creation on the cosmic microwave background (CMB) and structure formation. Even if the contributions of the two fluids cancel exactly at the homogeneous level, in the case of massless ghosts and massless sterile neutrinos, their perturbations do not cancel. This leads to constraints on the rate of DM plus phantom fluid creation, and consequently on the energy scale of new physics linking phantom particles to dark matter.

Unlike most previous studies, we are interested here in the quantum production of the phantom particles, rather than a classical field condensate. To keep these issues cleanly separated, we focus on the case of massless phantoms, whose potential vanishes. It is therefore consistent to neglect any phantom vacuum expectation value in the present work.

We start by revisiting the upper bound on Λ from diffuse gamma rays in Section II, and make a fully accurate determination. In Section III we describe the particle physics model for a phantom sector coupled to dark matter, and solve for the cosmological component densities created by decay of the vacuum. There we also derive preliminary constraints based on type Ia supernovae. In Section IV, the consequences for the CMB and large scale structure are studied using a full Monte Carlo search of the parameter space, resulting in an upper bound on the vacuum decay rate and corresponding new-physics energy scales. We investigate the potential of the model for providing a new source of dark energy, and for addressing various cosmological tensions. Conclusions are given in Section V.

II. CONSTRAINT ON Λ

In Ref. [6], a rough estimate was made of the rate for vacuum decay into ghosts and photons. Here we compute the rate more quantitatively. The computation is identical to that for gravitational scattering of ghosts into photons, $\phi\phi \rightarrow \gamma\gamma$, except that the initial state particles are treated as final state particles, and integrated over with momenta restricted by $|\vec{p}_i| \leq \Lambda$. The matrix element has been computed in Refs. [10, 11], and is given by ²

$$\sum_{\text{spin}} |\mathcal{M}|^2 = \frac{1}{8m_P^4} \left(\frac{tu}{s} \right)^2, \quad (1)$$

where the Mandelstam invariants are defined in the usual way, and we can pretend that the ghost energies are positive since the momentum-conserving delta function is $\delta(E_1 + E_2 - E_3 - E_4)$ where $E_{1,2}$ are ghost energies and $E_{3,4}$ are photon energies. Here $m_P = 2.43 \times 10^{18}$ GeV is the reduced Planck mass.

Carrying out the phase space integrals as described in appendix A, we first compute the instantaneous spectrum of gamma rays $d\Gamma/dE$. The result is shown as the black solid curve in Fig. 1. However the observed flux is a line-of-sight integral, similar to that for decaying dark matter [12], which can be expressed as an integral over the redshift of the corresponding emission distance,

$$\frac{dJ}{dE} = \frac{1}{4\pi} \int_1^\infty dz \frac{1}{H(z)(1+z)^3} \frac{d\Gamma}{dE}((1+z)E), \quad (2)$$

where the Hubble rate is $H(z) \cong H_0 \sqrt{\Omega_m(1+z)^3 + \Omega_\Lambda}$, ignoring the small contribution from radiation. Here $\Omega_m \simeq 0.32$ and $\Omega_\Lambda \simeq 0.68$ are the total matter and dark energy abundance, respectively. The result is shown as the red dashed curve in Fig. 1, in units of $\Lambda^7/(4\pi H_0 m_P^4)$. This must be compared to the observed diffuse electromagnetic spectrum, which in the region of interest was measured by the COMPTEL experiment [13] to be approximately $dJ/dE \cong 5.3 \times 10^{-3} (E/E_0)^{-2.4} \text{ MeV}^{-1} \text{ cm}^{-2} \text{ s}^{-1} \text{ sr}^{-1}$ with $E_0 = 1$ MeV. By demanding that the predicted flux in Eq. (2) not exceed the observed one, we derive a 95% Confidence Level (C.L.) limit of

$$\Lambda \lesssim 18.8 \text{ MeV}. \quad (3)$$

which is somewhat weaker than the rough estimate originally derived in Ref. [6]. Here we assumed the ghost particles are real scalars; the bound in Eq. (3) should be

² We use the interaction Lagrangian $\mathcal{L}_{\text{int}} = h_{\mu\nu} T^{\mu\nu}/(2m_P)$, where $h_{\mu\nu}$ is the graviton field and $T^{\mu\nu}$ is the total energy-momentum tensor, as done in Ref. [11]. This choice differs from the Lagrangian used in Ref. [10] by a factor of 1/2.

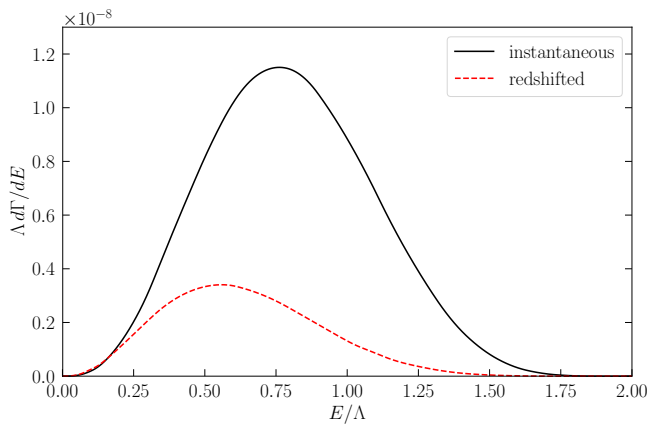


FIG. 1. Solid: Instantaneous photon spectrum ($\Lambda \times$ decay rate per unit volume and energy) from vacuum $\rightarrow \phi\phi\gamma\gamma$ (real scalar ghosts plus photons) decay, with units of Λ^8/m_P^4 . Dashed: Observed flux accounting for cosmological redshift, with units of $\Lambda^7/(4\pi H_0 m_P^4)$, as given by Eq. (2).

reduced by a factor $(1/2)^{1/9.4} \approx 0.93$ for complex scalar ghosts, giving $\Lambda \lesssim 17.5$ MeV.

We have also estimated the constraint arising from vacuum decay to ghosts and e^+e^- pairs; using the matrix elements computed in Ref. [11] (see Eq. (4) below), we find a decay rate per unit volume $\Gamma_d = \Lambda^8/(368640 \pi^5 m_P^4)$ in the approximation $m_e \ll \Lambda$. The present density of e^\pm is of order $n_e = \Gamma_d/H_0$, giving the rate $\Gamma_s \sim n_e \sigma$ for a CMB photon to scatter on e^\pm , with $\sigma \sim 8\pi\alpha^2/(3\Lambda^2)$. The probability to scatter is of order Γ_s/H_0 , which should be less than $\sim 10^{-4}$ [14]. This leads to a bound of $\Lambda \lesssim 350$ MeV, significantly weaker than Eq. (3).

III. GHOST/DARK MATTER MODELS

We next consider the decay of the vacuum into massless ghosts ϕ and massive hidden sector particles ν_s , which for definiteness is considered to be a sterile Dirac neutrino. (The main results are not expected to be sensitive to different possible choices, such as scalar dark matter.) Such a process can increase the energy density of the Universe at late times, due to the faster redshifting of the ghost versus the massive particle contribution.

III.1. Gravitational coupling

The matrix element for the gravitational scattering between Dirac fermions with mass m_{ν_s} and scalar particles is [11]

$$|\mathcal{M}_g|^2 = -\frac{(t - m_{\nu_s}^2)(s + t - m_{\nu_s}^2)(s + 2t - m_{\nu_s}^2)^2}{32 m_P^4 s^2}, \quad (4)$$

where the Mandelstam invariants s, t, u have their usual definitions, after changing $p_{1,2} \rightarrow -p_{1,2}$. The vacuum

decay rate, per unit volume, is given by the phase-space integral

$$\Gamma = (2\pi)^4 \int \prod_{i=1}^4 \frac{d^3 p_i}{(2\pi)^3 2E_i} \delta(E_1 + E_2 - E_3 - E_4) \times \delta^{(3)}(\vec{p}_1 + \vec{p}_2 - \vec{p}_3 - \vec{p}_4) |\mathcal{M}_g|^2, \quad (5)$$

where we have taken $p_{1,2} \rightarrow -p_{1,2}$, so that all energies are positive. The ghost momenta p_1 and p_2 should be integrated up to the cutoff Λ . In appendix A we carry out the numerical integration of the vacuum decay rate per unit volume. By numerically fitting, the result can be approximated as³

$$\Gamma_g \cong 4.4 \times 10^{-9} \frac{\Lambda^8}{m_P^4} \left[1 - \left(\frac{m_{\nu_s}}{\Lambda} \right)^2 \right] \exp[-5.3 \left(\frac{m_{\nu_s}}{\Lambda} \right)^{4.2}], \quad (6)$$

assuming the ghosts ϕ are real scalar particles, and that $m_{\nu_s} \leq \Lambda$ by energy conservation.

One can estimate the expected energy density in ν_s today following Ref. [6],

$$\rho_{\nu_s}(t_0) \sim \Lambda n_{\nu_s}(t_0) \sim \Lambda \Gamma_g t_0, \quad (7)$$

where $n_{\nu_s}(t)$ is the number density of sterile neutrinos and $t_0 \sim 1/H_0$ is the age of the Universe. Taking the maximum value $\Lambda \sim 19$ MeV and dividing by the critical density today ρ_{crit} , we find that $\Omega_{\nu_s} = \rho_{\nu_s}/\rho_{\text{crit}} \lesssim 10^{-9}$, which is far below the sensitivity of observational constraints. It follows that the vacuum decay rate must be ~ 9 orders of magnitude larger than that arising from purely gravitational interactions to have an observable cosmological impact.

III.2. Scalar or vector coupling

Since the gravitational interaction of ν_s is too weak to have appreciable cosmological effects, we introduce a heavy mediator coupling ϕ to ν_s , which can be either a scalar Φ or a vector Z' . Integrating out the mediator results in an effective interaction of the form

$$\frac{\Lambda}{M_s^2} |\phi|^2 \bar{\nu}_s \nu_s \quad \text{or} \quad \frac{i}{M_v^2} (\phi^* \overleftrightarrow{\partial}_\mu \phi) \bar{\nu}_s \gamma^\mu \nu_s, \quad (8)$$

where M_s and M_v are the new-physics mass scales, to be constrained.⁴ For simplicity, we take the ghost to be a complex scalar in both cases, and ν_s to be a Dirac fermion. This choice insures there is no gauge anomaly

³ In reality Γ_g falls to zero when $m_{\nu_s} \rightarrow \Lambda$ since the phase space vanishes, but the small discrepancy with Eq. (6) is numerically insignificant for our purposes.

⁴ The choice of parametrization for the scalar coupling strength is motivated by assuming that the dimensionful coupling of the scalar to ghosts will not exceed the cutoff Λ .

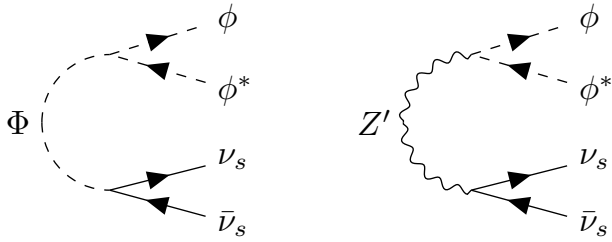


FIG. 2. Diagrams of vacuum decay mediated by a scalar Φ or a vector boson Z' .

for the vector mediator case. Figure 2 shows the Feynman diagrams of the vacuum decay processes.

Labeling the ghost momenta as $p_{1,2}$ and the ν_s momenta as $p_{3,4}$, we obtain the following new-physics matrix elements for the vacuum decay

$$|\mathcal{M}_n|^2 = \begin{cases} \frac{2\Lambda^2}{M_s^4} [s - 4m_{\nu_s}^2], & \text{scalar} \\ \frac{2}{M_s^4} [s^2 - (t - u)^2], & \text{vector} \end{cases}, \quad (9)$$

where again the Mandelstam invariants s, t, u have their usual definitions, after negating the 4-momenta of the ghosts so that kinematically they look like initial-state particles with positive energy. Integrating Eq. (5) numerically we find that the decay rate for both mediators can be approximately fit by the formulas⁵

$$\Gamma_n \cong 1.1 \times 10^{-5} \Lambda^8 \begin{cases} \frac{1}{M_s^4} \exp[-6.7 (\frac{m_{\nu_s}}{\Lambda})^{2.1}], & \text{scalar} \\ \frac{1}{M_s^4} \exp[-5.7 (\frac{m_{\nu_s}}{\Lambda})^{4.2}], & \text{vector} \end{cases}, \quad (10)$$

(see appendix A).

III.3. Phantom sector spectra

Once the massless ghosts ϕ and the massive sterile neutrinos ν_s are produced from the vacuum decay, their cosmological evolution is described by the Boltzmann equation in an expanding universe,

$$\frac{\partial f_i^0}{\partial t} - H p_i \frac{\partial f_i^0}{\partial p_i} = S_i, \quad (11)$$

where $p_i = |\vec{p}_i|$, t is the physical time, H is the Hubble parameter, $f_i^0(t, p_i)$ is the (dimensionless) phase-space distribution function and S_i is the collision or source term

for the species $i = \phi, \nu_s$, both at the homogeneous background level. The latter quantity is defined by [15]⁶

$$S_i = \frac{(2\pi)^4}{2E_i} \int \prod_{j \neq i}^4 \frac{d^3 p_j}{2E_j (2\pi)^3} \delta(E_1 + E_2 - E_3 - E_4) \times \delta^{(3)}(\vec{p}_1 + \vec{p}_2 - \vec{p}_3 - \vec{p}_4) |\mathcal{M}_n|^2 \mathcal{F}_0. \quad (12)$$

where we used the same labeling as in Eq. (5) (i.e., ghost energies are replaced by their absolute values), and

$$\mathcal{F}_0 = [1 + f_1^0(\vec{p}_1)] [1 + f_2^0(\vec{p}_2)] [1 - f_3^0(\vec{p}_3)] [1 - f_4^0(\vec{p}_4)] - f_1^0(\vec{p}_1) f_2^0(\vec{p}_2) f_3^0(\vec{p}_3) f_4^0(\vec{p}_4). \quad (13)$$

If the occupation number of the produced particles from the vacuum decay is small, namely $f_i^0 \ll 1$ (we will validate this assumption *a posteriori*), then $\mathcal{F}_0 \simeq 1$ and the collision term in Eq. (12) becomes independent of the phase-space distributions. This allows us to integrate Eq. (11) directly, obtaining [16, 17]

$$f_i^0(t, p_i) = \int_{t_{\text{in}}}^t dt' S_i\left(\frac{a(t)}{a(t')} p_i, t'\right) = \int_{a_{\text{in}}}^{a(t)} \frac{da'}{a' H(a')} S_i\left(\frac{a(t)}{a'} p_i, a'\right) \quad (14)$$

where t_{in} , or interchangeably the scale factor a_{in} , is the initial time of integration, and the factor $a(t)/a(t')$ accounts for the redshifting of the momenta between t' and t . We take $a_{\text{in}} \simeq 10^{-8}$ to be well deep inside the radiation era, when the vacuum decay is completely negligible; our results are insensitive to the precise value of a_{in} . We will compute the collision terms first.

The source term for the ghosts is relatively easy to evaluate, since the integrals over final-state particles have exactly the same form as for the cross section $\phi\phi \rightarrow \nu_s\nu_s$ of positive-energy massless ϕ particles. One can as usual perform this calculation in a Lorentz-invariant manner to obtain the cross section as a function of the Mandelstam variable $s = (p_1^\mu + p_2^\mu)^2 = 2p_1 p_2 (1 - \cos\theta)$, where θ is the angle between \vec{p}_1 and \vec{p}_2 ,

$$S_\phi(p_1) = \frac{1}{2(2\pi)^2 p_1} \int d\cos\theta \int_0^\Lambda dp_2 p_2 s \sigma(s), \quad (15)$$

with

$$\sigma(s) = \begin{cases} \frac{\Lambda^2}{8\pi M_s^4} \left(1 - 4\frac{m_{\nu_s}^2}{s}\right)^{3/2}, & \text{scalar} \\ \frac{s + 2m_{\nu_s}^2}{12\pi M_s^4} \sqrt{1 - 4\frac{m_{\nu_s}^2}{s}}, & \text{vector} \end{cases}. \quad (16)$$

⁶ The collision term for both species is positive since it describes the probability of collision. For massless ghosts, which carry negative energies, one has generally that $E_\phi = -p_\phi \leq 0$ with $p_\phi \geq 0$, and hence $f_\phi^0 \geq 0$, $n_\phi \geq 0$, $\rho_\phi \leq 0$, $P_\phi \leq 0$ and $w_\phi \geq 0$, from Eqs. (19) and (21). The negative pressure indicates that ghosts anti-gravitate.

⁵ See footnote 3.

The neutrino spectrum is slightly more complicated to calculate because the phase space of the ghosts is restricted by the momentum cutoff Λ ; hence one cannot write a completely analogous expression involving the cross section for $\nu_s \nu_s \rightarrow \phi \phi$. Instead,

$$S_{\nu_s}(p_3) = \frac{1}{16(2\pi)^4} \frac{1}{E_3} \int dc_{12} dc_{13} d\varphi \times \int_0^\Lambda dp_2 \frac{p_1^2 |\mathcal{M}|^2 \Theta(\Lambda - p_1)}{E_3 - p_3 c_{23}}, \quad (17)$$

where $c_{ij} = \hat{p}_i \cdot \hat{p}_j$, and $p_1 = p_2(E_3 - c_{23}p_3)/(p_2(1 - c_{12}) - (E_3 - c_{13}p_3))$. The integrals in Eqs. (15) and (17) can be evaluated numerically and they correspond to the instantaneous spectrum $d\Gamma_n/dp_i$ once multiplied by the factor $4\pi p_i^2/(2\pi)^3$.

We can use the computed collision terms to derive the phase-space distributions at the present time, which are given by Eq. (14) with $t = t_0$ or equivalently $a = a_0 = 1$ and where

$$H(a) = H_0 \sqrt{\frac{\Omega_m}{a^3} + \frac{\Omega_r}{a^4} + \Omega_\Lambda + \Omega_g(a)}. \quad (18)$$

Here, Ω_m , Ω_r and Ω_Λ are the relative abundances of total matter (baryonic plus cold dark matter), radiation (photons plus massless SM neutrinos) and dark energy described by a cosmological constant, respectively, and the contribution from the ghost plus ν_s densities is $\Omega_g(a) = (\rho_\phi(a) + \rho_{\nu_s}(a))/\rho_{\text{crit}}$ with the critical density defined as usual, $\rho_{\text{crit}} = 3H_0^2/(8\pi G)$. In practice, one can neglect Ω_r since the ghost fluid is produced mainly at late times. In the following, we will assume for simplicity a flat universe, which is also the expectation after a period of early-time acceleration dubbed as inflation [18]. In this way, we have $\Omega_\Lambda + \Omega_m + \Omega_g = 1$, where we have defined $\Omega_g \equiv \Omega_g(a_0)$ for simplicity.

The distribution functions in (14) are normalized such that the particle number densities are given by ⁷

$$n_i(t) = \int dp_i p_i^2 f_i^0(t, p_i) = \Lambda^3 \int dx x^2 f_i^0(t, x). \quad (19)$$

The shapes of the spectra at the present epoch for the vector and scalar mediator models are shown in Fig. 3. It is straightforward to show that the redshifted spectra $f_i^0(t_0, p_i)$ computed via Eq. (14) are identical to those derived through Eq. (2).

It can be convenient to have an explicit formula for $f_{\nu_s}^0$ in the case where $m_{\nu_s} = 0$ and vector mediator,

$$p^2 f_{\nu_s}^0(p) dp = A \Lambda^4 H_0^{-1} x^2 e^{-\pi x^2} dx, \quad (20)$$

where $x = p/\Lambda$ and $A = 7.7 \times 10^{-4}(\Lambda/M_i)^4$. Although this is a numerical fit, the coefficient π in the exponent turns out to be accurate to three digits. ⁸

III.4. Phantom fluid evolution

Treating the ghosts and sterile neutrinos as cosmological fluids, one can compute their energy density, pressure and equation of state (EOS) at the background level as

$$\begin{aligned} \rho_i(t) &= \int dp_i p_i^2 E_i f_i^0(t, p_i), \\ P_i(t) &= \int dp_i p_i^2 \frac{p_i^2}{3E_i} f_i^0(t, p_i), \\ w_i(t) &= \frac{P_i(t)}{\rho_i(t)}, \end{aligned} \quad (21)$$

where $f_i^0(t, p_i)$ is given by Eq. (14), and $E_\phi \leq 0$. Figure 4 shows the scale-factor evolution of the energy densities of ϕ and ν_s for different values of the sterile neutrino mass m_{ν_s} , in addition to their sum. As expected, in the case of massless ν_s there is no net contribution of the two new species to the total energy density of the Universe, while for $m_{\nu_s} > 0$, there is a clear difference between $|\rho_i(a)|$ for the two components.

The energy densities shown in Fig. 4 can be derived in a simpler way, directly from the Boltzmann equation (11), after weighing by the energy E_i and integrating over the particle three-momentum. This gives

$$\begin{aligned} \frac{d\rho_\phi}{dt} + 4H\rho_\phi &= -\Gamma_\rho, \\ \frac{d\rho_{\nu_s}}{dt} + 3H(1 + w_{\nu_s})\rho_{\nu_s} &= +\Gamma_\rho, \end{aligned} \quad (22)$$

where Γ_ρ is the rate of change in the particle energy density due to the vacuum decay, computed in appendix B (see Eq. (B12)) which gives approximately

$$\Gamma_\rho \cong \Gamma_n \Lambda \times \begin{cases} 0.76, & \text{scalar} \\ 0.82, & \text{vector} \end{cases} \equiv c_m \Gamma_n \Lambda, \quad (23)$$

in terms of Γ_n from Eq. (10).

In Eq. (22), the equation of state for sterile neutrinos w_{ν_s} depends upon m_{ν_s} , and it could *a priori* also be a function of time. w_{ν_s} ranges between zero for nonrelativistic particles when $m_{\nu_s} \sim \Lambda$ to 1/3 for relativistic ones, when $m_{\nu_s} \sim 0$. This is confirmed by Fig. 5 (left), which shows the present-day w_{ν_s} computed via Eq. (21) as a function of m_{ν_s} . We find that a good fitting formula is

$$w_{\nu_s}(\tilde{x}) \simeq \begin{cases} 1/3 - 1.33\tilde{x}^2 + 1.92\tilde{x}^3 - 1.07\tilde{x}^4 + 0.16\tilde{x}^6, \\ 1/3 - 1.05\tilde{x}^2 + 0.82\tilde{x}^3 + 0.01\tilde{x}^4 - 0.12\tilde{x}^6, \end{cases} \quad (24)$$

⁷ In Eq. (19) and from now on, we include the numerical factor $4\pi/(2\pi)^3$ in the definition of the phase-space distribution f_i^0 , given by Eq. (14).

⁸ For other choices of m_{ν_s} we find similar fits by replacing $x^2 e^{-\pi x^2} \rightarrow (2/3)x^{1.59} e^{-4x^{2.28}}$ for $m_{\nu_s}/\Lambda = 0.5$ and $\rightarrow 0.349 x^{1.57} e^{-8.255 x^{2.39}}$ for $m_{\nu_s}/\Lambda = 0.75$.

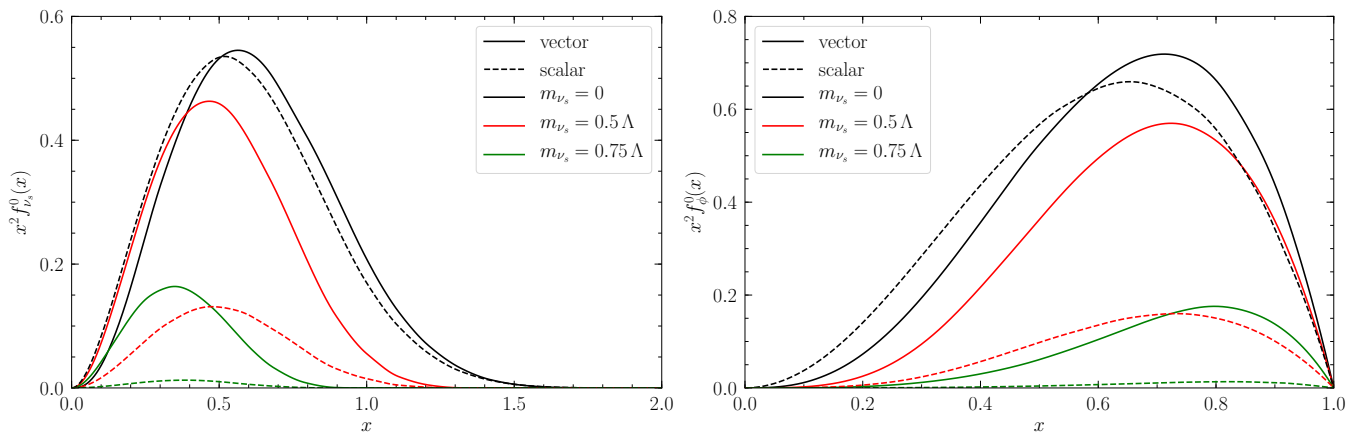


FIG. 3. *Left*: Present-day sterile neutrino momentum spectrum, divided by $\Lambda^5/(128\pi^6 M_i^4 H_0)$, with $M_i = M_s$ (scalar mediator) or M_v (vector mediator), for several choices of m_{ν_s}/Λ . Here $x = p/\Lambda$ and we used $\Omega_m = 0.32$. Solid (dashed) curves are for the vector (scalar) mediator model. *Right*: Momentum distribution for ghosts.

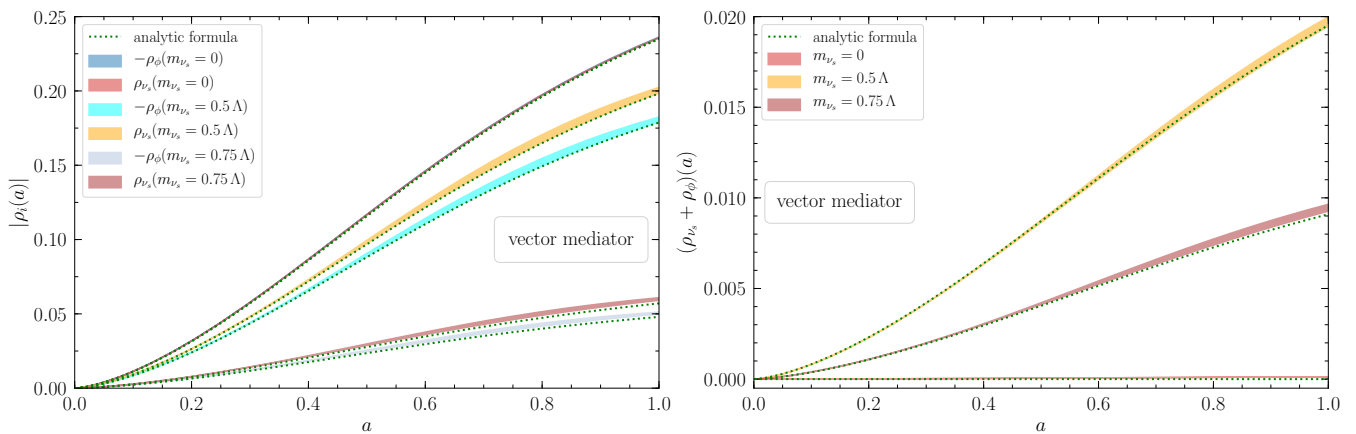


FIG. 4. Scale-factor evolution of the absolute value of the energy densities for ghosts ϕ (which have $\rho_\phi < 0$) and sterile neutrinos ν_s (*Left*), and of their sum (*Right*) for the vector mediator case. The units of $\rho_i(a)$ are $\Lambda^9/(128\pi^6 M_j^4 H_0)$ ($j = v, s$). Solid lines are the result of numerically solving Eq. (21). The color shaded band represents the uncertainty on the back-reaction from $\Omega_g(a)$ in the Friedmann equation (18) for the values of Γ_ρ allowed by Type Ia supernova (see Section III.5). The green dotted lines are given by the analytic formulas in Eq. (31), derived from the Boltzmann equations in (22) when back-reaction is neglected. For both plots, we used $\Omega_m = 0.32$ and Ω_Λ is determined by the flatness condition $\Omega_\Lambda = 1 - \Omega_m - \Omega_g$.

respectively for the vector and scalar mediator, where $\tilde{x} \equiv m_{\nu_s}/\Lambda \in [0, 1]$.

The ν_s equation of state turns out to be time independent, to a good approximation, as displayed in Fig. 5 (right). It can be shown that the time independence is exact whenever the scale factor has a simple power law behavior, $a(t) = t^p$, because in that case the integrals in Eq. (21) factorize to the form $\rho_i = F(t)\hat{\rho}_i(p)$ and $P_i = F(t)\hat{P}_i(p)$ such that the time dependence cancels in their ratio. Since most of the ghost fluid production takes place while the Universe is approximately matter dominated, this analytic behavior is realized by the full numerical solution.

It is convenient to recast the Boltzmann equations (22) in dimensionless form, with $y = a^3$ playing the role of time,

$$\begin{aligned} \frac{d\Omega_\phi}{dy} + \frac{4}{3y}\Omega_\phi &= -\frac{\epsilon_\rho}{y\hat{H}(y)}, \\ \frac{d\Omega_{\nu_s}}{dy} + \frac{1+w_{\nu_s}}{y}\Omega_{\nu_s} &= \frac{\epsilon_\rho}{y\hat{H}(y)}, \\ \hat{H}(y) &= \sqrt{\Omega_\Lambda + \Omega_m/y + \Omega_g(y)}, \end{aligned} \quad (25)$$

and $\epsilon_\rho \equiv \Gamma_\rho/(3H_0\rho_{\text{crit}})$. Evidently, in the limit of massless ν_s , $w_{\nu_s} = 1/3$ and the net contribution $\Omega_g(y) = \Omega_\phi(y) + \Omega_{\nu_s}(y)$ remains exactly zero, as expected.

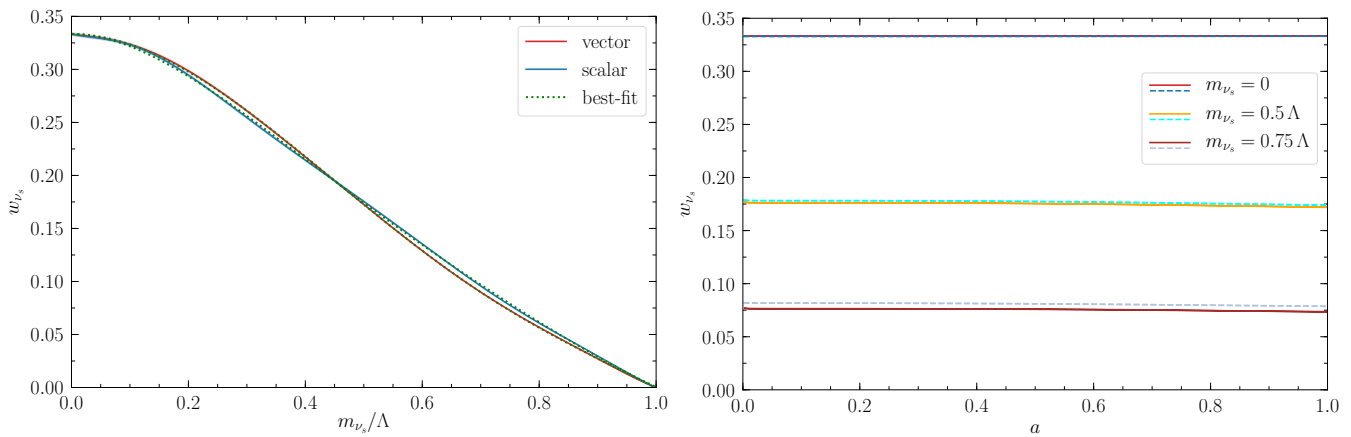


FIG. 5. *Left*: Present-day equation of state of sterile neutrinos w_{ν_s} as a function of the sterile-neutrino mass to cutoff ratio. The numerical results are shown with solid lines, while green dotted curves correspond to the numerical-fit functions (24). *Right*: Scale-factor evolution of w_{ν_s} for different choices of m_{ν_s} . The solid curves are for the vector mediator model, whereas the dashed curves are for the scalar model. The band thicknesses and Ω_m and Ω_Λ are as in Fig. 4.

Taking massless ghosts and massive neutrinos rather than vice versa is an arbitrary model-building choice. The system of equations for the alternative choice is trivially related, by exchanging the roles of Ω_ϕ and Ω_{ν_s} in Eq. (25), and relabeling $w_{\nu_s} \rightarrow w_\phi$. The first choice results in $\Omega_g > 0$ while the second gives $\Omega_g < 0$. We will consider the general case in the following, which results in a sign choice \pm for the solutions given below.

By solving the system (25) numerically, one finds that the net production $\Omega_g(y)$ is approximately linear in ϵ_ρ , for $\epsilon_\rho \lesssim \mathcal{O}(10)$. For larger ϵ_ρ , linearity breaks down because the back-reaction of the ghost plus ν_s fluid appears in \hat{H} and reduces the production; however such large values are ruled out by observations of late-time cosmology, namely supernovae, as we will show. Hence we focus on the linear regime. Useful approximate fits to the numerical solutions are given by

$$\begin{aligned} \Omega_{\nu_s/\phi}(y) &= \pm \epsilon_\rho A_0 y^{A_1 - A_2 y - A_3 y(1-y)}, \\ \Omega_g(y) &\cong \pm \epsilon_\rho f(w_{\nu_s}) (1 + 0.109 \ln y)^{3.09}, \\ f(w_{\nu_s}) &\cong 0.163 - 0.594 w_{\nu_s} + 0.321 w_{\nu_s}^2 \end{aligned} \quad (26)$$

where the coefficients A_i are linear functions of the equation-of-state parameter w , shown in Table I, and the factor $(1 + 0.109 \ln y)^{3.09}$ should be interpreted as zero at small y where it would become negative. The choice of sign corresponds to taking massless ghosts and massive ν_s (+) or vice versa (-). For small m_{ν_s} , one can read from Eq. (24) that $(1/3 - w_{\nu_s}) \cong C_m (m_{\nu_s}/\Lambda)^2$ with $C_m \cong 4/3$ for the scalar mediator and $C_m \cong 1$ for the vector mediator.

$\begin{aligned} A_0 &\approx 0.7969 - 0.486 w \\ A_1 &\approx 0.4128 - 0.017 w \\ A_2 &\approx 0.0587 - 0.003 w \\ A_3 &\approx 0.4296 + 0.076 w \end{aligned}$
--

TABLE I. Dependence of the coefficients A_i in Eq. (26) on the equation-of-state parameter w . For massive neutrinos, $w = w_{\nu_s} < 1/3$, for massless ghosts $w = 1/3$, and vice versa for massless neutrinos and massive ghosts.

III.5. Constraints from type Ia Supernovae

Because the net fluid of ghosts plus sterile neutrinos is produced at late times, a sensitive probe of its effect on cosmology is the use of supernovae as standard candles [19, 20]. Below, in Section IV.2, we will do a full analysis including other cosmological data sets. This preliminary study serves to define the parametric region of interest for the later Monte Carlo exploration.

The luminosity distance $d_L(z)$ of type Ia supernovae can probe deviations from the standard expansion history of the Universe. It is given by

$$d_L(z) = (1+z) c \int_0^z \frac{dz'}{H(z')} \quad (27)$$

where $H(z)$ is given by Eq. (18) with $a = (1+z)^{-1}$. It is related to the distance modulus $\mu(z) = 5 \log_{10}(d_L(z)/10 \text{ pc})$, which is experimentally determined from the observed and modeled absolute luminosities of the supernovae. Given a covariance matrix C_{ij} , the log-likelihood can be computed in the standard way,

$$-2 \ln \mathcal{L} = \chi^2 = \delta \vec{\mu}^T C^{-1} \delta \vec{\mu}, \quad (28)$$

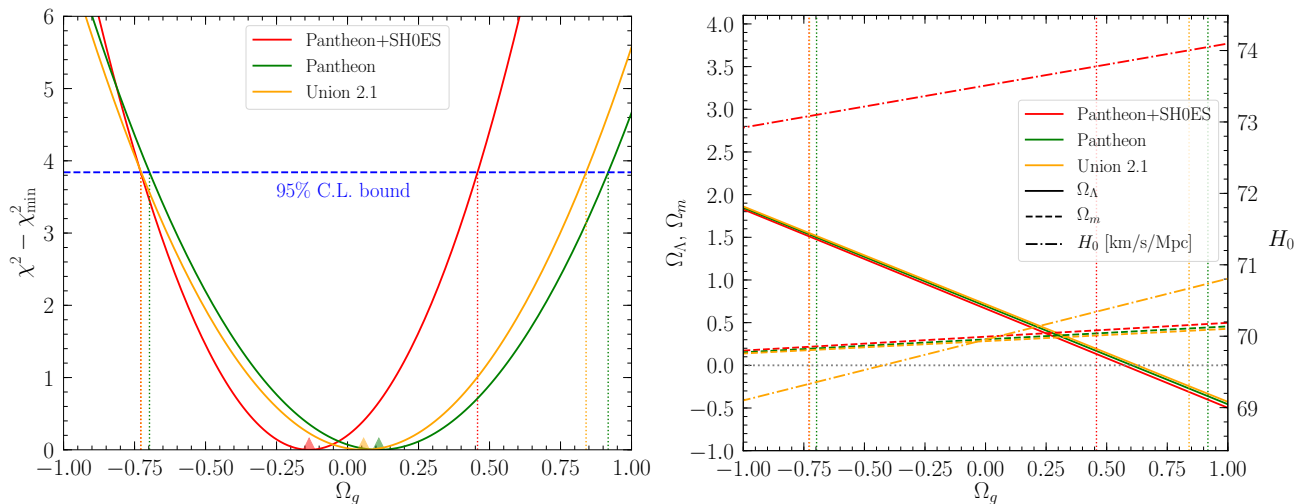


FIG. 6. *Left*: 95% C.L. allowed regions for the ghost plus sterile neutrino contribution to the present composition of the Universe, for the three supernovae data sets considered. The triangles indicate the best-fit values for Ω_g . *Right*: Most likely values of Ω_Λ (solid), Ω_m (dashed) and H_0 (dot-dashed) as a function of Ω_g . The 95% C.L. regions of the latter are indicated as dotted vertical lines.

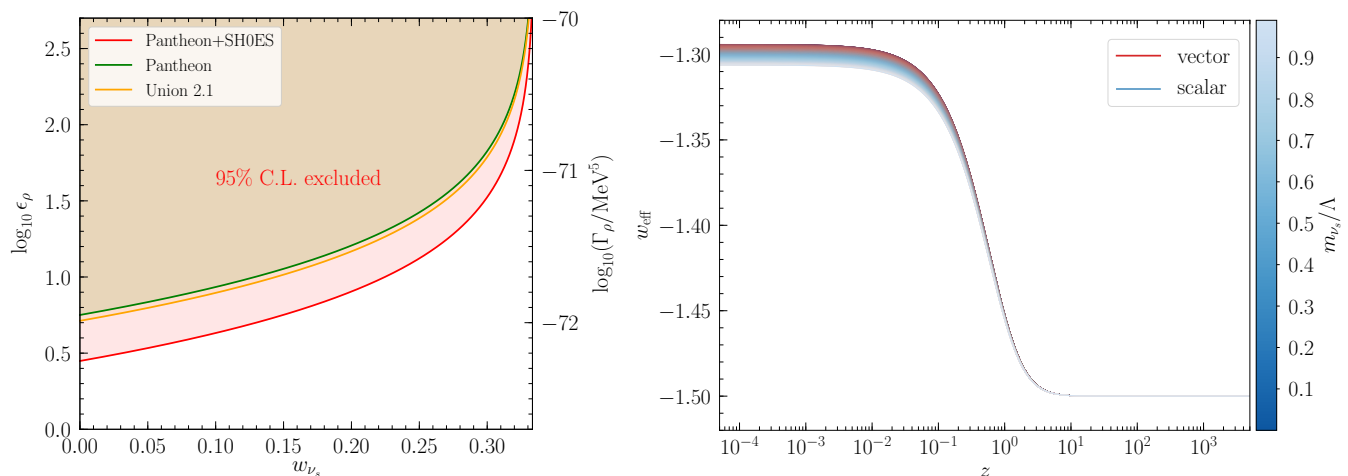


FIG. 7. *Left*: Mapping of Fig. 6 to the parameters $\epsilon_\rho = \Gamma_\rho/(3H_0\rho_{\text{crit}})$ or Γ_ρ as a function of the equation-of-state w_{ν_s} for sterile neutrinos. *Right*: Redshift evolution of the effective equation-of-state parameter w_{eff} for the $\phi + \nu_s$ fluid. The band colors distinguish the vector and scalar mediator models respectively. Ω_m and Ω_Λ are fixed as in previous figures (w_{eff} depends only weakly on these assumptions).

where $\delta\vec{\mu}$ is the vector of residuals between theory and observation. One minimizes the χ^2 with respect to the cosmological parameters to find the best-fit values and confidence intervals. This is known in the literature as frequentist profile likelihood, which is complementary to the Bayesian Markov Chain Monte Carlo (MCMC) since the latter identifies large regions in the parameter space that exhibit a good fit to the data. In the present case, the parameters over which to minimize the χ^2 are the Hubble rate H_0 , the present contribution to the energy density from the ghosts and sterile neutrinos Ω_g , and that from the total matter contribution, Ω_m . There may

also be a nuisance parameter, the correction factor of the absolute magnitude of the supernovae M , which is degenerate with H_0 for uncalibrated supernovae. We assume flatness, so that the dark energy contribution is determined as $\Omega_\Lambda = 1 - \Omega_m - \Omega_g$.

This procedure was followed for three different (but not all mutually exclusive) data sets: Union 2.1 [21], Pantheon [22], and Pantheon+SH0ES [23], comprising 580, 1048 and 1657 supernovae, respectively.⁹ In an alterna-

⁹ The Pantheon+ sample contains 1701 spectroscopically con-

tive analysis of Pantheon+, the smaller sample of 1590 SNe is used, omitting the nearby SNe whose absolute distances are calibrated using Cepheid variables; this leaves H_0 and M undetermined. The determination of the other parameters gives the same result in both cases.

The results of minimizing the χ^2 for the different data sets are shown in Fig. 6 (left). There is no preference for $\Omega_g \neq 0$, but large magnitudes are allowed at 95% C.L., down to -0.75 for the case of massive ghosts and up to 0.45 - 0.9 for massless ghosts, depending upon the data set. Fig. 6 (right) displays the preferred values of Ω_Λ and Ω_m as a function of Ω_g , along with the dependence of the Hubble parameter H_0 on Ω_g . Two values are shown, corresponding to the Union 2.1 and Pantheon+ samples (since Pantheon does not determine H_0). Both are linearly increasing functions of Ω_g , but are offset from each other by about 4 km/s/Mpc. The Union 2.1 fit gives a minimum value of $H_0 \cong 69.3$ km/s/Mpc at $\Omega_g \cong -0.75$, which is still in tension with the Planck determination 67.4 ± 0.5 [24] at nearly 4σ . In Section IV.2 we will show that this preliminary result agrees with a more careful analysis where all of the standard Λ CDM parameters are allowed to vary.

The 95% C.L. bounds on Ω_g in Fig. 6 restrict the allowed values of the dimensionless parameter ϵ_ρ (defined below Eq. (25)) or its dimensionful counterpart Γ_ρ . Fig. 7 (left) shows these limits for massless ghosts and massive sterile neutrinos as a function of the ν_s equation-of-state parameter w_{ν_s} . As already anticipated, values of ϵ_ρ larger than $\mathcal{O}(10)$ are excluded by supernova data, except when $w_{\nu_s} \sim 1/3$. However, for such values of w_{ν_s} the magnitude and shape of the energy densities of the new species become irrelevant since their contributions cancel, giving a negligible effect in the Friedmann equation (18). Therefore, the use of the approximate fits in Eq. (26), which assume linearity in ϵ_ρ , is justified even for these larger values of ϵ_ρ .

The minimum value of χ^2 for each data set, compared to the χ^2 value for the standard Λ CDM parameter values, can be characterized by $\Delta\chi^2 = \chi_{\min}^2 - \chi_{\Lambda\text{CDM}}^2$. It is given by -2810.4 (Pantheon+), -1.1 (Pantheon), and -94.5 (Union 2.1). The discrepancy for Union and Pantheon+ arises from the dependence on H_0 in the χ_{\min}^2 , which is calibrated using Cepheids. The superficial appearance that the ghost model gives a better fit than Λ CDM is a reflection of the Hubble tension between the supernovae and the larger cosmological data sets. This tension is hidden for the Pantheon analysis since H_0 is marginalized out. We will confirm a mild preference for the ghost model over Λ CDM in Section IV.2.

An interesting question is whether Ω_g can explain all of the dark energy, replacing the cosmological constant.

Figure 6 suggests that this is indeed possible, using the Union and Pantheon data sets, by taking $\Omega_g \sim 0.6$. However it is in tension with the Pantheon+ upper bound $\Omega_g < 0.45$, which requires $\Omega_\Lambda \gtrsim 0.2$. In general, the capability of Ω_g to function as dark energy can be understood through the effective EOS of the ghost fluid

$$w_{\text{eff}} = \frac{P_\phi + P_{\nu_s}}{\rho_\phi + \rho_{\nu_s}}, \quad (29)$$

whose redshift dependence is plotted in Fig. 7 (right). Notably, it violates the weak energy condition since $w_{\text{eff}} < -1.3$ both at early and late times. The early-time limit $w_{\text{eff}} \rightarrow -1.5$ can be derived analytically from the exact solution (31) that will be introduced below, in the regime where back-reaction of the ghost fluid is negligible. The late-time limit $w_{\text{eff}} \cong -1.3$ depends weakly on the value of m_{ν_s}/Λ . Coincidentally, such a value of w_{eff} was shown to solve the Hubble tension by shifting the central value of H_0 without broadening its uncertainty, although the associated model would be strongly disfavored with respect to the Λ CDM baseline model [25]. It is striking that the ghost fluid (in conjunction with the produced positive-energy particles) can function as dark energy even in the absence of a classical condensate, or indeed a potential $V(\phi)$, which was the original motivation for phantom fields in cosmology. The latter conclusion was originally drawn by Ref. [7], which obtained similar redshift evolution of w_{eff} as we derived in Fig. 7 (right), directly from the conservation of the energy-momentum tensor.

IV. CMB AND LARGE SCALE STRUCTURE

Even if their combined contributions to the energy density of the Universe are negligible, the creation of massless ghosts and positive-energy particles can leave an imprint on the CMB and matter power spectra. In particular, if both species are massless, their energy densities cancel exactly, but they can nevertheless alter the cosmological evolution and the formation of structure through their perturbations, depending on the production rate.

As noted above, the expansion history of the Universe is modified if the ghosts and ν_s are not degenerate in mass. We estimate that the results for $m_{\nu_s} > 0$ will revert to those of the massless case when $m_{\nu_s} \lesssim 2 \times 10^{-5} \Lambda$. This was found by comparing the effects on the CMB and matter power spectra, including the linear order perturbations, and either including or neglecting the zeroth-order contributions of the new species. In the following sections we will study the two qualitatively distinct regimes, depending on the scale of m_{ν_s} .

IV.1. Massless ν_s case

If ν_s is sufficiently light, its contribution to the total energy density of the Universe cancels that of the pre-

firmed type Ia supernovae up to redshift $z \simeq 2.3$, but only 1657 of them have $z > 0.01$. We followed Ref. [23] in omitting supernovae with $z < 0.01$ from the analysis because of their large peculiar velocities, which preclude an accurate determination of the cosmological parameters.

sumed massless ghosts and there is no appreciable effect at the background level. The first nontrivial contribution arises at linear order in the cosmological perturbations. We derive the relevant equations in Appendix B and find that the perturbations for ϕ and ν_s do not cancel each other, mainly because of the different phase-space distribution between the two species, shown in Fig. 3; see also Eqs. (B29) and (B30).

The perturbations were implemented in a modified version of the Boltzmann code **CAMB** [26]. To the six parameters comprising the Λ CDM model,¹⁰

$$\Omega_b h^2, \Omega_c h^2, 100 \theta_{\text{MC}}, \tau, \ln(10^{10} A_s), n_s, \quad (30)$$

we add two new ones: Γ_ρ , which controls the amplitude of the background energy densities of the dark species, and Γ_ρ/Λ^4 , which determines the strength of the first-order perturbed collision term. We assume vanishing initial conditions for the ϕ and ν_s perturbations in the early radiation era ($a \ll 10^{-5}$).

For the background energy densities, the Boltzmann equations (22) can be rewritten in terms of the scale factor a and solved analytically, since the net density of the new species vanishes in the Friedmann equation (18). The solutions are

$$\begin{aligned} \rho_\phi(\bar{x}) &= -\frac{2\Gamma_\rho}{11 H_0 \sqrt{\Omega_\Lambda}} \sqrt{\bar{x}} \\ &\times {}_2F_1\left(\frac{1}{2}, \frac{11}{6}, \frac{17}{6}, -\bar{x}\right), \\ \rho_{\nu_s}(\bar{x}) &= \frac{\Gamma_\rho}{3(3/2 + w_{\nu_s}) H_0 \sqrt{\Omega_\Lambda}} \sqrt{\bar{x}} \\ &\times {}_2F_1\left(\frac{1}{2}, \frac{3}{2} + w_{\nu_s}, \frac{5}{2} + w_{\nu_s}, -\bar{x}\right), \end{aligned} \quad (31)$$

defining $\bar{x} \equiv a^3 \Omega_\Lambda / \Omega_m$, where ${}_2F_1(a, b, c, z)$ is the hypergeometric function.¹¹

The effects of the two new species on the CMB temperature and linear matter power spectra are shown in Fig. 8. The main modification on the former is an overall decrease of the late Integrated Sachs-Wolfe (ISW) effect, visible at large angular scales (small ℓ), which is due to the increase of the gravitational potential along the path of photons between the time of last scattering and today. This makes the photons lose energy as they travel

through gravitational potential wells that are growing in time.

More precisely, the late ISW contribution to the CMB anisotropy in Fourier space is given by [32]

$$\mathcal{C}_\ell^{\text{ISW}} \propto \int dk k^2 \left[\int_{\tau_*}^{\tau_0} d\tau (\Psi' - \Phi') j_\ell(k(\tau_0 - \tau)) \right]^2, \quad (32)$$

where τ_* and τ_0 are the conformal times at last scattering and today, respectively, Ψ and Φ are the potential and curvature in conformal Newtonian gauge [33], the prime indicates the conformal time derivative, and j_ℓ are the spherical Bessel functions. The Newtonian curvature Φ and potential Ψ for the mode k are set by the total density contrast δ_{tot} , velocity θ_{tot} and shear σ_{tot} perturbations [34],

$$\begin{aligned} \Phi &= \frac{4\pi G a^2}{k^2} \left[\rho \delta + \frac{3\mathcal{H}}{k^2} (\rho + P) \theta \right]_{\text{tot}}, \\ \Psi &= -\Phi - \frac{12\pi G a^2}{k^2} [(\rho + P) \sigma]_{\text{tot}}, \end{aligned} \quad (33)$$

where $\mathcal{H} = aH(a)$ is the conformal Hubble parameter. The terms in the square brackets in Eq. (33) are gauge invariant and hence they can be evaluated in the frame comoving with the cold DM (CDM), corresponding to synchronous gauge. In a flat Λ CDM universe, the late ISW contribution is zero during matter domination because both Ψ and Φ remain constant, but as dark energy begins to dominate, the curvature Φ decays, reducing the magnitude of the potential Ψ . This effect is enhanced if (i) there is extra radiation pressure, (ii) the Universe expands faster than in Λ CDM, or (iii) a nonzero spatial curvature is present [35–37].

In the present case, one can understand the decrease of the late ISW effect directly from Eq. (33). Figure 9 (left) shows the large-scale evolution of the synchronous-gauge physical perturbations for sterile neutrinos ν_s and ghosts ϕ , which can be treated as a single effective fluid since both species are relativistic. The ghost nature as a negative-energy particle manifests itself through the opposite sign in the physical perturbations ($\rho_\phi F_{\phi,\ell}$) with respect to those for ν_s , having negative density contrast and velocity, but positive shear stress perturbations, which is due to $\rho_\phi \lesssim 0$. Positive physical shear stress is a generic feature of phantom cosmological species and the main effect is to drive clustering [38]. This is exactly the opposite of what happens for normal species like SM neutrinos, where the presence of the shear stress leads to erasure of fluctuations that might initially be present in the fluid, suppressing further growth.

Due to the larger phase space available for ν_s ,¹² which increases its first-order perturbed collision term, the relative perturbations for ν_s are expected to dominate over

¹⁰ $\Omega_b h^2$ and $\Omega_c h^2$ are the present-day abundances of baryons and cold DM, respectively, multiplied by the square of the reduced Hubble constant h . $100 \theta_{\text{MC}}$ is a **CosmoMC** parameter describing approximately the position of the first acoustic peak, and is used instead of H_0 because it is less correlated with other parameters. τ is the reionization optical depth, while A_s and n_s are the primordial scalar amplitude and spectral index respectively.

¹¹ Eq. (31) are valid whenever back-reaction of the new species on the Hubble-parameter evolution can be neglected, and they apply for any value of m_{ν_s} . One should keep in mind that Γ_ρ is generally a function of m_{ν_s} (see Eqs. (23) and (10)), which in turn affects the value of w_{ν_s} as described by Eq. (24).

¹² The momentum of ν_s can reach 2Λ for extreme kinematic configurations, while that of the ghost is limited to Λ .

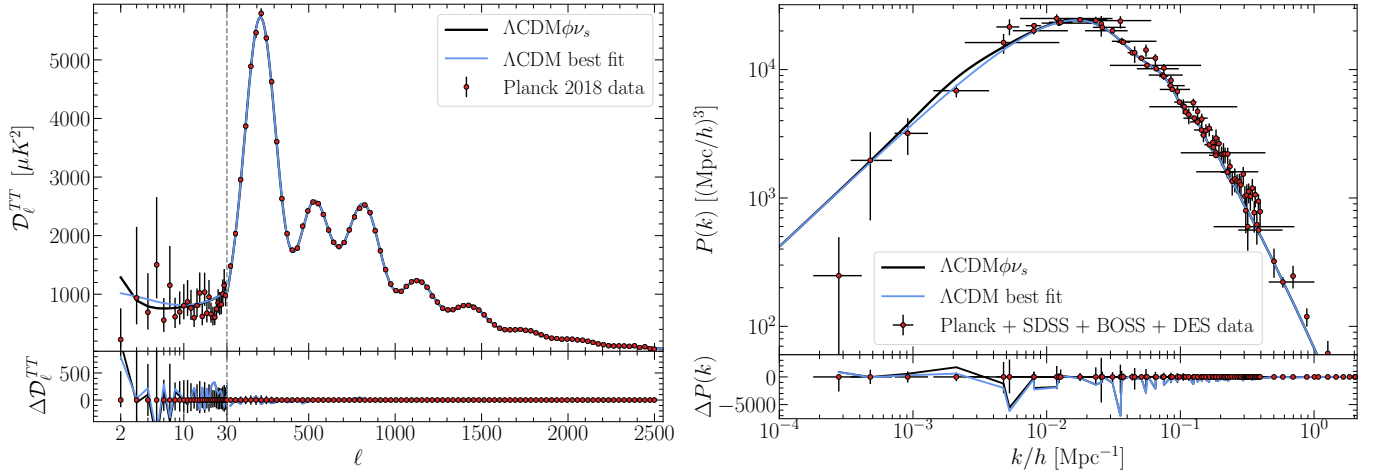


FIG. 8. For the special case of $m_{\nu_s} = 0$. *Left*: Prediction of the Λ CDM $\phi\nu_s$ model (black curve) for the CMB temperature autocorrelation spectrum, compared to the Λ CDM best-fit model (blue curve). The Planck 2018 data points are taken from Ref. [24]. *Right*: Predictions for the linear matter power spectrum. The data points, used only for display purposes, are given by Ref. [27], which contains data from Planck 2018 [28], eBOSS DR14 [29], SDSS DR7 [30] and DES YR1 [31]. For both plots, the vector mediator is assumed, we used $\Gamma_\rho \simeq 10^{-69}$ MeV⁵, $\Gamma_\rho/\Lambda^4 \simeq 10^{-41}$ MeV and fixed the six Λ CDM parameters and H_0 to their Planck 2018 best-fit values. Residuals between the model predictions and the data points are shown at the bottom.

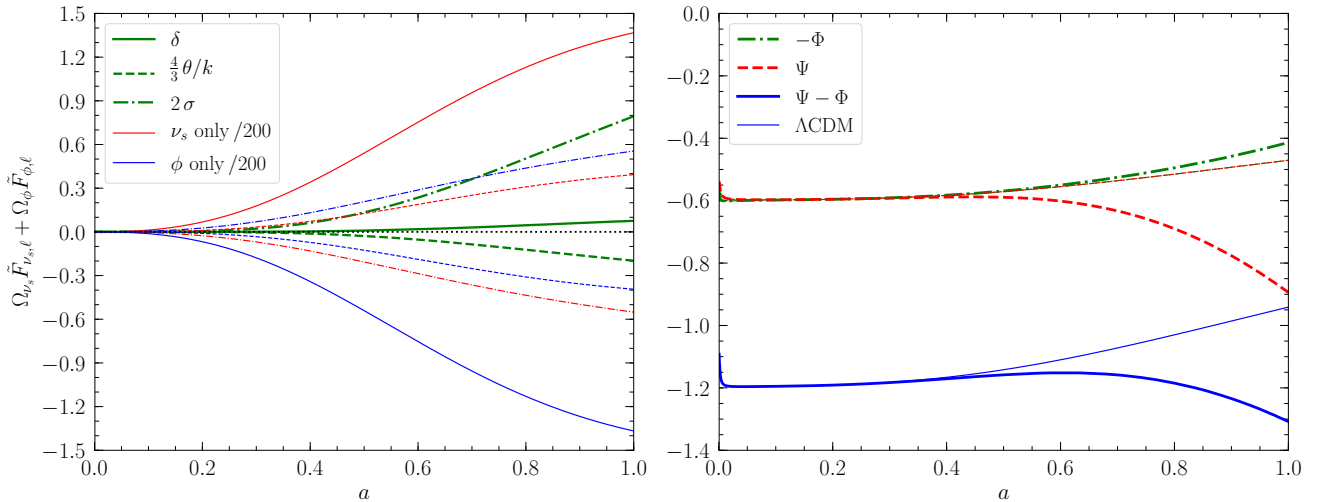


FIG. 9. *Left*: Scale-factor evolution of the cosmological perturbations at large scales ($k/h = 5 \times 10^{-4}$ Mpc⁻¹) for sterile neutrinos ν_s (red) and ghosts ϕ (blue), rescaled by 1/200. The physical perturbations are given by $\Omega_i F_{i,\ell}$, where $i = \phi, \nu_s$, $\Omega_i(a)$ is the fractional energy density and $F_{i,\ell}$ is the relative perturbation, Eq. (B13): $F_{i,0} = \delta_i$ (solid line), $F_{i,1} = (1 + w_i)\theta_i/k$ (dashed line) and $F_{i,2} = \frac{3}{2}(1 + w_i)\sigma_i$ (dot-dashed line); δ_i , θ_i and σ_i are the perturbations for the density contrast, velocity and shear, respectively. For massless ϕ and ν_s , $w_i = 1/3$. The sum $\sum_i \Omega_i F_{i,\ell}$ for δ , θ and σ , is shown in green (not rescaled). *Right*: Scale-factor evolution of the Newtonian curvature Φ and potential Ψ at the same scale. Thick lines include the contribution from the new species, while thin lines correspond to Λ CDM. Γ_ρ , Λ , H_0 and mediator are as in Fig. 8.

those for ϕ at high hierarchy multipoles (see discussion in section (1.a) of Appendix B). Since the relative shear σ and higher hierarchy multipoles for a single relativistic species are generally negative at large scales, as occurs for SM massless neutrinos and photons, we expect σ_ϕ to be more negative than σ_{ν_s} . As a consequence, the physical shear for the effective $\nu_s + \phi$ fluid, defined by

$\rho_{\nu_s}\sigma_{\nu_s} + \rho_\phi\sigma_\phi$, becomes positive, as borne out in Fig. 9 (left) with the dot-dashed green curve. The effect of the new species is therefore to decrease the value of the potential Ψ in Eq. (33), favoring matter clustering. This is shown with the red dashed curve in Fig. 9 (right).

On the other hand, the density contrast δ and the velocity perturbation θ for the effective single fluid turn out

to be positive and negative, respectively, which makes it harder to predict *a priori* the net contribution of the new species to Φ . The evolution of the latter is shown with the green dot-dashed curve in Fig. 9 (right). The net effect of the $\nu_s + \phi$ fluid is to reduce $\Psi - \Phi$, which generally leads to smaller C_ℓ^{ISW} in Eq. (32) than in Λ CDM. A similar trend occurs in phantom dark energy models with non-negligible anisotropic stress [39].

For larger values of Γ_ρ and Γ_ρ/Λ^4 , at the largest angular scales, the shear perturbation σ increases faster than the lower multipole perturbations δ and θ , driving $(\Psi - \Phi)$ to smaller values on shorter time scales. This results in a larger contribution to the late ISW effect in the CMB temperature power spectrum because of the square in Eq. (32), which is visible in Fig. 8 (left) around $\ell \sim 2 - 3$. The divergent nature of the perturbations for large values of Γ_ρ/Λ^4 or Γ_ρ is not surprising, since theories with ghosts are generically subject to instabilities. The growth of the instability is controlled by the ghost momentum cutoff Λ and the mediator mass M_i , and the analysis carried out below will exclude parameter values leading to excessive growth.¹³ We note that the effect of weak gravitational lensing on the CMB power spectra (*e.g.*, Ref. [40]), in the presence of ghosts and sterile neutrinos, does not deviate appreciably from the Λ CDM scenario because the Weyl potential $(\Psi - \Phi)/2$ in the two cases is essentially identical at small angular scales (large ℓ).

The modifications to the matter power spectrum in our scenario are also negligible for allowed values of Γ_ρ and Γ_ρ/Λ^4 , and the main effect is a small rise of the spectrum at large scales, as shown in Fig. 8 (right). The small positive contribution to $P(k)$ is due to its dependence on the ratio between the matter density perturbation $\delta\rho_m$ and the background matter density ρ_m . In fact, neither ν_s or ϕ contribute directly to $\delta\rho_m$ nor ρ_m , except through the metric perturbations appearing in the equation governing the evolution of $\delta\rho_m$. The increase in the matter power spectrum signals that the ghost and sterile neutrino effective fluid favors a mildly more efficient matter clustering than Λ CDM at large angular scales, which was already noticed from the CMB power spectrum.

IV.1.1. Method and Results

To constrain the new parameters Γ_ρ and Γ_ρ/Λ^4 , in conjunction with the Λ CDM ones, we ran the publicly available MCMC code `CosmoMC` [41]. Convergence of the MCMC chains was monitored through the Gelman-Rubin parameter $R - 1$ [42], by requiring $R - 1 \lesssim 0.01$. The cosmological data sets we considered are:

¹³ Conceivably, higher order perturbations could cut off the instabilities. In this work we constrain the effect of the first order perturbations, such that the higher-order contributions, proportional to higher powers of $\Gamma_\rho/\Lambda^4 \ll 1$, are negligible.

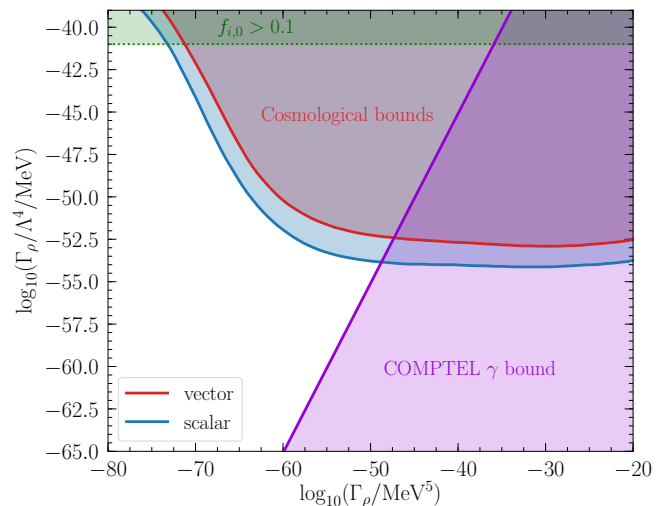


FIG. 10. Constraints on Γ_ρ/Λ^4 versus Γ_ρ , assuming $m_{\nu_s} = 0$. Red and blue regions correspond to the 95% C.L. cosmological bounds for the vector and scalar mediator models, respectively. Violet indicates the gamma-ray excluded region, Eq. (3). The green region is inconsistent with the technical assumption $f_i^0 \lesssim 0.1$ in Eq. (13).

- **Planck:** the full range of the CMB measurements from Planck 2018, which include the temperature and polarization anisotropies, as well as their cross-correlations [24];
- **Lensing:** the 2018 Planck measurements of the CMB lensing potential power spectrum, reconstructed from the CMB temperature four-point function [43];
- **BAO:** the distance measurements of the baryon acoustic oscillations given by the 6dFGS [44], SDSS-MGS [45], and BOSS DR12 [46] surveys;
- **DES:** the first year of the Dark Energy Survey galaxy clustering and cosmic shear measurements [31, 47, 48];
- **Pantheon:** distance measurements of (uncalibrated) type Ia supernovae from the Pantheon sample, comprising 1048 data points in the redshift range $z \in [0.01, 2.3]$ [22].

We did not include the `Halofit` modeling of the nonlinear part of the matter power spectrum because additional modifications of the standard nonlinear clustering model might be needed. Since this is beyond the scope of the present work, we consider only linear observables in our analysis.

Figure 10 shows the constraints on Γ_ρ and Γ_ρ/Λ^4 , for the vector and scalar mediator models, as derived from the `CosmoMC` analysis, in addition to the COMPTTEL bound of Eq. (3). Regarding the cosmological limits, one observes two features: the models in agreement with the

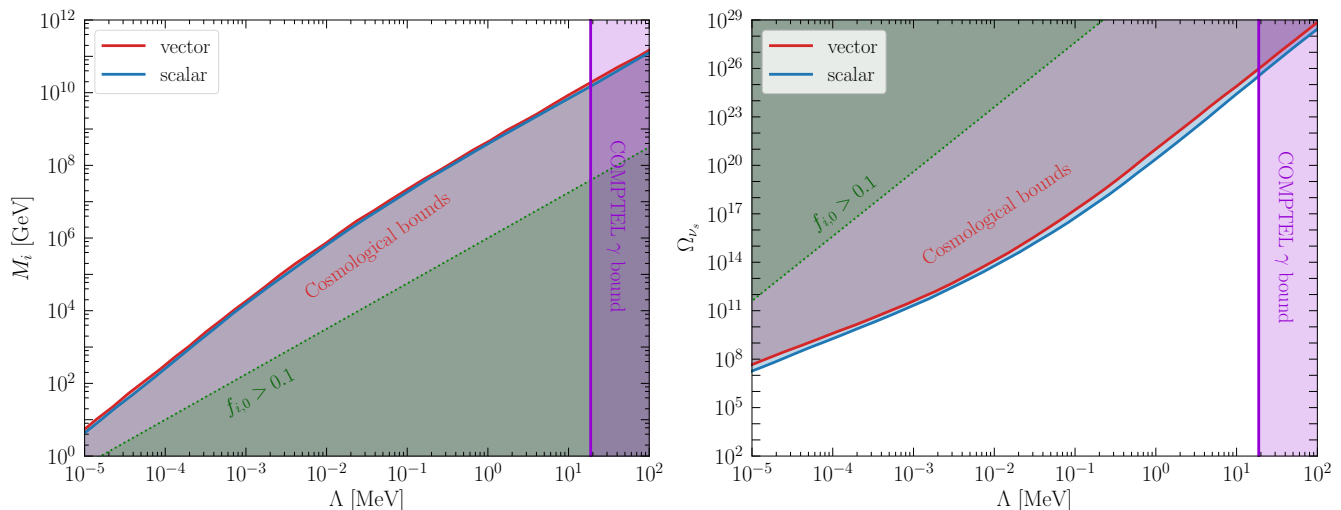


FIG. 11. For the special case of $m_{\nu_s} = 0$. *Left*: Mapping of excluded regions in Fig. 10 to the microphysics parameters, the mediator mass M_i ($i = v, s$) versus the ghost momentum cutoff Λ . *Right*: Conversion of the same constraints to the present-day sterile neutrino abundance Ω_{ν_s} as a function of the ghost momentum cutoff Λ . The color coding is the same as in Fig. 10

data lie in the region of $\Gamma_\rho/\Lambda^4 \lesssim 10^{-38}$ MeV, and for sufficiently small Γ_ρ/Λ^4 , the dependence on Γ_ρ disappears. We qualitatively explain such features in Appendix B, since they are closely related to the form of the perturbation equations. The constraints on the scalar mediator model are slightly stronger than those of the vector model, due to differences in the perturbation equations for the two interactions, which arise from their energy dependence; see, *e.g.*, Eq. (9).

The constraints on Γ_ρ/Λ^4 versus Γ_ρ can be mapped onto the plane of the ghost momentum cutoff Λ versus the mediator mass scale M_i , using Eq. (23). The resulting limits are shown in Fig. 11 (left) and they are essentially independent of the mediator type. Also shown is the consistency condition for neglecting the Pauli-blocking and Bose-Einstein stimulated-emission factors in the collision term of Eq. (12). This is inferred by demanding that $f_i^0 \sim 2\pi^2 \Gamma_\rho/(\Lambda^4 H_0) \lesssim 0.1$, which translates into the bound $\Gamma_\rho/\Lambda^4 \lesssim 10^{-41}$ MeV. For massless ν_s , this is equivalent to $M_i \gtrsim 1.0 \times 10^6 (\Lambda/\text{MeV})^{1.25}$ GeV for both the vector ($i = v$) and scalar ($i = s$) mediator cases. The 95% C.L. bounds on M_i versus Λ can be approximately expressed by

$$\frac{M_i}{\text{GeV}} \gtrsim 4.6 \times 10^8 \hat{\Lambda}^{1.3-0.05 \log_{10} \hat{\Lambda}}, \quad (34)$$

where $\hat{\Lambda} \equiv \Lambda/\text{MeV} \in (10^{-7}, 10^2)$.

We found that the two new parameters in the massless ν_s case leave the standard six Λ CDM parameters almost unchanged compared to their Planck 2018 best-fit values, without ameliorating any current cosmological tensions, such as the H_0 and S_8 tensions [49, 50]. This will be considered in more detail in Section IV.3 below. The correlations between these parameters are shown in Appendix C. Based on the foregoing discus-

sion, the constraints on Γ_ρ and Γ_ρ/Λ^4 are expected to be dominated by the CMB power spectra rather than large-scale-structure observables. We verified this by excluding BAO, DES, and Pantheon data sets in a separate CosmoMC run, finding that the results in Fig. 11 (left) were only slightly modified.

From the bounds in Fig. 10, one can estimate how large the abundance of massless sterile neutrinos can be today, while remaining consistent with cosmological data. This is shown in Fig. 11 (right), displaying Ω_{ν_s} versus the ghost momentum cutoff Λ for both mediator models. The surprisingly large values of $\Omega_{\nu_s} \gg 1$ are viable because of their exact cancellation by Ω_ϕ , so that the constraints arise only at the level of the perturbations. The maximum values of Ω_{ν_s} are reached by saturating the gamma-ray constraint, Eq. (3), leading to

$$\Omega_{\nu_s}^{95\% \text{ C.L.}} \lesssim \begin{cases} 9.6 \times 10^{25}, & \text{scalar mediator} \\ 3.4 \times 10^{25}, & \text{vector mediator} \end{cases}, \quad (35)$$

for $\Lambda \sim 19$ MeV. Despite the large numbers, these ν_s gases are still dilute, by many orders of magnitude, relative to a degenerate Fermi gas with Fermi energy Λ . Thus the occupation number $f_{\nu_s}(p) \ll 1$, even for this extreme case.

IV.2. Massive ν_s case

In section III.5, we made a preliminary study of the effects of producing massive neutrinos plus massless ghosts, comparing to supernova data but not to the other cosmological data sets. Here we undertake the more complete analysis, implementing the energy-density evolution of ϕ and ν_s at the background level, given by Eq. (26), in a

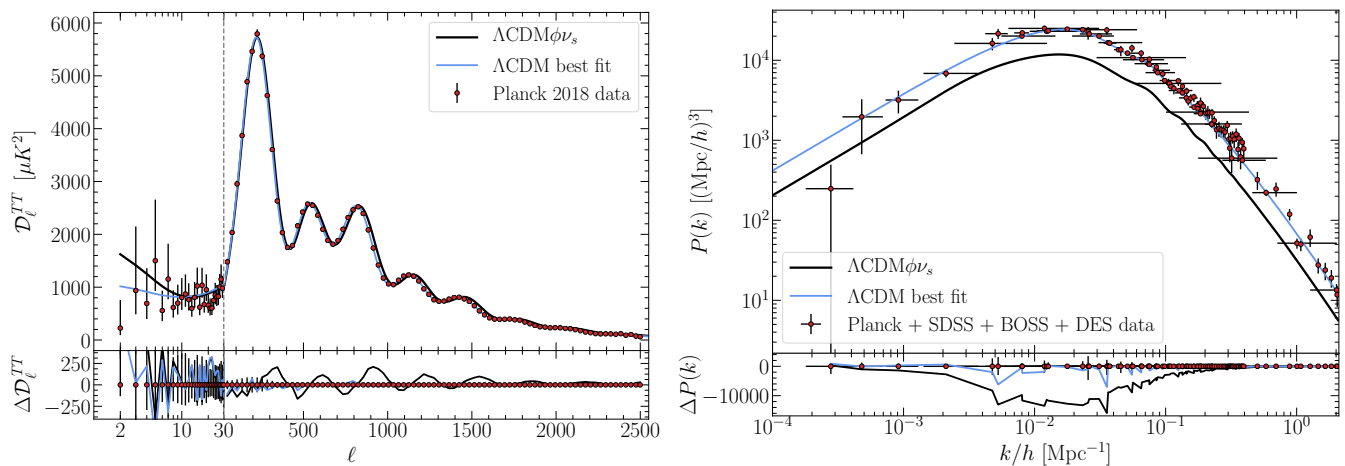


FIG. 12. Like Fig. 8, but for $m_{\nu_s} > 0$. We assumed $\Omega_g \simeq 0.6$, $w_{\nu_s} \simeq 0.02$, $\Omega_\Lambda \simeq 0.1$, and spatial flatness.

modified version of the CAMB code. It is embedded in CosmoMC to scan the full parameter space.

In addition to the six parameters of Λ CDM, we considered $\Omega_g \equiv \Omega_{\nu_s}(a_0) + \Omega_\phi(a_0)$, the net contribution of the ghost plus ν_s densities today, and the equation of state for sterile neutrinos w_{ν_s} as the independent new-physics parameters, even though they are related to each other via Eqs. (10, 23-24). This allows for simultaneous study of the scalar and vector mediator models, which differ only by how Ω_g and w_{ν_s} are related to the microphysical parameters m_{ν_s} , Λ , M_i .

The linear perturbations for the two new dark species were included in an approximate form, given by Eq. (B38) in Appendix B. A more exact form for the perturbations for massive sterile neutrinos is technically challenging to derive, and is left for a future study. We expect that the bounds on Ω_g and w_{ν_s} derived here could only be moderately strengthened by such a study, since the main effect is through the background evolution rather than the perturbations, as discussed in appendix B.

Figure 12 shows the impact of massless ghosts and massive sterile neutrinos on the CMB temperature anisotropies and on the matter power spectrum, for $\Omega_g = 0.6$ and $w_{\nu_s} = 0.02$. To highlight the effects of the new parameters, those of Λ CDM are fixed at their Planck 2018 best-fit values. (Note that Ω_Λ is derived from the flatness assumption and is not a fundamental parameter in Λ CDM.) The features in Fig. 12 differ qualitatively from those where $m_{\nu_s} = 0$, Fig. 8. In the CMB spectrum, there are two main effects: an overall shift of the CMB acoustic peaks toward smaller angular scales (larger ℓ) and an increase of the late ISW contribution at large scales.

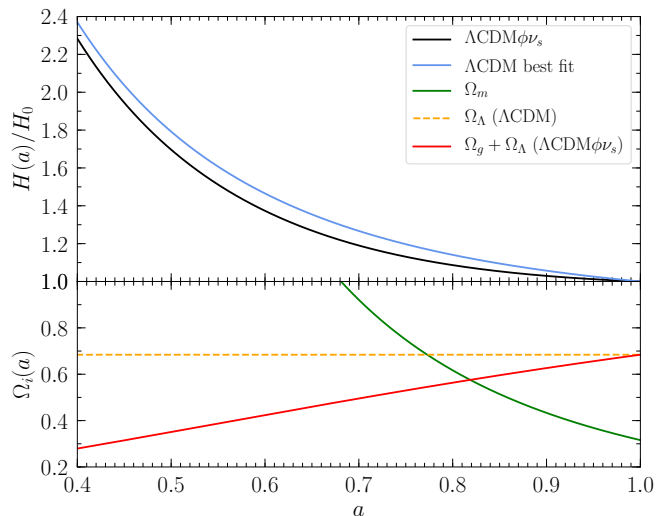


FIG. 13. Late-time evolution of (Top) the Hubble parameter $H(a)$ normalized to its present-day value H_0 , and (Bottom) the energy densities of the main species normalized to the critical density of the Universe today. Parameter values are as in Fig. 12. Red curve is the total dark energy density, $\Omega_\Lambda + \Omega_g$.

IV.2.1. Acoustic peak shift

The peak shift comes from the decrease of the dark-energy abundance Ω_Λ [37] (a derived parameter in Λ CDM), which is required to preserve spatial flatness. If one simultaneously keeps the other Λ CDM parameters fixed to their Planck best-fit values,¹⁴ the Hub-

¹⁴ In our model, the preferred values of H_0 and Ω_m change by relatively smaller amounts than Ω_Λ and have a subdominant

ble rate $H(a)$ in Eq. (18) decreases relative to the standard scenario because the density of the new species becomes significant only at late times, as shown in Fig. 13 (top). Since the age of the Universe is computed as $t = \int d \ln a / H(a)$, reducing $H(a)$ results in an older universe, and the thermal history, including photon decoupling, has to occur earlier in the past relative to Λ CDM. This shifts the acoustic CMB peaks to smaller scales, as seen in Fig. 12 (left).

In detail, the location of the first acoustic peak is given by $\ell_s \simeq \pi / \theta_s^*$, where [37]

$$\theta_s^* = \frac{r_s^*}{D_A^*} \quad (36)$$

is the angular size of the sound horizon at the time of last scattering,

$$r_s^* = r_s(z_*) = \int_{z_*}^{\infty} \frac{dz}{H(z)} c_s(z) \quad (37)$$

is the sound horizon with $c_s(z)$ the sound speed of the photon-baryon fluid, and

$$D_A^* \equiv D_A(z_*) = \int_0^{z_*} \frac{dz}{H(z)} \quad (38)$$

is the comoving angular diameter distance between the last-scattering surface at redshift z_* and today. A decrease of Ω_Λ does not affect the sound horizon r_s^* , since it depends only on the physics before the time of photon decoupling, when the dark energy and the new species were negligible, but it does affect D_A^* by reducing $H(z)$. Therefore, the comoving angular diameter distance increases with respect to Λ CDM, reducing the value of θ_s^* and shifting the location of the first CMB peak to larger ℓ .

IV.2.2. Late ISW enhancement

The second feature in the CMB temperature anisotropy spectrum, when nonrelativistic ν_s are included, is an increase in the late ISW contribution, which can be explained by the interplay of two competing phenomena: the behavior of the cosmological perturbations of ν_s and ϕ , and the decrease of Ω_Λ .

Fig. 14 (left) shows the large-scale evolution of the synchronous-gauge physical perturbations for the ghosts and sterile neutrinos. Similarly to the massless ν_s case, the physical shear perturbation $\rho_\phi \sigma_\phi$ for ghosts (blue dot-dashed line) dominates over that for sterile neutrinos (red dot-dashed curve), leading to an overall positive contribution to the total shear (green dot-dashed line) and a consequent decrease of the Newtonian potential Ψ ,

according to Eq. (33). The impact on the Newtonian curvature Φ from the perturbations of the new species is small, because the positive contribution of the density contrast δ , which is dominated by ν_s , is largely canceled by the negative contribution of the velocity perturbation θ , dominated by ϕ , as shown in Fig. 14 (left). The net effect on $(\Psi - \Phi)$, whose conformal time derivative enters the late ISW contribution in Eq. (32), is to drive it to more negative values on a shorter timescale, leading to an increase in the late ISW effect, as shown in Fig. 14 (right).

The situation is complicated by the decrease of Ω_Λ in the background density evolution, which tends to counteract the late ISW effect. The dark energy impacts the decay of the gravitational wells which photons traverse. In Λ CDM, the Newtonian curvature Φ and potential Ψ , which parameterize the depth of the gravitational wells, and remain constant during matter domination, but they start to decay when dark energy takes over, illustrated by the thin curves in Fig. 14 (right). This is due to the gravitational wells becoming shallower when the Universe starts accelerating, enhancing the late ISW effect. Conversely, the effect is diminished if Ω_Λ is reduced [37], attenuating the increase of the late ISW contribution arising from the ϕ and ν_s perturbations.

Which of these competing effects wins is determined by the relative values of Ω_Λ and Ω_g , due to the ν_s contribution to the latter. If $\Omega_\Lambda \gg \Omega_g$, the $\phi + \nu_s$ contribution becomes negligible and the late ISW effect is reduced. In general, we see that for relativistic sterile neutrinos, with $w_{\nu_s} \gtrsim 0.1$, the late ISW effect in the CMB temperature anisotropy spectrum decreases, similarly to the massless ν_s case.

IV.2.3. Spatial curvature

The previous discussion assumes that the Universe is spatially flat, which forces Ω_Λ to decrease with respect to the Planck prediction, whenever massive sterile neutrinos are produced. The presence of a positive curvature ($\Omega_k < 0$) might reduce the impact of the new species on the CMB spectrum since a nonzero curvature provides opposite effects to those seen here [37]. A closed universe could also reduce some discrepancies between the Λ CDM model and the Planck 2018 data [51, 52], although it is still unclear whether they might be due to internal systematics [53]. We leave the study of phantom fluids in a non-flat Universe for a future work.

IV.2.4. Matter power spectrum

As concerns the matter power spectrum, shown in Fig. 12 (right), the vacuum decay into massless ϕ and nonrelativistic massive ν_s leads to a suppression at all scales. The dominant effect is the free streaming of the new species, which occurs immediately after they are

effect on the peak shift.

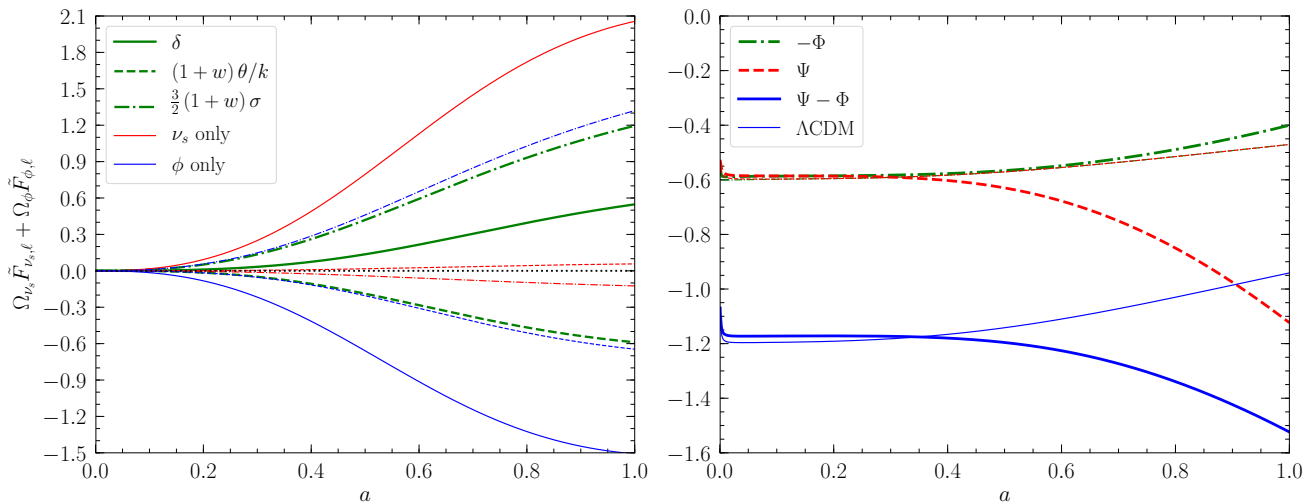


FIG. 14. Like Fig. 9, but for the massive ν_s case, with $w_{\nu_s} \simeq 0.02$ and $\Omega_g \simeq 0.6$.

produced, causing a damping of their density fluctuations compared to standard nonrelativistic species, such as CDM.

This is particularly important for sterile neutrinos, since they contribute to the total nonrelativistic matter and hence to the matter power spectrum. The density contrast for ν_s is smaller than that for CDM, $\delta_{\nu_s} < \delta_{\text{cdm}}$, due to the collision term (see Appendix B), whereas its energy density ρ_{ν_s} can be of the same order as ρ_m , but in any case it leads to $\delta\rho_{\nu_s} \lesssim \delta\rho_{\text{cdm}}$. Since the matter power spectrum is defined in terms of $\delta\rho_m/\rho_m$ to which both ν_s and CDM contribute, the net effect is a decrease of $P(k)$ relative to ΛCDM . This differs from massive SM neutrinos, where the suppression occurs only at scales smaller than the free-streaming length set by the time of relativistic-to-nonrelativistic transition [54]. Unlike SM neutrinos, the equation-of-state w_{ν_s} for ν_s from vacuum decay is approximately time-independent, depending only upon the value of m_{ν_s} .

However, the free streaming of ν_s is not the only effect on $P(k)$. Sterile neutrinos and ghosts contribute to the Friedmann equation and their abundance increases with time. If the ΛCDM parameters and H_0 are fixed at their Planck values, increasing Ω_g requires reducing Ω_Λ to keep the total dark energy unchanged. The net effect of the time evolution of $\Omega_g(a) + \Omega_\Lambda$ on the Friedmann equation is to lower the value of $H(a)$ (Fig. 13, upper plot) and to delay the transition from matter domination to the epoch when dark energy, including the $\phi + \nu_s$ fluid, started to dominate (Fig. 13, bottom plot). This allowed more matter to fall into gravitational wells and thereby enhance the matter power spectrum.

Similarly, the perturbations of the new species, and in particular the nonzero shear for ν_s and ϕ , tend to reduce the decay of the Newtonian gravitational potential Ψ and curvature Φ , leading to an increase of the matter clustering. This is a direct gravitational back-reaction

effect at the level of perturbations, which adds to the background effect discussed above, leading to an increase of $P(k)$ primarily affecting large angular scales, as in the case of massless ν_s .

For nonrelativistic massive ν_s , the free-streaming effect dominates over the background and back-reaction ones, as shown in Fig. 12 (right), producing less matter clustering. On the other hand, the latter two effects dominate in the case of relativistic or mildly relativistic massive ν_s , because such sterile neutrinos do not contribute to the total nonrelativistic matter and hence do not directly affect the matter power spectrum.

IV.2.5. Results

Similarly to the massless ν_s case, the MCMC code CosmoMC was used to constrain the two new parameters Ω_g and w_{ν_s} , and to study their correlations with the ΛCDM ones. We adopted the same convergence requirement and data sets as used for the $m_{\nu_s} = 0$ case, as described in subsection IV.1.1.

Figure 15 shows the correlations between the new parameters and those derived from ΛCDM that are significantly correlated. The latter include the total matter abundance Ω_m , which is separate from the ν_s contribution, the dark energy abundance Ω_Λ , the Hubble constant H_0 , and the clustering amplitude parameter $S_8 = \sigma_8\sqrt{\Omega_m/0.3}$. The extended version of the correlation parameter plot shown in Fig. 15 is discussed in Appendix C, including a table with the 68% C.L. limits.

Increasing Ω_g , defined as the present-day energy fractions of ϕ plus ν_s , leads to an increase in H_0 , which can be intuitively understood by the phantom nature of the effective $\phi + \nu_s$ fluid. Its equation of state w_{eff} was found to be < -1.3 (Fig. 7), more negative than that of the cosmological constant. Therefore, increasing the relative

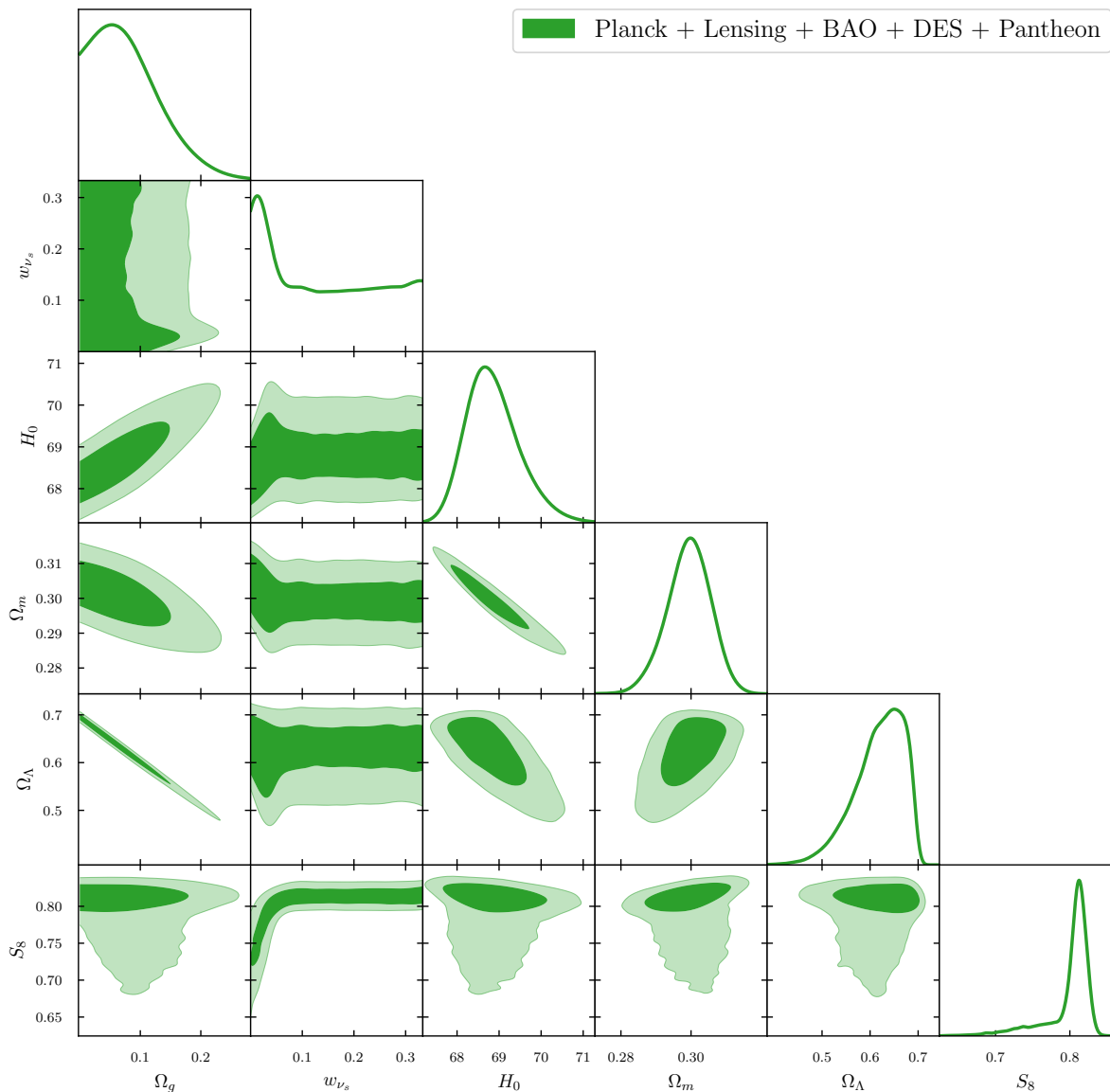


FIG. 15. Correlations between the Λ CDM $\phi\nu_s$ model parameters, as inferred from CosmoMC for massive ν_s , valid independently of the mediator model used. The data sets Planck + Lensing + BAO + DES + Pantheon are the same as described in subsection IV.1.1. The darker and lighter green shaded regions correspond to the 68% and 95% C.L. intervals, respectively.

abundance of the phantom fluid causes the Universe to expand faster today than in the Λ CDM model, leading to a larger value of H_0 .

Such accelerated expansion entails weaker growth of large scale structure, which is parameterized by $S_8 = \sigma_8 \sqrt{\Omega_m}/0.3$, where σ_8 is the linear-theory standard deviation of matter density fluctuations in a sphere of radius $8 h^{-1}$ Mpc. Namely, Fig. 15 shows a slow decrease in the parameter S_8 with increasing H_0 , which is most pronounced at small values of w_{ν_s} . This confirms the observation made in subsection IV.2.4, where the decrease of the amplitude of the matter power spectrum (and hence σ_8 and S_8) was observed for nonrelativistic massive ν_s . We will quantitatively discuss the implications of those

findings for H_0 and S_8 in the next subsection, devoted to possible resolutions of known cosmological tensions.

Another striking correlation is the decrease of both Ω_Λ and Ω_m as the present-day abundance of the new species increases. The former effect derives from the flatness condition $\Omega_\Lambda + \Omega_m + \Omega_g = 1$. Although Ω_m is also a derived parameter in Λ CDM, it is determined by $\Omega_b h^2$ and $\Omega_c h^2$, which are constrained by the relative heights of the CMB peaks [55]. Since our model affects only the late-time evolution and hence does not alter photon decoupling, whose physics impacts the peak height, the value of $(\Omega_b + \Omega_c) h^2$ remains nearly unchanged relative to Λ CDM. This is verified in the extended correlation plot in Appendix C. Consequently, the decrease in Ω_m with

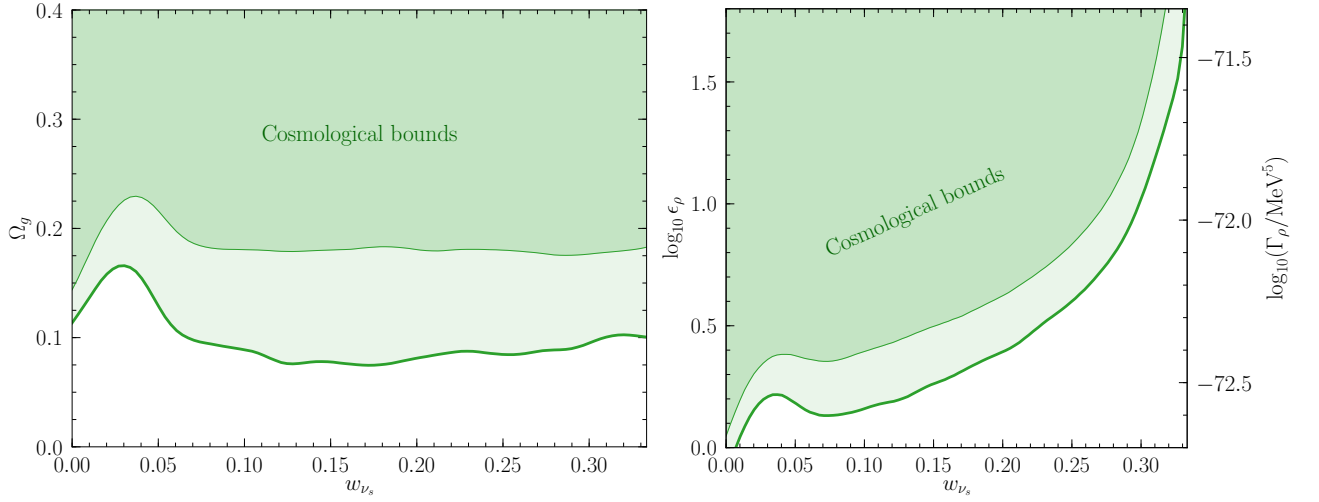


FIG. 16. *Left*: Constraints on $\Omega_g = (\rho_\phi + \rho_{\nu_s})/\rho_{\text{crit}}$ versus $w_{\nu_s} = P_{\nu_s}/\rho_{\nu_s}$ for the massive ν_s scenario, derived from Fig. 15. *Right*: Corresponding excluded regions in the plane of $\epsilon_\rho = \Gamma_\rho/(3H_0\rho_{\text{crit}})$, the dimensionless vacuum decay rate in the Boltzmann equations (25), and w_{ν_s} . (Right axis shows $\log_{10} \Gamma_\rho$ in MeV^5 units.) In both plots, the thick and thin curves show the respective 68% and 95% C.L. exclusion limits.

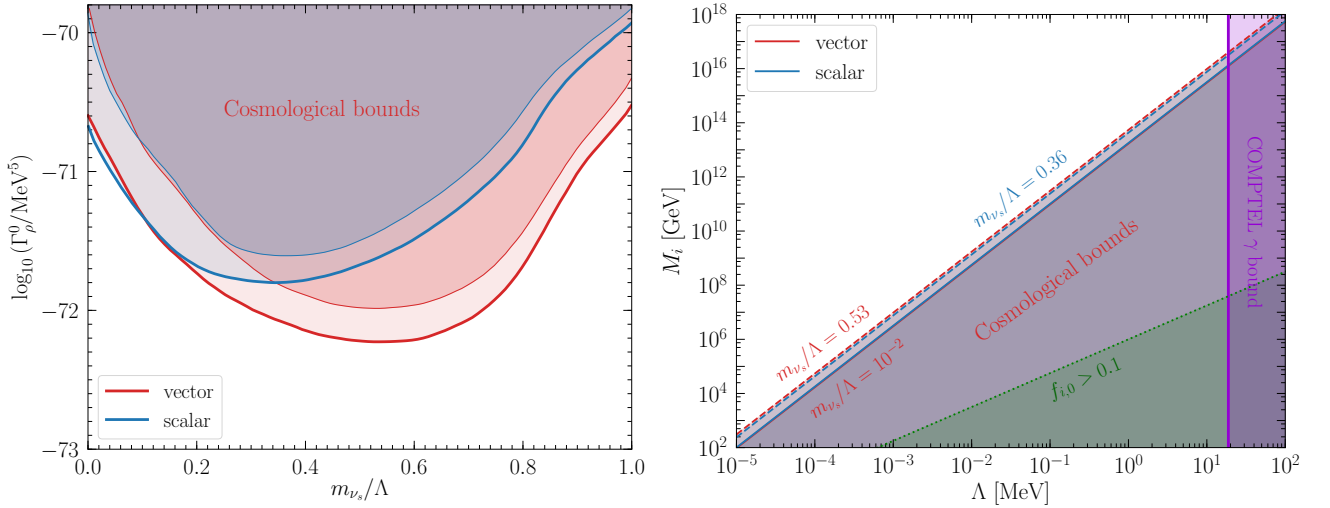


FIG. 17. *Left*: Mapping of excluded regions of Fig. 16 (left) to the microphysics quantities $\Gamma_\rho^0 \equiv \Gamma_\rho|_{m_{\nu_s}=0}$ (the vacuum decay rate) and m_{ν_s}/Λ , for vector (red) and scalar (blue) mediator models. Thick (thin) curves show the 68% (95%) C.L. exclusion limits. *Right*: 95% C.L. bounds on the parameters M_i (the mediator mass scale, with $i = s, v$), versus the ghost momentum cutoff Λ , corresponding to the left plot. Solid lines correspond to $m_{\nu_s}/\Lambda = 10^{-2}$, and dashed to the values that give the strongest constraints, namely $m_{\nu_s}/\Lambda \simeq 0.53$ (0.36) for the vector (scalar) mediator case.

increasing Ω_g comes mostly from the growth of H_0 , as explained above.

For constraining Ω_g and w_{ν_s} , which are taken as independent input parameters, the second-from-top left plot of Fig. 15 displays their allowed values. It shows that Ω_g is roughly independent of w_{ν_s} , which can be understood from the definition of Ω_g as the net amount of $\rho_{\nu_s} + \rho_\phi$ that has been produced, whose value already incorporates the effect of w_{ν_s} . In the limit of $m_{\nu_s} \rightarrow 0$, $w_{\nu_s} \rightarrow 1/3$, with Γ_ρ fixed, it is true that Ω_g would be

driven to zero, but in the Ω_g - w_{ν_s} parametrization, Γ_ρ is not fixed and the former are independent of each other. In fact, w_{ν_s} does not correlate strongly with the other Λ CDM parameters either. Its main effect is on the linear perturbations. At the more important level of the homogeneous energy densities, w_{ν_s} has a relatively small impact.

The 68% and 95% C.L. exclusion plots for Ω_g and w_{ν_s} corresponding to Fig. 15 are shown in Fig. 16 (left). We also map them onto the plane of w_{ν_s} and $\epsilon_\rho =$

$\Gamma_\rho/(3H_0\rho_{\text{crit}})$, or directly Γ_ρ , using Eq. (26) and Fig. 15. The resulting limits, shown in Fig. 16 (right), resemble those obtained from the supernova analysis of section III.5, Fig. 7 (left). As expected, large values of Γ_ρ are allowed as $w_{\nu_s} \rightarrow 1/3$, since Ω_g can remain fixed in that limit.

Using Eqs. (A6), (23), and (24), one can constrain $\Gamma_\rho^0 \equiv \Gamma_\rho|_{m_{\nu_s}=0}$ versus m_{ν_s}/Λ . This is shown in Fig. 17 (left) for the vector and scalar mediator models. It does not correspond to independent bounds on the microphysical parameters Λ and M_i , since cosmological observables are sensitive to the derived combination Γ_ρ^0 . However we can use Eqs. (23) and (A6), together with the bounds on Γ_ρ^0 , to limit M_i as a function of Λ , for fixed values of m_{ν_s}/Λ , as shown in Fig. 17 (right).

Analytically, the new physics mass scales are bounded from below as

$$M_i \gtrsim (1-5) \times 10^{13} \left(\frac{\Lambda}{\text{MeV}} \right)^{2.25} \text{ GeV} \quad (39)$$

for neutrino masses $m_{\nu_s}/\Lambda \gtrsim 0.01$. The strongest limits occur for particular values of $m_{\nu_s}/\Lambda \simeq 0.53$ (0.36) for the vector (scalar) mediator respectively. As expected, these bounds are much stronger than those in the massless ν_s scenario, (section IV.1.1), resulting mainly from modifications at the background level, as opposed to perturbations. They depend weakly on m_{ν_s}/Λ , since Γ_ρ^0 in Fig. 17 (left) changes by at most few orders of magnitude from varying m_{ν_s} .

IV.3. Cosmological tensions

In recent years, discrepancies have emerged among various observational probes regarding the values of certain cosmological parameters. The most notable one is the Hubble tension, which refers to a mismatch between early-time and late-time estimations of the Hubble constant H_0 [50, 56–67]. This tension has crossed the critical 5σ level between the two most precise measurements: Planck finds $H_0 = 67.66 \pm 0.42$ km/s/Mpc [24] from fitting the CMB data within the Λ CDM framework, whereas SH0ES finds $H_0 = 73.04 \pm 1.04$ km/s/Mpc [68] based on the distance-ladder approach.¹⁵ A milder tension also exists concerning the large-scale structure of the Universe [47, 70–76]. Estimations of the amplitude of late-time matter fluctuations S_8 from galaxy redshift surveys are consistently lower than those inferred from CMB data, which points to $S_8 = 0.825 \pm 0.011$ [24], assuming the Λ CDM model. The most recent late-time measurement $S_8 = 0.790^{+0.018}_{-0.014}$, from the DES Y3+KIDS-1000 surveys [77], agrees with the Planck value within the $\sim 2\sigma$ level.

¹⁵ A recent determination of H_0 from late-time measurements can be found in Ref. [69].

Parameter	Λ CDM	Λ CDM $\phi\nu_s$	
		solve tensions	best fit
$\Omega_b h^2$	0.02246	0.02222	0.02250
$\Omega_c h^2$	0.1192	0.1182	0.1185
$100 \theta_{\text{MC}}$	1.04093	1.04087	1.04119
τ	0.0530	0.0609	0.05817
$\ln(10^{10} A_s)$	3.040	3.0593	3.0468
n_s	0.9636	0.9639	0.9667
Ω_g	0.0001	0.3934	0.1430
w_{ν_s}	0.2480	0.2811	0.0548
H_0 /[km/s/Mpc]	67.70	72.71	69.76
Ω_Λ	0.6893	0.3397	0.5659
Ω_m	0.3106	0.2669	0.2911
σ_8	0.8062	0.8556	0.8118
S_8	0.820	0.807	0.800
$\log_{10}(\Gamma_\rho^0/\text{MeV}^5)$	-75.26 (v) -75.02 (s)	-71.51 (v) -71.38 (s)	-71.81 (v) -70.87 (s)
m_{ν_s}/Λ	0.331 (v) 0.320 (s)	0.249 (v) 0.235 (s)	0.805 (v) 0.820 (s)
$w_{\text{eff}}(z=0)$	-1.2925	-1.3462	-1.3128
χ^2_{Planck}	2780.5	2790.0	2780.3
χ^2_{Lensing}	9.2	8.4	8.8
χ^2_{BAO}	5.7	17.9	7.4
χ^2_{DES}	523.4	510.8	512.0
χ^2_{Pantheon}	1035.0	1053.1	1036.5
χ^2_{tot}	4353.8	4380.2	4345.0
$\Delta\chi^2$	0	+26.4	-8.8

TABLE II. Cosmological parameters for Λ CDM (second column), for the preferred Λ CDM $\phi\nu_s$ model solving both the H_0 and S_8 tensions (third column), and for the best-fit Λ CDM $\phi\nu_s$ model found in the full MCMC scan, Fig. 15 (last column). The first six rows are the Λ CDM parameters, and the following two are the new-physics parameters. The remaining ones are derived from the cosmological model. (v), (s) indicate vector and scalar mediator models, respectively. Bottom rows give the χ^2 contribution from each data set, the total χ^2_{tot} , and $\Delta\chi^2 \equiv \chi^2_{\text{tot}} - \chi^2_{\Lambda\text{CDM}}$.

This motivates us to reconsider our main results for the parameter distributions, Fig. 15, with respect to the cosmological tensions. In particular, we want to determine whether there exist models within the Λ CDM $\phi\nu_s$ scenario that can ameliorate the tensions, while remaining compatible with all the cosmological data. Figure 18 shows the same correlation plot between the parameters as in Fig. 15, restricted to those models that resolve the H_0 and S_8 tensions within the 1σ level. Interestingly, both tensions can be resolved in a narrow region of the parameter space with $w_{\nu_s} \sim 0.3$ and $\Omega_g \sim 0.3-0.5$, forcing both Ω_Λ and Ω_m to decrease from their Planck 2018 best-fit values. In our MCMC chains, only about 0.015% of the models can address both tensions, while keeping a total χ^2 comparable to that of the Λ CDM model.

However, this does not constitute a successful resolution of the $H_0 + S_8$ tensions, because it comes at the expense of creating new ones. In Table II we compare the goodness of the fit for these models (third column) to Λ CDM (second column). Although the fit to Dark Energy Survey (DES) data improves, that to Planck, BAO

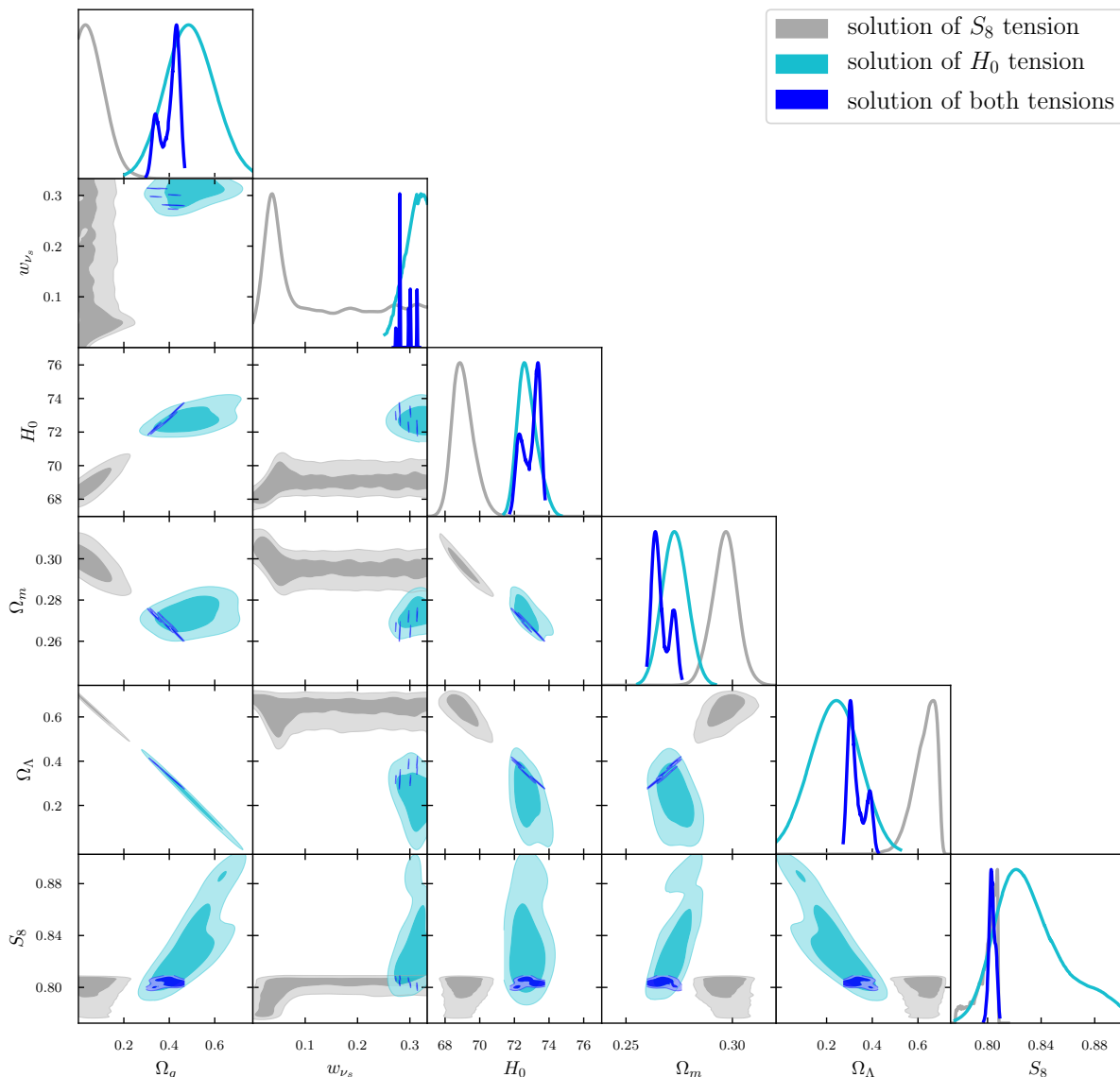


FIG. 18. Correlations between the $\Lambda\text{CDM}\phi\nu_s$ parameters for the models addressing the H_0 and S_8 tensions, selected from the full MCMC scan shown in Fig. 15. Gray regions solve only the S_8 tension, cyan addresses only the H_0 tension, and blue indicates models ameliorating both. Darker and lighter regions correspond to the 68% and 95% C.L. intervals, respectively.

and Pantheon degrades, resulting in a significantly worse global fit, with $\Delta\chi^2 \simeq 26$.

Nevertheless, we find that the $\Lambda\text{CDM}\phi\nu_s$ model can ameliorate the H_0 tension to the $\sim 3\sigma$ level, with $H_0 \simeq 69.8$ km/s/Mpc, while simultaneously addressing the S_8 tension. This is shown in the third column of Table II, for the best-fit $\Lambda\text{CDM}\phi\nu_s$ model. Coincidentally, this model predicts $\Omega_g \sim 0.15$, which is the same value that was preferred by the Pantheon type Ia supernovae in Fig. 6. The net improvement of $\Delta\chi^2 = -8.8$ relative to ΛCDM provides a mild preference of the ghost model, based on the Akaike and Bayesian Information Criteria [78, 79]. Similar conclusions were drawn in Ref. [80] applied to generic phantom dark energy models.

V. CONCLUSIONS

In this work, we have reconsidered the cosmological consequences of a phantom field, a scalar with the wrong-sign kinetic term. Such a theory must be a low-momentum effective description, valid below some cutoff Λ . We refined a previous estimated upper limit to show that $\Lambda \lesssim 19$ MeV, from observational constraints on diffuse gamma rays. At higher scales, phantom models must revert to a theory with normal-sign kinetic terms.

Unlike the great majority of phantom dark energy studies, we assumed the vacuum expectation value of the field vanishes, so that its potential makes no contribution to the Hubble expansion. Instead, the spontaneous

breakdown of the vacuum into phantom particles plus normal ones produces a fluid that behaves as dark energy, as long as there is a mismatch between the masses of the two kinds of particles. We showed that the equation of state of this exotic “ghost fluid” always violates the null energy condition (NEC), since it lies in the interval $-1.3 \lesssim w_{\text{eff}} < -1.5$ at all times (see Fig. 7, right). Therefore, even if at the present time the net contribution of the ghost fluid to the energy budget of the Universe is small, $\Omega_g \ll 1$, eventually it will come to dominate over the cosmological constant. However since the phantom theory is only an effective description valid below the scale Λ , the usual “big rip” singularity that would occur in the future [81] is avoided. Nevertheless, the accelerated expansion that occurs before the cutoff is reached will be sufficient to disrupt any object whose density falls below Λ^4 . For example, the sun would be ripped apart if $\Lambda \gtrsim 10 \text{ keV}$.

We found that the NEC-violating equation of state is at odds with combined cosmological data if one tries to make the ghost fluid account for all of the dark energy. Instead, there is an upper bound $\Omega_g \lesssim 0.2$, requiring it to be subdominant to the contribution from cosmological constant, $0.5 \lesssim \Omega_\Lambda \leq 0.7$.

Such large values of Ω_g cannot be attained if the phantoms couple with only gravitational strength to other particles. Instead, we allowed for stronger interactions, mediating the production of phantoms plus light dark matter (with mass $< \Lambda$). It leads to a larger Hubble rate at late times, in the case of massless phantoms, since the negative ghost energy redshifts faster than the positive dark matter density. This constant rate of creation of energy density is reminiscent of the old steady-state cosmology [82, 83], with the difference that the present mechanism is rooted in quantum field theory, rather than an *ad hoc* assumption. Naively, one might think it could resolve the Hubble tension, but we find that this exacerbates the S_8 tension, as expected on general grounds for late-time mechanisms [84, 85] (see however Refs. [86–88]). The best-fit phantom model does soften the H_0 tension, reducing it to $\sim 3\sigma$, and it provides a mild im-

provement relative to ΛCDM in fitting the data sets.

A special case is where massless phantoms couple to massless dark radiation with strength exceeding that of gravity. Then their energy densities cancel exactly, and the magnitude of each can exceed usual bounds on a new light species by many orders of magnitude, since there is no impact on the Hubble expansion. Nevertheless, linear-order cosmological perturbations grow in this scenario, and provide constraints via the ISW effect. In the extreme case where the cutoff Λ saturates the gamma-ray bound, and the new-physics scale coupling ghosts to dark radiation is $M \sim 10^{10} \text{ GeV}$, the dark radiation could contribute as much as $\Omega_{\nu_s} \sim 10^{26}$ (see Fig. 10), being canceled by the negative contribution of the ghosts.

In a companion paper, we considered a possible observable effect of such a large density of dark radiation, whose energy is of order the cutoff Λ : in the presence of an additional interaction coupling it to electrons, it could be seen in direct detection experiments [89]. It would be interesting to identify other potentially observable consequences of such a large population of energetic particles in the late Universe. For example, there could be a mismatch between the preferred reference frame of the ghost fluid and that of the CMB, which for simplicity we neglected in the present study.

Acknowledgments. We thank G. Alonso-Alvarez, J. Ambjörn, H. Bernardo, R. Brandenberger, S. Caron-Huot, B. Gavela, K. Rogers, K. Schutz, and M. Toomey for discussions, and T. Brinckmann, A. Lewis, L. Lopez-Honorez, A. Singal, and S. Vagnozzi for very helpful correspondence. We acknowledge Calcul Québec (<https://www.calculquebec.ca>) and Digital Research Alliance of Canada (<https://alliancecan.ca>) for supercomputing resources. JC and MP are supported by NSERC (Natural Sciences and Engineering Research Council, Canada). MP was also partially supported by the Arthur B. McDonald Institute for Canadian astroparticle physics during the initial stages of the project. TT is supported by JSPS Grant-in-Aid for Scientific Research KAKENHI Grant No. JP23H04004.

Appendix A: Computation of vacuum decay rate per unit volume

In this appendix the integral in Eq. (5) is evaluated, which generalizes the computation of Section II when the produced particles (apart from the ghosts) are massive. Eliminating the integral over \vec{p}_4 through the three-dimensional delta function, the vacuum decay rate into massless ghosts and massive sterile neutrinos is

$$\Gamma = \frac{1}{16(2\pi)^8} \int \frac{d^3 p_1}{p_1} \int \frac{d^3 p_2}{p_2} \int \frac{d^3 p_3}{E_3} \left(\frac{|\mathcal{M}|^2}{E_4} \right)_{\vec{p}_4 \rightarrow \vec{p}_1 + \vec{p}_2 - \vec{p}_3} \delta\left(p_1 + p_2 - E_3 - \sqrt{(\vec{p}_1 + \vec{p}_2 - \vec{p}_3)^2 + m_{\nu_s}^2}\right) \times \Theta(\Lambda - p_1) \Theta(\Lambda - p_2), \quad (\text{A1})$$

where $p_i = |\vec{p}_i|$. The two Heaviside functions restrict the ghost momenta to lie below the cutoff. The sterile neutrinos (with momenta p_3, p_4) are assumed to be Dirac fermions and the ghosts (momenta p_1, p_2) are complex scalars. For real scalar ghosts, an extra factor of $1/2$ should be included.

Using rotational invariance to make \vec{p}_1 parallel to \hat{z} and \vec{p}_2 to lie in the \hat{x} - \hat{z} plane, the measure becomes

$$\frac{d^3 p_1}{p_1} \frac{d^3 p_2}{p_2} \frac{d^3 p_3}{E_3} = 4\pi p_1 dp_1 2\pi p_2 dp_2 dc_{12} p_3 dE_3 dc_{13} d\varphi_3, \quad (\text{A2})$$

where $c_{jk} \equiv \cos \theta_{jk}$ for $j, k = 1, 2, 3$, and we used $p_i dp_i = E_i dE_i$. Hence

$$\begin{aligned} \Gamma &= \frac{1}{8(2\pi)^6} \int_0^\Lambda dp_1 p_1 \int_0^\Lambda dp_2 \int_{-1}^1 dc_{12} \int_{-1}^1 dc_{13} \int dE_3 \int d\varphi_3 \frac{p_2 p_3}{E_4} |\mathcal{M}|_{\vec{p}_4 \rightarrow \vec{p}_1 + \vec{p}_2 - \vec{p}_3}^2 \\ &\times \delta\left(p_1 + p_2 - E_3 - \sqrt{(\vec{p}_1 + \vec{p}_2 - \vec{p}_3)^2 + m_{\nu_s}^2}\right). \end{aligned} \quad (\text{A3})$$

Using the remaining delta function to solve for φ_3 gives

$$\delta(\dots) = \delta\left(p_1 + p_2 - E_3 - \sqrt{p_1^2 + p_2^2 + E_3^2 + 2p_1 p_2 c_{12} - 2p_1 p_3 c_{13} - 2p_2 p_3 c_{23}}\right) \equiv \delta(g(\cos \varphi_3)), \quad (\text{A4})$$

where $c_{23} = c_{12} c_{13} + s_{12} s_{13} \cos \varphi_3$, with $s_{jk} \equiv \sin \theta_{jk}$. Here $\delta(g(x)) = \sum_{x_s} \delta(x - x_s) / |g'(x_s)|$, where x_s are the roots of $g(x)$. In this case the single root is

$$(\cos \varphi_3)_0 = -\frac{p_1 p_2 (1 - c_{12}) - p_1 (E_3 - p_3 c_{13}) - p_2 (E_3 - p_3 c_{12} c_{13})}{p_2 p_3 s_{12} s_{13}}, \quad (\text{A5})$$

with $g'(\cos \varphi_3) = (p_2 p_3 / E_4) s_{12} s_{13}$. Using $dc_{jk} = -s_{jk} d\theta_{jk}$, the decay rate integrals reduce to

$$\begin{aligned} \Gamma &= \frac{1}{8(2\pi)^6} \int_0^\Lambda dp_1 p_1 \int_0^\Lambda dp_2 \int_0^\pi d\theta_{12} \int_0^\pi d\theta_{13} \int_{m_{\nu_s}}^{2\Lambda - m_{\nu_s}} dE_3 \int d\varphi_3 |\mathcal{M}|^2 \delta(\cos \varphi_3 - (\cos \varphi_3)_0) \\ &= \frac{\Lambda^4}{4(2\pi)^6} \int_0^1 dx_1 x_1 \int_0^1 dx_2 \int_0^\pi d\theta_{12} \int_0^\pi d\theta_{13} \int_{\frac{m_{\nu_s}}{\Lambda}}^{2 - \frac{m_{\nu_s}}{\Lambda}} dy_3 \frac{\Theta(1 - |(\cos \varphi_3)_0|)}{|\sin \varphi_3|} |\mathcal{M}|^2, \end{aligned} \quad (\text{A6})$$

where $x_j \equiv p_j / \Lambda$, $y_j \equiv E_j / \Lambda$ and there is a factor of 2 for the two values of φ_3 satisfying Eq. (A5). The upper limit on E_3 comes from energy conservation with $p_4 = 0$, the maximum energy allowed by kinematics.

If vacuum decay is mediated by gravitons, the matrix element (4) is

$$|\mathcal{M}_g|^2 = -\frac{\Lambda^4}{32 m_p^4} \left\{ \frac{[\hat{t} - (m_{\nu_s} / \Lambda)^2][\hat{s} + \hat{t} - (m_{\nu_s} / \Lambda)^2][\hat{s} + 2\hat{t} - (m_{\nu_s} / \Lambda)^2]^2}{\hat{s}^2} \right\}, \quad (\text{A7})$$

with $\hat{s} = 2x_1 x_2 (1 - c_{12})$, $\hat{t} = (m_{\nu_s} / \Lambda)^2 - 2x_1 (y_3 - x_3 c_{13})$ are the usual Mandelstam variables divided by Λ^2 and $x_3 \equiv \sqrt{y_3^2 - (m_{\nu_s} / \Lambda)^2}$. Numerically solving the integrals in Eq. (A6) with $|\mathcal{M}_g|^2$ using Vegas [90, 91], we find the analytic fit

$$\Gamma_g \approx 8.9 \times 10^{-9} \frac{\Lambda^8}{m_p^4} \left[1 - \left(\frac{m_{\nu_s}}{\Lambda} \right)^2 \right] \exp \left[-5.3 \left(\frac{m_{\nu_s}}{\Lambda} \right)^{4.2} \right]. \quad (\text{A8})$$

for $m_{\nu_s} \leq \Lambda$.

For the scalar mediator, $|\mathcal{M}_n|^2$ in Eq. (9) simplifies to

$$|\mathcal{M}_s|^2 = 4 \frac{\Lambda^4}{M_s^4} \left[x_1 x_2 (1 - c_{12}) - 2(m_{\nu_s} / \Lambda)^2 \right], \quad (\text{A9})$$

and the result for the corresponding decay rate is

$$\Gamma_s \approx 1.1 \times 10^{-5} \frac{\Lambda^8}{M_s^4} \exp \left[-6.7 \left(\frac{m_{\nu_s}}{\Lambda} \right)^{2.1} \right]. \quad (\text{A10})$$

Similarly, for the vector mediator, the matrix element (A6) is

$$|\mathcal{M}_v|^2 = 32 \frac{\Lambda^4}{M_v^4} x_1^2 \left[y_3 (x_2 - y_3) + x_3 (2y_3 - x_2) c_{13} - x_3^2 c_{13}^2 - x_2 c_{12} (y_3 - x_3 c_{13}) \right], \quad (\text{A11})$$

leading to a vacuum decay rate

$$\Gamma_v \approx 1.1 \times 10^{-5} \frac{\Lambda^8}{M_v^4} \exp \left[-5.7 \left(\frac{m_{\nu_s}}{\Lambda} \right)^{4.2} \right]. \quad (\text{A12})$$

Appendix B: Derivation of Boltzmann equations and hierarchies

In this appendix, we derive the Boltzmann equations describing the evolution of the background densities for ghosts and sterile neutrinos and their perturbations at linear order. Following Refs. [34, 92], the phase-space distribution for the particle species i is a background homogeneous contribution f_i^0 plus a perturbation,

$$f_i(\vec{x}, \vec{p}_i, \tau) = f_i^0(q_i, \tau) [1 + \Psi_i(\vec{x}, \vec{q}_i, \tau)], \quad (\text{B1})$$

where τ is the conformal time, related to the physical time t by $d\tau = dt/a(t)$, with a the scale factor, $\vec{q}_i \equiv a\vec{p}_i$ is the comoving three-momentum with magnitude $|\vec{q}_i| = q_i$ and unit-vector direction \hat{q}_i , and $\Psi_i(\vec{x}, \vec{q}_i, \tau)$ is the phase-space density contrast. The phase-space distribution evolves according to the Boltzmann equation, which is generically given in terms of the comoving momentum by

$$\frac{df_i}{d\tau} = \frac{\partial f_i}{\partial \tau} + \frac{q_i}{\varepsilon_i} \hat{q}_i \cdot \nabla_{\vec{x}} f_i + \frac{dq_i}{\partial \tau} \frac{\partial f_i}{\partial q_i} = \left(\frac{df_i}{d\tau} \right)_c, \quad (\text{B2})$$

where $\varepsilon_i = \sqrt{q_i^2 + a^2 m_i^2} = aE_i$ is the comoving energy and we neglected the term proportional to the derivative of f_i with respect to the direction \hat{q}_i , it being a second-order quantity. Putting Eq. (B1) into Eq. (B2) gives at the background level

$$\frac{\partial f_i^0}{\partial \tau}(q_i, \tau) = \left(\frac{df_i}{d\tau} \right)_c^{(0)}(q_i, \tau), \quad (\text{B3})$$

and at the linear-perturbation level

$$\frac{\partial \Psi_i}{\partial \tau}(\vec{x}, \vec{q}_i, \tau) + \frac{q_i}{\varepsilon_i} \hat{q}_i \cdot \nabla_{\vec{x}} \Psi_i(\vec{x}, \vec{q}_i, \tau) + \frac{dq_i}{d\tau} \frac{\partial \ln f_i^0}{\partial q_i} = \frac{1}{f_i^0} \left(\frac{df_i}{d\tau} \right)_c^{(1)} - \frac{1}{f_i^0} \left(\frac{df_i}{d\tau} \right)_c^{(0)} \Psi_i(\vec{x}, \vec{q}_i, \tau), \quad (\text{B4})$$

where $\left(\frac{df_i}{d\tau} \right)_c^{(1)}$ is the perturbed collision term. On the right-hand side of Eq. (B4) we used Eq. (B3) to replace the time-derivative of f_i^0 with the zeroth-order collision term. Equation (B3) reduces to Eq. (11) in terms of the physical time t and momentum p_i , and identifying $S_i \equiv \left(\frac{df_i}{d\tau} \right)_c^{(0)}$.

It is common practice to decompose Ψ_i into Legendre polynomials $P_\ell(\hat{k} \cdot \hat{q}_i)$, motivated by left-hand side of Eq. (B4) depending only on q_i , $k = |\vec{k}|$ and $\hat{k} \cdot \hat{q}_i$ in Fourier space. Hence [34]

$$\begin{aligned} \Psi_i(\vec{k}, \vec{q}_i, \tau) &= \sum_{\ell=0}^{\infty} (-i)^\ell (2\ell + 1) \Psi_{i,\ell}(k, q_i, \tau) P_\ell(\hat{k} \cdot \hat{q}_i), \\ \Psi_{i,\ell}(k, q_i, \tau) &= \frac{i^\ell}{2} \int_{-1}^1 d(\hat{k} \cdot \hat{q}_i) \Psi_i(\vec{k}, \vec{q}_i, \tau) P_\ell(\hat{k} \cdot \hat{q}_i). \end{aligned} \quad (\text{B5})$$

This allows the Fourier version of Eq. (B4) to be expressed as a hierarchy of equations for the multipole moments $\Psi_{i,\ell}(k, q_i, \tau)$ [34, 93]

$$\begin{aligned} \Psi'_{i,0}(k, q_i, \tau) &= -\frac{q_i k}{\varepsilon_i} \Psi_{i,1}(k, q_i, \tau) + \frac{1}{6} \frac{\partial \ln f_i^0}{\partial \ln q_i} h' + \mathcal{C}_0^{(1)}[\Psi_i(k, q_i, \tau)], \\ \Psi'_{i,1}(k, q_i, \tau) &= \frac{q_i k}{3\varepsilon_i} \left(\Psi_{i,0}(k, q_i, \tau) - 2\Psi_{i,2}(k, q_i, \tau) \right) + \mathcal{C}_1^{(1)}[\Psi_i(k, q_i, \tau)], \\ \Psi'_{i,2}(k, q_i, \tau) &= \frac{q_i k}{5\varepsilon_i} \left(2\Psi_{i,1}(k, q_i, \tau) - 3\Psi_{i,2}(k, q_i, \tau) \right) - \frac{\partial \ln f_i^0}{\partial \ln q_i} \frac{h' + 6\eta'}{15} + \mathcal{C}_2^{(1)}[\Psi_i(k, q_i, \tau)], \\ \Psi'_{i,\ell>2}(k, q_i, \tau) &= \frac{k}{2\ell + 1} \frac{q_i}{\varepsilon_i} [\ell \Psi_{i,\ell-1}(k, q_i, \tau) - (\ell + 1) \Psi_{i,\ell+1}(k, q_i, \tau)] + \mathcal{C}_\ell^{(1)}[\Psi_i(k, q_i, \tau)], \end{aligned} \quad (\text{B6})$$

where the collision-term multipoles are [93]

$$\mathcal{C}_\ell^{(1)}[\Psi_i(k, q_i, \tau)] \equiv \frac{1}{f_i^0} \left(\frac{df_i}{d\tau} \right)_{c,\ell}^{(1)}(k, q_i, \tau) - \frac{1}{f_i^0} \left(\frac{df_i}{d\tau} \right)_c^{(0)} \Psi_{i,\ell}(k, q_i, \tau), \quad (\text{B7})$$

and

$$\left(\frac{df_i}{d\tau}\right)_{c,\ell}^{(1)}(k, q_i, \tau) \equiv \frac{i^\ell}{4\pi} \int d\Omega_{\vec{k}} P_\ell(\hat{k} \cdot \hat{q}_i) \left(\frac{df_i}{d\tau}\right)_c^{(1)}(\vec{k}, \vec{q}_i, \tau), \quad (\text{B8})$$

with $\Omega_{\vec{k}}$ the solid angle subtended by the wave vector \vec{k} .

The collision term for sterile neutrinos ν_s on the right-hand side of Eq. (B2) comes from the vacuum decay into $\phi\phi\nu_s\bar{\nu}_s$, which has the same matrix element as the scattering process $\phi(q_1, \vec{q}_1)\phi(q_2, \vec{q}_2) \leftrightarrow \nu_s(\varepsilon_3, \vec{q}_3)\nu_s(\varepsilon_4, \vec{q}_4)$ when the ghost energies are treated as being positive

$$\begin{aligned} \left(\frac{df_{\nu_s}}{d\tau}\right)_c(\vec{q}_3) &= \frac{a}{2\varepsilon_3} \int \frac{d^3\vec{q}_1}{(2\pi)^3 2q_1} \int \frac{d^3\vec{q}_2}{(2\pi)^3 2q_2} \int \frac{d^3\vec{q}_4}{(2\pi)^3 2\varepsilon_4} |\mathcal{M}|^2 \times \\ &\times (2\pi)^4 \delta(q_1 + q_2 - \varepsilon_3 - \varepsilon_4) \delta^{(3)}(\vec{q}_1 + \vec{q}_2 - \vec{q}_3 - \vec{q}_4) \times \\ &\times \left[(1 + f_\phi(\vec{q}_1))(1 + f_\phi(\vec{q}_2))(1 - f_{\nu_s}(\vec{q}_3))(1 - f_{\nu_s}(\vec{q}_4)) - f_\phi(\vec{q}_1)f_\phi(\vec{q}_2)f_{\nu_s}(\vec{q}_3)f_{\nu_s}(\vec{q}_4) \right]. \end{aligned} \quad (\text{B9})$$

Expanding f_i as in Eq. (B1) and neglecting the Pauli-blocking and Bose-Einstein stimulated-emission factors, the background contribution and the linear-order perturbation of the collision term are respectively

$$\begin{aligned} \left(\frac{df_{\nu_s}}{d\tau}\right)_c^{(0)}(q_3) &= \frac{a}{2\varepsilon_3} \int \frac{d^3\vec{q}_1}{(2\pi)^3 2q_1} \int \frac{d^3\vec{q}_2}{(2\pi)^3 2q_2} \int \frac{d^3\vec{q}_4}{(2\pi)^3 2\varepsilon_4} |\mathcal{M}|^2 \times \\ &\times (2\pi)^4 \delta(q_1 + q_2 - \varepsilon_3 - \varepsilon_4) \delta^{(3)}(\vec{q}_1 + \vec{q}_2 - \vec{q}_3 - \vec{q}_4) \times \\ &\times \left[1 + f_\phi^0(q_1) + f_\phi^0(q_2) - f_{\nu_s}^0(q_3) - f_{\nu_s}^0(q_4) \right], \end{aligned} \quad (\text{B10})$$

and

$$\begin{aligned} \left(\frac{df_{\nu_s}}{d\tau}\right)_{c,\ell}^{(1)}(k, q_3) &\approx a \frac{i^\ell}{4\pi} \int d\Omega_{\vec{k}} P_\ell(\hat{k} \cdot \hat{q}_3) \frac{1}{2\varepsilon_3} \int \frac{d^3\vec{q}_1}{(2\pi)^3 2q_1} \int \frac{d^3\vec{q}_2}{(2\pi)^3 2q_2} \int \frac{d^3\vec{q}_4}{(2\pi)^3 2\varepsilon_4} |\mathcal{M}|^2 \times \\ &\times (2\pi)^4 \delta(q_1 + q_2 - \varepsilon_3 - \varepsilon_4) \delta^{(3)}(\vec{q}_1 + \vec{q}_2 - \vec{q}_3 - \vec{q}_4) \times \\ &\times \left[2f_\phi^0(q_1)\Psi_\phi(\vec{q}_1) - f_{\nu_s}^0(q_3)\Psi_{\nu_s}(\vec{q}_3) - f_{\nu_s}^0(q_4)\Psi_{\nu_s}(\vec{q}_4) \right], \end{aligned} \quad (\text{B11})$$

where the dependence on (\vec{k}, τ) is suppressed and the symmetry $q_1 \leftrightarrow q_2$ was used to combine two terms in the last line. Similar expressions can be derived for the ghosts ϕ . Subleading contributions were kept in Eq. (B10), arising from the terms $f_i^0 \ll 1$, that will be relevant in the collision multipoles (B7).

Integrating Eq. (B10), weighted by the sterile neutrino energy ε_3 , and neglecting subleading contributions gives the numerical fit¹⁶

$$\Gamma_\rho \equiv \frac{1}{a} \int \frac{d^3q_3}{(2\pi)^3} \varepsilon_3 \left(\frac{df_{\nu_s}}{d\tau}\right)_c^{(0)} \approx \begin{cases} 8.4 \times 10^{-6} \frac{\Lambda^9}{M_s^4} \exp\left[-6.6 \left(\frac{m_{\nu_s}}{\Lambda}\right)^{2.1}\right], & \text{scalar} \\ 9.0 \times 10^{-6} \frac{\Lambda^9}{M_v^4} \exp\left[-5.5 \left(\frac{m_{\nu_s}}{\Lambda}\right)^{4.3}\right], & \text{vector} \end{cases}, \quad (\text{B12})$$

which appears in Eq. (22). The same result arises from the integral of $\left(\frac{df_\phi}{d\tau}\right)_c^{(0)}$ weighted by the ghost energy q_1 .

The computation of the perturbed collision term in Eq. (B11) in the case of massive sterile neutrinos is nontrivial, requiring not only the integral of $\Psi_{i,\ell}$ (defined in Eq. (B5)) and solution of the multipole hierarchy (B6), but also depending on two free parameters: the Λ and am_{ν_s} . It simplifies in the relativistic limit, $q \gg am_{\nu_s}$, approximated by $m_{\nu_s} \sim 0$ in the preceding expressions. This is the most interesting case for the perturbation analysis, since then the background contributions to the energy density from ghosts and sterile neutrinos cancel and modifications of the CMB and matter power spectrum can arise only through the perturbations. We consider this scenario in detail in the following subsection, B.1, and derive an adequate approximate description for the more general case in subsection B.2.

¹⁶ See footnote 3

1. Relativistic sterile neutrinos

In the relativistic limit, it is a common simplification to integrate over \vec{q}_i in (B6), weighted by the energy and the background phase-space distribution [34]. The equations can then be expressed in terms of the relative perturbation variables: the density contrast δ_i , the divergence of the velocity field θ_i and the anisotropic stress σ_i , where $i = \phi, \nu_s$. They are defined in terms of

$$F_{i,\ell} \equiv \frac{\int dq q^3 f_i^0(q) \Psi_{i,\ell}(q)}{\int dq q^3 f_i^0(q)}, \quad (\text{B13})$$

by $\delta_i = F_{i,0}$, $\theta_i = 3kF_{i,1}/4$ and $\sigma_i = F_{i,2}/2$. Then the perturbation equations (B6) reduce to [34, 93]

$$\begin{aligned} \delta'_i &= -\frac{4}{3}\theta_i + \frac{2}{3}h' + C_0^{(1)}[F_i], \\ \theta'_i &= k^2 \left(\frac{1}{4}\delta_i - \sigma_i \right) + C_1^{(1)}[F_i], \\ F'_{i,2} &= 2\sigma'_i = \frac{8}{15}\theta_i - \frac{3}{5}kF_{i,3} + \frac{4}{15}h' + \frac{8}{5}\eta' + C_2^{(1)}[F_i], \\ F'_{i,\ell} &= \frac{k}{2\ell+1}[\ell F_{i,\ell-1} - (\ell+1)F_{i,\ell+1}] + C_\ell^{(1)}[F_i], \end{aligned} \quad (\text{B14})$$

with collision multipoles

$$C_\ell^{(1)}[F_i] \equiv \frac{\int dq q^3 \left(\frac{df_i}{d\tau} \right)_{c,\ell}^{(1)}}{\int dq q^3 f_i^0(q)} - F_{i,\ell} \frac{\int dq q^3 \left(\frac{df_i}{d\tau} \right)_c^{(0)}}{\int dq q^3 f_i^0(q)}. \quad (\text{B15})$$

The numerators can be evaluated by integrating Eqs. (B10) and (B11). In terms of $x_j \equiv q_j/\Lambda$, the collision terms for ν_s are

$$\int dq_3 q_3^3 \left(\frac{df_{\nu_s}}{d\tau} \right)_c^{(0)} = \frac{a\Lambda^5}{8(2\pi)^4} \left[\int_0^\infty dx_3 \mathcal{K}_3(x_3) + 2 \int_0^1 dx_1 f_\phi^0(x_1) \mathcal{K}_{1,0}(x_1) - \int_0^\infty dx f_{\nu_s}^0(x) (\mathcal{K}_3(x) + \mathcal{K}_{4,0}(x)) \right], \quad (\text{B16})$$

$$\int dq_3 q_3^3 \left(\frac{df_{\nu_s}}{d\tau} \right)_{c,\ell}^{(1)} = \frac{a\Lambda^5}{8(2\pi)^4} \left[2 \int_0^1 dx_1 f_{\phi,0}(x_1) \Psi_{\phi,\ell}(x_1) \mathcal{K}_{1,\ell}(x_1) - \int_0^\infty dx f_{\nu_s}^0(x) \Psi_{\nu_s,\ell}(x) (\mathcal{K}_3(x) + \mathcal{K}_{4,\ell}(x)) \right], \quad (\text{B17})$$

depending on the dimensionless kernels

$$\begin{aligned} \mathcal{K}_{1,\ell}(x_1) &= \int_0^\infty dx_3 x_3^2 \int_0^1 dx_2 \int_0^\pi d\theta_{13} P_\ell(\cos \theta_{13}) \int_0^\pi d\theta_{23} |\mathcal{M}|^2 \frac{\Theta(1 - |\cos \varphi_2|)}{|\sin \varphi_2|}, \\ \mathcal{K}_3(x_3) &= x_3^2 \int_0^1 dx_1 \int_0^1 dx_2 \int_0^\pi d\theta_{13} \int_0^\pi d\theta_{23} |\mathcal{M}|^2 \frac{\Theta(1 - |\cos \varphi_2|)}{|\sin \varphi_2|}, \\ \mathcal{K}_{4,\ell}(x_4) &= \int_0^\infty dx_3 x_3^2 \int_0^1 dx_1 \int_0^\pi d\theta_{34} P_\ell(\cos \theta_{34}) \int_0^\pi d\theta_{13} |\mathcal{M}|^2 \frac{\Theta(1 - |\cos \varphi_1|)}{|\sin \varphi_1|} \Theta(1 + x_1 - x_3 - x_4), \end{aligned} \quad (\text{B18})$$

with $\cos \varphi_2$ and $\cos \varphi_1$ given by

$$\begin{aligned} \cos \varphi_2 &= \frac{x_1 x_2 (1 - c_{13} c_{23}) - x_1 x_3 (1 - c_{13}) - x_2 x_3 (1 - c_{23})}{x_1 x_2 s_{13} s_{23}}, \\ \cos \varphi_1 &= \frac{x_1 x_3 (1 - c_{13}) + x_1 x_4 (1 - c_{13} c_{34}) - x_3 x_4 (1 - c_{34})}{x_1 x_4 s_{13} s_{34}}, \end{aligned} \quad (\text{B19})$$

and $c_{jk} = \cos \theta_{jk}$, $s_{jk} = \sin \theta_{jk}$. Analogously, the collision terms for ghosts (with overall $-$ signs from their negative energy) are

$$\int dq_1 q_1^3 \left(\frac{df_\phi}{d\tau} \right)_c^{(0)} = -\frac{a\Lambda^5}{8(2\pi)^4} \left[\int_0^1 dx_1 \mathcal{W}_1(x_1) + \int_0^1 dx f_{\phi,0}(x) (\mathcal{W}_1(x) + \mathcal{W}_{2,0}(x)) - 2 \int_0^\infty dx_3 f_{\nu_s}^0(x_3) \mathcal{W}_{3,0}(x_3) \right], \quad (\text{B20})$$

	Vector mediator							Scalar mediator						
$\mathcal{K}_{i,\ell}$	a_0	a_1	a_2	a_3	a_4	a_5	a_6	a_0	a_1	a_2	a_3	a_4	a_5	a_6
$\mathcal{K}_{1,0}$	2.2	2.8	0	0	0	0	0	6.1	-2.5	0	0	0	0	0
$\mathcal{K}_{1,1}$	-1.1	2.8	0	0	0	0	0	0.8	0.8	0	0	0	0	0
$\mathcal{K}_{1,2}$	-0.9	0.8	0	0	0	0	0	-0.3	0.9	0	0	0	0	0
$\mathcal{K}_{1,3}$	-0.1	-0.4	0	0	0	0	0	-0.3	0.5	0	0	0	0	0
$\mathcal{K}_{1,4}$	0.2	-0.5	0	0	0	0	0	-0.2	0.3	0	0	0	0	0
$\mathcal{K}_{1,5}$	0.2	-0.3	0	0	0	0	0	-0.1	0.1	0	0	0	0	0
\mathcal{K}_3	-6.1	75.8	-164.8	156.3	-75.2	18.1	-1.7	3.7	33.1	-97.1	100.9	-50.2	12.0	-1.1
$\mathcal{K}_{4,0}$	42.0	-94.5	62.7	8.4	-28.2	12.2	-1.7	80.3	-288.3	447.1	-381.1	186.8	-49.5	5.5
$\mathcal{K}_{4,1}$	-18.2	22.1	27.7	-67.4	49.2	-16.0	2.0	-25.1	78.0	-104.8	79.3	-35.9	9.2	-1.0
$\mathcal{K}_{4,2}$	-1.3	30.9	-83.0	93.1	-52.6	14.9	-1.7	-3.1	23.2	-50.7	51.6	-27.3	7.3	-0.8
$\mathcal{K}_{4,3}$	5.1	-31.2	62.9	-60.5	30.6	-7.9	0.8	2.5	-13.0	23.8	-20.7	9.3	-2.1	0.2

	Vector mediator							Scalar mediator						
$\mathcal{W}_{i,\ell}$	a_0	a_1	a_2	a_3	a_4	a_5	a_6	a_0	a_1	a_2	a_3	a_4	a_5	a_6
\mathcal{W}_1	0.1	5.5	0	0	0	0	0	4.2	0	0	0	0	0	0
$\mathcal{W}_{2,0}$	4.4	0.1	0	0	0	0	0	8.1	-5.1	0	0	0	0	0
$\mathcal{W}_{2,1}$	-2.2	0	0	0	0	0	0	-2.7	1.7	0	0	0	0	0
$\mathcal{W}_{2,2}$	0.4	0	0	0	0	0	0	0	0	0	0	0	0	0
$\mathcal{W}_{3,0}$	17.9	-11.5	-46.1	76.8	-48.5	14.1	-1.6	41.9	-127.2	173.7	-138.5	67.3	-18.4	2.2
$\mathcal{W}_{3,1}$	-12.0	45.8	-61.5	36.6	-8.4	-0.4	0.3	-10.9	56.2	-102.5	91.8	-44.0	10.9	-1.1
$\mathcal{W}_{3,2}$	-0.2	-7.7	21.5	-23.0	11.9	-3.0	0.3	-8.1	41.1	-79.2	77.4	-41.1	11.3	-1.3
$\mathcal{W}_{3,3}$	-0.8	4.3	-11.6	15.1	-9.8	3.1	-0.4	-4.9	23.7	-42.6	37.9	-17.8	4.2	-0.4
$\mathcal{W}_{3,4}$	0.8	-5.0	11.7	-14.0	9.0	-3.0	0.4	-2.1	8.0	-10.0	3.8	1.4	-1.4	0.3

TABLE III. Numerical coefficients for the polynomials in Eqs. (B24) used to fit the kernels in Eq. (B18) and (B22). Kernels with higher ℓ than those displayed are negligible. Kernels with subscripts $i = 1, 2$ refer to ghost quantities, whereas those with subscripts $i = 3, 4$ refer to sterile neutrinos. \mathcal{K}_3 and \mathcal{W}_1 do not have the ℓ subscript because they refer to the background contribution.

$$\int dq_1 q_1^3 \left(\frac{df_\phi}{d\tau} \right)_{c,\ell}^{(1)} = -\frac{a \Lambda^5}{8(2\pi)^4} \left[\int_0^1 dx f_{\phi,0}(x) \Psi_{\phi,\ell}(x) (\mathcal{W}_1(x) + \mathcal{W}_{2,\ell}(x)) - 2 \int_0^\infty dx_3 f_{\nu_s}^0(x_3) \Psi_{\nu_s,\ell}(x_3) \mathcal{W}_{3,\ell}(x_3) \right], \quad (\text{B21})$$

where

$$\begin{aligned} \mathcal{W}_1(x_1) &= x_1^2 \int_0^1 dx_2 \int_0^\infty dx_3 \int_0^\pi d\theta_{12} \int_0^\pi d\theta_{13} |\mathcal{M}|^2 \frac{\Theta(1 - |\cos \varphi_3|)}{|\sin \varphi_3|}, \\ \mathcal{W}_{2,\ell}(x_2) &= \int_0^1 dx_1 x_1^2 \int_0^\infty dx_3 \int_0^\pi d\theta_{12} P_\ell(\cos \theta_{12}) \int_0^\pi d\theta_{13} |\mathcal{M}|^2 \frac{\Theta(1 - |\cos \varphi_3|)}{|\sin \varphi_3|}, \\ \mathcal{W}_{3,\ell}(x_3) &= \int_0^1 dx_1 x_1^2 \int_0^1 dx_2 \int_0^\pi d\theta_{13} P_\ell(\cos \theta_{13}) \int_0^\pi d\theta_{12} |\mathcal{M}|^2 \frac{\Theta(1 - |\cos \varphi_3|)}{|\sin \varphi_3|}, \end{aligned} \quad (\text{B22})$$

and

$$\cos \varphi_3 = -\frac{x_1 x_2 (1 - c_{12}) - x_1 x_3 (1 - c_{13}) - x_2 x_3 (1 - c_{12} c_{13})}{x_2 x_3 s_{12} s_{13}}. \quad (\text{B23})$$

The kernels in Eqs. (B18) and (B22) are fitted by polynomials

$$(\mathcal{K}, \mathcal{W})(x) = x^3 (a_0 + a_1 x + a_2 x^2 + a_3 x^3 + a_4 x^4 + a_5 x^5 + a_6 x^6), \quad (\text{B24})$$

with coefficients a_j given in Table III for the \mathcal{K} and \mathcal{W} kernels.

The kernels associated with ghost particles (subscripts $i = 1, 2$) have only the two leading coefficients nonvanishing; therefore, the integrals over ghost momenta in Eqs. (B17) and (B21) take the form

$$\int dx x^3 f_\phi^0(x) \Psi_{\phi,\ell}(x) (\mathcal{K}, \mathcal{W})(x) \approx \int dx x^3 f_\phi^0(x) \Psi_{\phi,\ell}(x) (a_0 + a_1 x), \quad (\text{B25})$$

the first term of which is proportional to $F_{\phi,\ell}$, while the second one is a higher-order correction. To estimate the latter, we assume $\Psi_{\phi,\ell}(x)$ depends weakly on x so that

$$\begin{aligned} \int dx x^3 f_{\phi}^0(x) \Psi_{\phi,\ell}(x) (\mathcal{K}, \mathcal{W})(x) &\sim \int dx x^3 f_{\phi}^0(x) \Psi_{\phi,\ell}(x) \left[a_0 + a_1 \frac{\int dx x^4 f_{\phi}^0(x)}{\int dx x^3 f_{\phi}^0(x)} \right] \\ &\sim F_{\phi,\ell} \frac{\rho_{\phi}}{\Lambda^4} \begin{cases} [a_0 + 0.66 a_1], & \text{scalar} \\ [a_0 + 0.69 a_1], & \text{vector} \end{cases}, \end{aligned} \quad (\text{B26})$$

using $f_{\phi}^0(x)$ defined in Eq. (14); see Fig. 3. The factor $1/\Lambda^4$ comes from the normalization of the background phase-space distribution according to the number density, so that $f_i^0(x) \propto \Gamma_{\rho}/(\Lambda^4 H_0)$, while $\rho_i(a) \propto \Gamma_{\rho}/H_0$ as in Eq. (31). For ν_s , the analogous procedure leads to

$$\begin{aligned} \int dx f_{\nu_s}^0(x) \Psi_{\nu_s,\ell}(x) (\mathcal{K}, \mathcal{W}) &\approx \int dx x^3 f_{\nu_s}^0(x) \Psi_{\nu_s,\ell}(x) (a_0 + a_1 x + a_2 x^2 + a_3 x^3 + a_4 x^4 + a_5 x^5 + a_6 x^6) \\ &\sim \int dx x^3 f_{\nu_s}^0(x) \Psi_{\nu_s,\ell}(x) \left[a_0 + a_1 \frac{\int dx x^4 f_{\nu_s}^0(x)}{\int dx x^3 f_{\nu_s}^0(x)} + a_2 \frac{\int dx x^5 f_{\nu_s}^0(x)}{\int dx x^3 f_{\nu_s}^0(x)} + \right. \\ &\quad + a_3 \frac{\int dx x^6 f_{\nu_s}^0(x)}{\int dx x^3 f_{\nu_s}^0(x)} + a_4 \frac{\int dx x^7 f_{\nu_s}^0(x)}{\int dx x^3 f_{\nu_s}^0(x)} + \\ &\quad \left. + a_5 \frac{\int dx x^8 f_{\nu_s}^0(x)}{\int dx x^3 f_{\nu_s}^0(x)} + a_6 \frac{\int dx x^9 f_{\nu_s}^0(x)}{\int dx x^3 f_{\nu_s}^0(x)} \right] \\ &\sim F_{\nu_s,\ell} \frac{\rho_{\nu_s}}{\Lambda^4} \begin{cases} [a_0 + 0.72 a_1 + 0.59 a_2 + 0.54 a_3 + 0.53 a_4 + 0.56 a_5 + 0.63 a_6], & \text{scalar} \\ [a_0 + 0.75 a_1 + 0.63 a_2 + 0.58 a_3 + 0.58 a_4 + 0.61 a_5 + 0.68 a_6], & \text{vector} \end{cases}. \end{aligned} \quad (\text{B27})$$

The series $[a_0 + \dots]$ in Eqs. (B26,B27) differ from each other because of the larger phase space available for ν_s relative to ϕ .

Equations (B16) and (B20) can be similarly estimated, but more simply since all the functions are now known. Therefore, Eqs. (B16), (B17), (B20) and (B21) reduce to

$$\begin{aligned} \int dq_3 q_3^3 \left(\frac{df_{\nu_s}}{d\tau} \right)_c^{(0)} &\approx a\Gamma_{\rho} + a \frac{\Gamma_{\rho}}{\Lambda^4} \left[a_{\nu_s,0} \rho_{\phi} + b_{\nu_s,0} \rho_{\nu_s} \right], \\ \int dq_1 q_1^3 \left(\frac{df_{\phi}}{d\tau} \right)_c^{(0)} &\approx -a\Gamma_{\rho} + a \frac{\Gamma_{\rho}}{\Lambda^4} \left[a_{\phi,0} \rho_{\phi} + b_{\phi,0} \rho_{\nu_s} \right], \\ \int dq_{\nu_s} q_{\nu_s}^3 \left(\frac{df_{\nu_s}}{d\tau} \right)_{c,\ell}^{(1)} &\approx a \frac{\Gamma_{\rho}}{\Lambda^4} \left[a_{\nu_s,\ell} \rho_{\phi} F_{\phi,\ell} + b_{\nu_s,\ell} \rho_{\nu_s} F_{\nu_s,\ell} \right], \\ \int dq_{\phi} q_{\phi}^3 \left(\frac{df_{\phi}}{d\tau} \right)_{c,\ell}^{(1)} &\approx a \frac{\Gamma_{\rho}}{\Lambda^4} \left[a_{\phi,\ell} \rho_{\phi} F_{\phi,\ell} + b_{\phi,\ell} \rho_{\nu_s} F_{\nu_s,\ell} \right], \end{aligned} \quad (\text{B28})$$

where $a_{i,\ell}$ and $b_{i,\ell}$ are given in Table IV. There one notices that the $\ell = 0, 1$ terms of Eq. (B28) for ν_s are equal and opposite in sign to those for ϕ , as well as the background terms. This follows from energy and momentum conservation both at the zeroth and linear order in the perturbations [93]. Moreover, the second term in the first two equations in (B28) is subleading compared to Γ_{ρ} , scaling as $\Gamma_{\rho}^2/(H_0 \Lambda^4)$. Although it can be neglected in the background Boltzmann equations, it is needed in the perturbation equations since it is of the same order as the perturbed collision term (see Eqs. (B15) and (B28)).

	Vector mediator				Scalar mediator			
	ν_s		ϕ		ν_s		ϕ	
ℓ	$a_{\nu_s,\ell}$	$b_{\nu_s,\ell}$	$a_{\phi,\ell}$	$b_{\phi,\ell}$	$a_{\nu_s,\ell}$	$b_{\nu_s,\ell}$	$a_{\phi,\ell}$	$b_{\phi,\ell}$
0	7.5	-8.1	-7.5	8.1	8.1	-9.7	-8.1	9.7
1	1.5	0.2	-1.5	-0.2	2.3	-0.8	-2.3	0.8
2	-0.7	-43.3	-3.9	32.0	0.5	-79.3	-3.8	90.7
3	-0.6	-2.6	-3.5	-0.3	-0.1	-3.4	-3.8	-0.1
4	-0.3	-3.0	-3.5	-0.1	0	-3.4	-3.8	0
5	-0.1	-2.9	-3.5	0	0	-3.4	-3.8	0
≥ 6	0	-2.9	-3.5	0	0	-3.4	-3.8	0

TABLE IV. Numerical value of the coefficients $a_{i,\ell}$ and $b_{i,\ell}$ entering Eq. (B28).

Substituting Eq. (B28) into Eq. (B15), the full perturbation equations (B14) for ν_s are

$$\begin{aligned}
\delta'_{\nu_s} &\approx -\frac{4}{3}\theta_{\nu_s} - \frac{2}{3}h' + a \frac{\Gamma_\rho}{\Lambda^4} \left[a_{\nu_s,0} \frac{\rho_\phi}{\rho_{\nu_s}} (\delta_\phi - \delta_{\nu_s}) \right] - a \frac{\Gamma_\rho}{\rho_{\nu_s}} \delta_{\nu_s}, \\
\theta'_{\nu_s} &\approx k^2 \left(\frac{1}{4} \delta_{\nu_s} - \sigma_{\nu_s} \right) + a \frac{\Gamma_\rho}{\Lambda^4} \left[a_{\nu_s,1} \frac{\rho_\phi}{\rho_{\nu_s}} \theta_\phi + \left(B_{\nu_s,1} - a_{\nu_s,0} \frac{\rho_\phi}{\rho_{\nu_s}} \right) \theta_{\nu_s} \right] - a \frac{\Gamma_\rho}{\rho_{\nu_s}} \theta_{\nu_s}, \\
F'_{\nu_s,2} = 2\sigma'_{\nu_s} &\approx \frac{8}{15} \theta_{\nu_s} - \frac{3}{5} k F_{\nu_s,3} + \frac{4}{15} h' + \frac{8}{5} \eta' + 2a \frac{\Gamma_\rho}{\Lambda^4} \left[a_{\nu_s,2} \frac{\rho_\phi}{\rho_{\nu_s}} \sigma_\phi + \left(B_{\nu_s,2} - a_{\nu_s,0} \frac{\rho_\phi}{\rho_{\nu_s}} \right) \sigma_{\nu_s} \right] - 2a \frac{\Gamma_\rho}{\rho_{\nu_s}} \sigma_{\nu_s}, \\
F'_{\nu_s,\ell \geq 2} &\approx \frac{k}{2\ell+1} [\ell F_{\nu_s,\ell-1} - (\ell+1) F_{\nu_s,\ell+1}] + a \frac{\Gamma_\rho}{\Lambda^4} \left[\left(B_{\nu_s,\ell} - a_{\nu_s,0} \frac{\rho_\phi}{\rho_{\nu_s}} \right) F_{\nu_s,\ell} \right] - a \frac{\Gamma_\rho}{\rho_{\nu_s}} F_{\nu_s,\ell},
\end{aligned} \tag{B29}$$

where $B_{\nu_s,\ell} \equiv (b_{\nu_s,\ell} - b_{\nu_s,0})$, and for the ghosts they are

$$\begin{aligned}
\delta'_\phi &\approx -\frac{4}{3}\theta_\phi - \frac{2}{3}h' + a \frac{\Gamma_\rho}{\Lambda^4} \left[-b_{\phi,0} \frac{\rho_{\nu_s}}{\rho_\phi} (\delta_\phi - \delta_{\nu_s}) \right] + a \frac{\Gamma_\rho}{\rho_\phi} \delta_\phi, \\
\theta'_\phi &\approx k^2 \left(\frac{1}{4} \delta_\phi - \sigma_\phi \right) + a \frac{\Gamma_\rho}{\Lambda^4} \left[\left(A_{\phi,1} - b_{\phi,0} \frac{\rho_{\nu_s}}{\rho_\phi} \right) \theta_\phi + b_{\phi,1} \frac{\rho_{\nu_s}}{\rho_\phi} \theta_{\nu_s} \right] + a \frac{\Gamma_\rho}{\rho_\phi} \theta_\phi, \\
F'_{\phi,2} = 2\sigma'_\phi &\approx \frac{8}{15} \theta_\phi - \frac{3}{5} k F_{\phi,3} + \frac{4}{15} h' + \frac{8}{5} \eta' + 2a \frac{\Gamma_\rho}{\Lambda^4} \left[\left(A_{\phi,2} - b_{\phi,0} \frac{\rho_{\nu_s}}{\rho_\phi} \right) \sigma_\phi + b_{\phi,2} \frac{\rho_{\nu_s}}{\rho_\phi} \sigma_{\nu_s} \right] + 2a \frac{\Gamma_\rho}{\rho_\phi} \sigma_\phi, \\
F'_{\phi,\ell \geq 2} &\approx \frac{k}{2\ell+1} [\ell F_{\phi,\ell-1} - (\ell+1) F_{\phi,\ell+1}] + a \frac{\Gamma_\rho}{\Lambda^4} \left[\left(A_{\phi,\ell} - b_{\phi,0} \frac{\rho_{\nu_s}}{\rho_\phi} \right) F_{\phi,\ell} \right] + a \frac{\Gamma_\rho}{\rho_\phi} F_{\phi,\ell},
\end{aligned} \tag{B30}$$

where $A_{\phi,\ell} \equiv (a_{\phi,\ell} - a_{\phi,0})$. For both species, we solved the perturbation equations with CAMB up to the hierarchy multipole $\ell_{\max} = 45$, as done for massless neutrinos and photons when no approximation scheme is applied.

a. Qualitative features of the perturbed massless equations

Eqs. (B29) and (B30) can be further simplified since $\rho_{\nu_s}(a) = -\rho_\phi(a)$ for massless sterile neutrinos. Then the last term on the right-hand sides, which arise from the time dependence of the background phase-space distributions f_i^0 , are negative assuming $F_{i,\ell} > 0$ and therefore provide damping of the perturbations for all values of ℓ . Such damping is typical of particle decay processes (*e.g.*, Ref. [94]), hence we will refer to it as the ‘‘decay term’’ below. Its effect is larger at early times because $\rho_i(a)$ evolves faster than a . The damping is independent of Γ_ρ since $\rho_i \propto \Gamma_\rho/H_0$, according to Eq. (31).

On the other hand, the second-to-last term of the right-hand sides of Eqs. (B29) and (B30), which we will refer to as the ‘‘collision term,’’ scales as a , so that it grows at late times. Being proportional to $\Gamma_\rho/\Lambda^4 \sim \Lambda(\Lambda/M_i)^4$, it is generally smaller than the last term. We expect that deviations in the CMB or matter power spectra with respect to Λ CDM will be apparent only when the collision term starts to dominate over the decay term, otherwise Eqs. (B29) and (B30) become identical, giving $F_{\nu_s,\ell} \sim F_{\phi,\ell}$, implying $\rho_{\nu_s} F_{\nu_s,\ell} + \rho_\phi F_{\phi,\ell} \sim 0$. However, the collision term in the high- ℓ equations leads to exponential instabilities because of the positive sign in front of the relative perturbation

$F_{i,\ell}$.¹⁷ Hence, it cannot be too much larger than the decay term while remaining consistent with the CMB and matter power spectrum. This criterion gives the estimate $\Gamma_\rho/\Lambda^4 \lesssim H_0 \sim 10^{-39}$ MeV, in rough agreement with the quantitative result of Section IV.

This reasoning also explains why Γ_ρ becomes unconstrained at sufficiently small values of Γ_ρ/Λ^4 (see Fig. 10). In that regime the collision term is small compared to the decay term, and the perturbations become irrelevant. Moreover, deviations between $\Lambda\text{CDM}\phi\nu_s$ and ΛCDM are more pronounced at small k (large scales), because the Liouville term (the first term) of the perturbation equations above becomes negligible, being proportional to k . This is borne out in Fig. 8.

It is noteworthy that $F_{\nu_s,\ell}$ is less suppressed than $F_{\phi,\ell}$, at $\ell > 2$, where the ϕ and ν_s equations decouple. This is because $(a_{\phi,\ell} - a_{\phi,0}) + b_{\phi,0} < (b_{\nu_s,\ell} - b_{\nu_s,0}) + a_{\nu_s,0}$ in the comparison of their collision terms; hence $F_{\nu_s,\ell} \gtrsim F_{\phi,\ell}$ for $\ell \gtrsim 2$.¹⁸ The physical origin for this can be traced to the larger phase space available for sterile neutrinos than for ghosts, which increases its collision term. For the $\ell = 0, 1$ perturbations, the situation is more complicated since the ν_s and ϕ equations are coupled.

The perturbations for the scalar mediator have a modestly larger effect on cosmological observables relative to the vector mediator. This is ultimately due to the kinematical dependences of the matrix elements (9), which result in the coefficients for the scalar model in Table IV being larger than the vector ones. This trend is confirmed by the CosmoMC results in Fig. 10.

2. Massive sterile neutrinos

A detailed analysis of the cosmological perturbations for the most general case where ν_s can be nonrelativistic, is beyond the scope of the present paper, since in that case the perturbations play a subdominant role compared to the background contributions to the energy density. Nevertheless, we develop an approximate treatment in this appendix.

The perturbation equation hierarchy for massive ν_s is given in Eq. (B6), from which the perturbed energy density, pressure, energy flux and shear stress in k -space are [34]

$$\begin{aligned}\delta\rho_{\nu_s} &= \frac{1}{a^4} \int dq q^2 \varepsilon f_{\nu_s,0}(q) \Psi_{\nu_s,0}, \\ \delta P_{\nu_s} &= \frac{1}{3a^4} \int dq q^2 \frac{q^2}{\varepsilon} f_{\nu_s,0}(q) \Psi_{\nu_s,0}, \\ (\rho_{\nu_s} + P_{\nu_s})\theta_{\nu_s} &= \frac{k}{a^4} \int dq q^3 f_{\nu_s,0}(q) \Psi_{\nu_s,1}, \\ (\rho_{\nu_s} + P_{\nu_s})\sigma_{\nu_s} &= \frac{2}{3a^4} \int dq q^2 \frac{q^2}{\varepsilon} f_{\nu_s,0}(q) \Psi_{\nu_s,2},\end{aligned}\tag{B31}$$

where $\varepsilon = \sqrt{q^2 + a^2 m_{\nu_s}^2}$ is the comoving energy of ν_s . Proceeding analogously to the massless case, one can integrate Eq. (B6) over q , weighting by ε or q^2/ε , to obtain Eq. (B31).

We take as an example the $\ell = 0$ equation, giving the density contrast δ_{ν_s} , since the same procedure can be straightforwardly applied to higher multipoles. From Eq. (B31), one obtains

$$\begin{aligned}\int dq q^2 \varepsilon f_{\nu_s,0}(q) \Psi'_{\nu_s,0} &= -k \int dq q^3 f_{\nu_s,0}(q) \Psi_{\nu_s,1} + \frac{h'}{6} \int dq q^3 \varepsilon \frac{df_{\nu_s,0}}{dq} + \int dq q^2 \varepsilon f_{\nu_s,0}(q) \mathcal{C}_0^{(1)}[\Psi_{\nu_s,0}] \\ &= -\frac{a^4}{4\pi} (\rho_{\nu_s} + P_{\nu_s}) \theta_i - \frac{h'}{2} \frac{a^4}{4\pi} (\rho_{\nu_s} + P_{\nu_s}) + \int dq q^2 \varepsilon \left[\left(\frac{df_{\nu_s}}{d\tau} \right)_{C,0}^{(1)} - \left(\frac{df_{\nu_s}}{d\tau} \right)_C^{(0)} \Psi_{\nu_s,0} \right] \\ &= -\frac{a^4 \rho_{\nu_s}}{4\pi} (1 + w_{\nu_s}) \left(\theta_{\nu_s} + \frac{h'}{2} \right) + \int dq q^2 \varepsilon \left(\frac{df_{\nu_s}}{d\tau} \right)_{C,0}^{(1)} - \int dq q^2 \varepsilon \left(\frac{df_{\nu_s}}{d\tau} \right)_C^{(0)} \Psi_{\nu_s,0},\end{aligned}\tag{B32}$$

in the second step using the definition of $\mathcal{C}_0^{(1)}[\Psi_{\nu_s,0}]$ in Eq. (B7), integrating the second integral on the right-hand side by parts, and using the definitions of the background density and pressure given by Eq. (21) expressed in comoving

¹⁷ The sign follows from the numerical values of the coefficients in Table IV.

¹⁸ Since the relative perturbation $F_{i,\ell}$ for $\ell \gtrsim 2$ is negative for relativistic particles, such as massless SM neutrinos and photons,

the condition $F_{\nu_s,\ell} \gtrsim F_{\phi,\ell}$ implies that $F_{\phi,\ell}$ is more negative than $F_{\nu_s,\ell}$. Therefore $0 \lesssim |\rho_{\nu_s} F_{\nu_s,\ell}| \lesssim \rho_\phi F_{\phi,\ell}$ for the physical perturbations, since $\rho_{\nu_s} = -\rho_\phi \gtrsim 0$. This is confirmed by Fig. 9 (left).

variables. The left-hand side of Eq. (B32) can be related to the time derivative of the density contrast δ_{ν_s} via

$$\begin{aligned}\delta'_{\nu_s} &= \frac{\delta\rho'_{\nu_s}}{\rho_{\nu_s}} - \frac{\rho'_{\nu_s}}{\rho_{\nu_s}}\delta_{\nu_s} = \frac{\int dq q^2 (\varepsilon f_{\nu_s,0}(q)\Psi_{\nu_s,0})'}{\int dq q^2 \varepsilon f_{\nu_s,0}(q)} - \frac{\int dq q^2 (\varepsilon f_{\nu_s,0}(q))'}{\int dq q^2 \varepsilon f_{\nu_s,0}(q)} \\ &= \frac{4\pi}{a^4 \rho_{\nu_s}} a^2 m_{\nu_s}^2 \mathcal{H} \int dq \frac{q^2}{\varepsilon} f_{\nu_s,0}(q) \Psi_{\nu_s,0} + \frac{4\pi}{a^4 \rho_{\nu_s}} \int dq q^2 \varepsilon \left(\frac{df_{\nu_s,0}}{d\tau} \right)'_C \Psi_{\nu_s,0} + \frac{4\pi}{a^4 \rho_{\nu_s}} \int dq q^2 \varepsilon f_{\nu_s,0}(q_i) \Psi'_{\nu_s,0} \\ &\quad - \frac{4\pi}{a^4 \rho_{\nu_s}} \delta_{\nu_s} \left[a^2 m_{\nu_s}^2 \mathcal{H} \int dq \frac{q^2}{\varepsilon} f_{\nu_s,0}(q) + \int dq q^2 \varepsilon \left(\frac{df_{\nu_s,0}}{d\tau} \right)'_C \right],\end{aligned}\quad (\text{B33})$$

where we used the background Boltzmann equation (B3) and $\varepsilon'_{\nu_s} = a^2 m_{\nu_s}^2 \mathcal{H} / \varepsilon_{\nu_s}$, with $\mathcal{H} = d \ln a / d\tau = aH$, the comoving Hubble rate. Combining Eq. (B33) with (B32),

$$\delta'_{\nu_s} = -(1 + w_{\nu_s}) \left(\theta_{\nu_s} + \frac{h'}{2} \right) + \frac{4\pi}{a^4 \rho_{\nu_s}} \mathcal{H} a^2 m_{\nu_s}^2 \left[\int dq \frac{q^2}{\varepsilon} f_{\nu_s,0}(q) \Psi_{\nu_s,0} - \delta_{\nu_s} \int dq \frac{q^2}{\varepsilon} f_{\nu_s,0}(q) \right] + \mathcal{C}_0^{(1)}[\delta_{\nu_s}], \quad (\text{B34})$$

by defining a new collision term

$$\mathcal{C}_0^{(1)}[\delta_{\nu_s}] \equiv \frac{\int dq q^2 \varepsilon \left(\frac{df_{\nu_s}}{d\tau} \right)'_{C,0}}{\int dq q^2 \varepsilon f_{\nu_s,0}(q)} - \delta_{\nu_s} \frac{\int dq q^2 \varepsilon \left(\frac{df_{\nu_s}}{d\tau} \right)'_C}{\int dq q^2 \varepsilon f_{\nu_s,0}(q)}, \quad (\text{B35})$$

in analogy with Eq. (B15) for the massless sterile neutrino case. Notice that Eq. (B34) reduces to the first equation of (B14) in the massless case, $m_{\nu_s} \rightarrow 0$ and $w_{\nu_s} \rightarrow 1/3$.

Although Eq. (B35) is exact, it can be simplified in the nonrelativistic limit, for which $q \ll am_{\nu_s}$. The terms in the square parenthesis reduce to

$$\begin{aligned}\mathcal{H} \frac{a^2 m_{\nu_s}^2}{\rho_{\nu_s}} \left[\int dq \frac{q^2}{\varepsilon} f_{\nu_s,0}(q) \Psi_{\nu_s,0} - \delta_{\nu_s} \int dq \frac{q^2}{\varepsilon} f_{\nu_s,0}(q) \right] &\simeq \frac{\mathcal{H}}{\rho_{\nu_s}} \int dq am_{\nu_s} q^2 \left(1 - \frac{1}{2} \frac{q^2}{a^2 m_{\nu_s}^2} + \mathcal{O}\left(\frac{q^4}{a^4 m_{\nu_s}^4}\right) \right) f_{\nu_s,0}(q) \Psi_{\nu_s,0} \\ &\quad - \mathcal{H} \frac{\delta_{\nu_s}}{\rho_{\nu_s}} \int dq am_{\nu_s} q^2 \left(1 - \frac{1}{2} \frac{q^2}{a^2 m_{\nu_s}^2} + \mathcal{O}\left(\frac{q^4}{a^4 m_{\nu_s}^4}\right) \right) f_{\nu_s,0}(q) \\ &\simeq \mathcal{H} \left(\frac{\delta\rho_{\nu_s}}{\rho_{\nu_s}} - 3 \frac{\delta P_{\nu_s}}{\rho_{\nu_s}} \right) - \mathcal{H} \left(1 - 3 \frac{P_{\nu_s}}{\rho_{\nu_s}} \right) \delta_{\nu_s} \\ &\simeq -3\mathcal{H} (c_{s,\nu_s}^2 - w_{\nu_s}) \delta_{\nu_s},\end{aligned}\quad (\text{B36})$$

by introducing the fluid sound speed $c_{s,\nu_s}^2 \equiv \delta P_{\nu_s} / \delta \rho_{\nu_s}$ and using $\varepsilon \simeq am_{\nu_s} [1 + q^2 / (2a^2 m_{\nu_s}^2) + \mathcal{O}(q^4 / (a^4 m_{\nu_s}^4))]$. For a barotropic fluid, applicable since the equation of state for the new species is constant in time, $c_{s,\nu_s}^2 \simeq w_{\nu_s} \approx \text{constant}$ and therefore Eq. (B36) vanishes. Since it is negligible both in the relativistic and nonrelativistic limits, we neglect it for general m_{ν_s} . Then Eq. (B34) simplifies to

$$\delta'_{\nu_s} \simeq -(1 + w_{\nu_s}) \left(\theta_{\nu_s} + \frac{h'}{2} \right) + \mathcal{C}_0^{(1)}[\delta_{\nu_s}], \quad (\text{B37})$$

which agrees with the derivation based on energy-momentum conservation [34].

The new collision term given by Eq. (B35) is complicated in the general $m_{\nu_s} > 0$ case. However, based on the results we obtained for $m_{\nu_s} = 0$, some inferences can be made. In particular, the first term of Eq. (B35) is proportional to Γ_ρ / Λ^4 , since it depends linearly on the background phase-space distribution $f_i^0(q)$ with $i = \phi, \nu_s$, whereas the second term is exactly given by $\Gamma_\rho \delta_{\nu_s} / \rho_{\nu_s}$ and is thus proportional to H_0 . In order to be consistent with type Ia supernovae data, Fig. 7 implies that $\Gamma_\rho \lesssim \mathcal{O}(10^{-70}) \text{ MeV}^5$. For such small values, the constraints on Γ_ρ and Γ_ρ / Λ^4 for $m_{\nu_s} = 0$, Fig. 10, become almost independent of Γ_ρ / Λ^4 , suggesting that the first term of Eq. (B35) is negligible compared to the second. Physically, this means that redshifting of the new species, described by the Liouville terms and the second part of the collision term, is more important than the growth from particle production, when $m_{\nu_s} > 0$. In this case the perturbations of the new species decouple from each other.

By neglecting the first piece of the new collision term in Eq. (B35), we expect to find conservative bounds for the parameter Γ_ρ , or quantities derived from it such as Ω_g , that might be moderately strengthened by a more exact treatment. The bounds derived for $m_{\nu_s} > 0$ come primarily from the background contributions of the new species, rather their perturbations.

Carrying out the same procedure as for δ_{ν_s} to higher ℓ , the perturbation equations for ϕ and ν_s are

$$\begin{aligned}
\delta'_{\nu_s} &\sim -(1 + w_{\nu_s}) \left(\theta_{\nu_s} + \frac{h'}{2} \right) - a \frac{\Gamma_\rho}{\rho_{\nu_s}} \delta_{\nu_s}, \\
\theta'_{\nu_s} &\sim -\mathcal{H}(1 - 3w_{\nu_s}) \theta_{\nu_s} + \frac{w_{\nu_s}}{1 + w_{\nu_s}} k^2 \delta_{\nu_s} - k^2 \sigma_{\nu_s} - a \frac{\Gamma_\rho}{\rho_{\nu_s}} \theta_{\nu_s}, \\
\sigma'_{\nu_s} &\sim -3\mathcal{H}\sigma_{\nu_s} + \frac{8}{3} \frac{w_{\nu_s}}{1 + w_{\nu_s}} \left(\theta_{\nu_s} + \frac{h'}{2} + 3\eta' \right) - a \frac{\Gamma_\rho}{\rho_{\nu_s}} \sigma_{\nu_s}, \\
\delta'_\phi &\sim -\frac{4}{3} \theta_\phi + \frac{2}{3} h' + a \frac{\Gamma_\rho}{\rho_\phi} \delta_\phi, \\
\theta'_\phi &\sim k^2 \left(\frac{1}{4} \delta_\phi - \sigma_\phi \right) + a \frac{\Gamma_\rho}{\rho_\phi} \theta_\phi, \\
\sigma'_\phi &\sim -3\mathcal{H}\sigma_\phi + \frac{2}{3} \left(\theta_\phi + \frac{h'}{2} + 3\eta' \right) + a \frac{\Gamma_\rho}{\rho_\phi} \sigma_\phi,
\end{aligned} \tag{B38}$$

assuming a barotropic fluid, where we neglected the equations for the multipoles with $\ell > 2$ since they will become negligible for nonrelativistic ν_s . Similar equations for the anisotropic stress σ_i were derived in Refs. [32, 39, 95] to approximate the closing of the ℓ hierarchy at the quadrupole, valid for both massless and massive particles. We take the viscosity parameter in Ref. [95] to be $c_{i,\text{vis}}^2 \simeq w_i$. These equations encapsulate the free-streaming effect of the new species, which cannot be neglected; Ref. [95] showed that doing so in the SM with massless neutrinos induces an error of $\sim 10\%$ in the CMB power spectrum. Different prescriptions for the shear stress equation can be found in Ref. [96], which provide similar numerical accuracy.

The perturbation equations derived above become the same for ϕ and ν_s in the limit $w_{\nu_s} \rightarrow 1/3$, since the part of the collision term sensitive to their phase space differences has been neglected. Hence the physical perturbations of the new species cancel each other in that limit, $(\rho_{\nu_s} \delta_{\nu_s} + \rho_\phi \delta_\phi) \rightarrow 0$. Similarly to the $m_{\nu_s} = 0$ treatment, the equations are solved within CAMB up to the $\ell_{\text{max}} = 45$.

Appendix C: Correlations between parameters

In this appendix, we present the full correlation plots including all parameters in the $\Lambda\text{CDM}\phi\nu_s$ model, as inferred from CosmoMC.

1. Massless ν_s case

For $m_{\nu_s} = 0$, the input parameters are the standard six of ΛCDM , plus Γ_ρ , which controls the amplitude of ϕ and ν_s energy densities, and Γ_ρ/Λ^4 , which sets the strength of the perturbed collision term in the linear perturbations. Table V shows the best-fit values for these parameters and their associated 68% C.L. intervals. We verified consistency with the Planck 2018 best-fit parameters [24], which is expected since for $m_{\nu_s} = 0$ the homogeneous components of the Universe remain the same as in ΛCDM .

The new parameters, Γ_ρ and Γ_ρ/Λ^4 , are degenerate with several ΛCDM parameters, as shown in Fig. 19. This occurs because the linear-order ϕ and ν_s perturbations affect the CMB and matter power spectra through their energy densities, whose magnitude is of order $\Gamma_\rho/(H_0 \sqrt{\Omega_\Lambda})$, from Eq. (31), with $\Omega_\Lambda \approx 1 - \Omega_m$.

The choice of the vector versus scalar mediator has a small impact on the results of Table V and Fig. 19, and only the correlation between Γ_ρ and Γ_ρ/Λ differs slightly between the two cases. This can be traced back to the numerical coefficients in the perturbation equations (B29) and (B30); see Table IV.

2. Massive ν_s case

For massive ν_s , the new-physics parameters are taken to be Ω_g and w_{ν_s} . They show degeneracies with several ΛCDM quantities in Fig. 20. As noted previously, w_{ν_s} is largely completely unconstrained, having no effect on most of the ΛCDM parameters. The exceptions are σ_8 and S_8 , which are related to the amplitude of the matter perturbations. This occurs because w_{ν_s} impacts the linear perturbation equations. Table VI shows the 68% C.L. parameter intervals for the $\Lambda\text{CDM}\phi\nu_s$ model for the massive ν_s scenario, as derived from CosmoMC.

Massless ν_s		
Parameter	vector	scalar
$\Omega_b h^2$	0.02235 ± 0.00015	0.02235 ± 0.00015
$\Omega_c h^2$	0.1202 ± 0.0012	0.1202 ± 0.0012
$100 \theta_{\text{MC}}$	1.04089 ± 0.00031	1.04090 ± 0.00031
τ	0.0549 ± 0.0075	0.0550 ± 0.0075
$\ln(10^{10} A_s)$	3.046 ± 0.015	3.046 ± 0.015
n_s	0.9642 ± 0.0042	0.9643 ± 0.0042
$\log_{10}(\Gamma_\rho/\text{MeV}^5)$	—	—
$\log_{10}(\Gamma_\rho/\Lambda^4/\text{MeV})$	< -58.1	< -58.4
$H_0/[\text{km/s/Mpc}]$	67.25 ± 0.54	67.26 ± 0.55
Ω_Λ	0.6832 ± 0.0075	0.6834 ± 0.0075
Ω_m	0.3168 ± 0.0075	0.3166 ± 0.0075
σ_8	0.8122 ± 0.0061	0.8123 ± 0.0061
S_8	0.835 ± 0.013	0.834 ± 0.013

TABLE V. 68% C.L. parameter intervals for the $\Lambda\text{CDM}\phi\nu_s$ model, as inferred from CosmoMC in the massless ν_s scenario, for the vector and scalar mediators. The first six parameters in bold are for the ΛCDM model, whereas the following two are associated to the new physics. The remaining ones are derived from the cosmological model.

Massive ν_s	
Parameter	both mediators
$\Omega_b h^2$	0.02246 ± 0.00014
$\Omega_c h^2$	0.11878 ± 0.00094
$100 \theta_{\text{MC}}$	1.04102 ± 0.00029
τ	0.0556 ± 0.0074
$\ln(10^{10} A_s)$	3.045 ± 0.014
n_s	0.9670 ± 0.0037
Ω_g	< 0.102
w_{ν_s}	—
$H_0/[\text{km/s/Mpc}]$	$68.88^{+0.48}_{-0.75}$
Ω_Λ	$0.617^{+0.069}_{-0.027}$
Ω_m	$0.2992^{+0.0068}_{-0.0056}$
σ_8	$0.801^{+0.027}_{-0.081}$
S_8	$0.799^{+0.027}_{-0.077}$

TABLE VI. Similar to Table V, but for the massive ν_s scenario. The results are independent of the mediator model chosen.

-
- [1] S. Hannestad and E. Mortsell, “Probing the dark side: Constraints on the dark energy equation of state from CMB, large scale structure and Type Ia supernovae,” *Phys. Rev. D* **66** (2002) 063508, [arXiv:astro-ph/0205096](#).
- [2] A. Melchiorri, L. Mersini-Houghton, C. J. Odman, and M. Trodden, “The State of the dark energy equation of state,” *Phys. Rev. D* **68** (2003) 043509, [arXiv:astro-ph/0211522](#).
- [3] J. A. S. Lima, J. V. Cunha, and J. S. Alcaniz, “Constraining the dark energy with galaxy clusters x-ray data,” *Phys. Rev. D* **68** (2003) 023510, [arXiv:astro-ph/0303388](#).
- [4] K. Bamba, S. Capozziello, S. Nojiri, and S. D. Odintsov, “Dark energy cosmology: the equivalent description via different theoretical models and cosmography tests,” *Astrophys. Space Sci.* **342** (2012) 155–228, [arXiv:1205.3421 \[gr-qc\]](#).
- [5] S. M. Carroll, M. Hoffman, and M. Trodden, “Can the dark energy equation-of-state parameter w be less than -1 ?,” *Phys. Rev. D* **68** (2003) 023509, [arXiv:astro-ph/0301273](#).
- [6] J. M. Cline, S. Jeon, and G. D. Moore, “The Phantom menaced: Constraints on low-energy effective ghosts,” *Phys. Rev. D* **70** (2004) 043543, [arXiv:hep-ph/0311312](#).
- [7] B. Holdom, “Accelerated expansion and the Goldstone ghost,” *JHEP* **07** (2004) 063, [arXiv:hep-th/0404109](#).
- [8] V. A. Rubakov, “Phantom without UV pathology,” *Theor. Math. Phys.* **149** (2006) 1651–1664, [arXiv:hep-th/0604153](#).
- [9] M. Libanov, V. Rubakov, E. Papantonopoulos, M. Sami, and S. Tsujikawa, “UV stable, Lorentz-violating dark energy with transient phantom era,” *JCAP* **08** (2007) 010, [arXiv:0704.1848 \[hep-th\]](#).
- [10] B. R. Holstein, “Analytical On-shell Calculation of Higher Order Scattering: Massive Particles,”

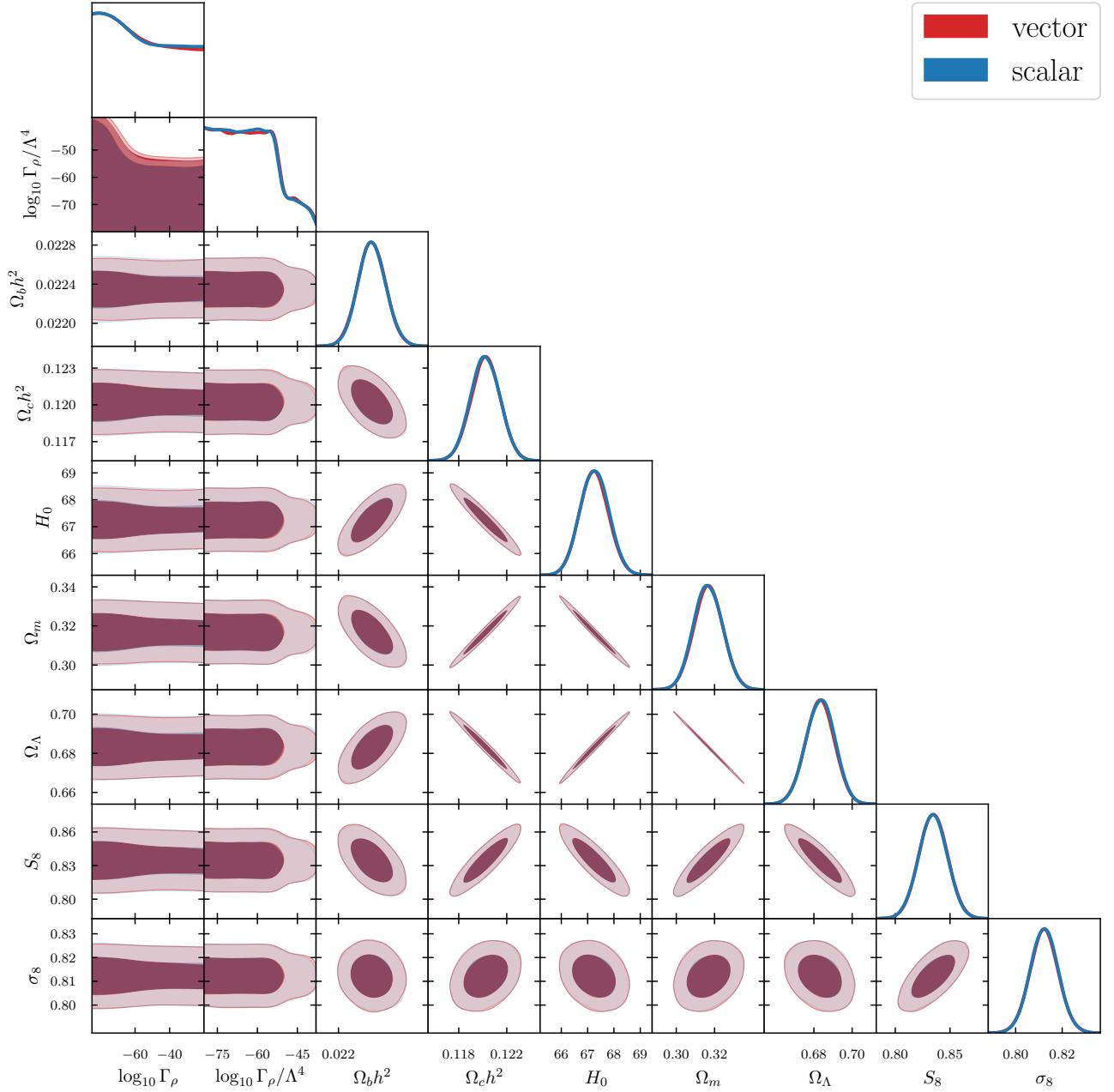


FIG. 19. Correlation between the main $\Lambda\text{CDM}\phi\nu_s$ model parameters, as inferred from `CosmoMC` for massless ν_s , for the vector (red) and scalar (blue) mediator models. The data sets Planck + Lensing + BAO + DES + Pantheon we consider here are described in the main text. The darker and lighter shaded regions correspond to the 68% and 95% C.L. intervals, respectively.

arXiv:1610.07957 [hep-ph].

- [11] N. Bernal, M. Dutra, Y. Mambrini, K. Olive, M. Peloso, and M. Pierre, “Spin-2 Portal Dark Matter,” *Phys. Rev. D* **97** no. 11, (2018) 115020, arXiv:1803.01866 [hep-ph].
- [12] T. R. Slatyer, “Les Houches Lectures on Indirect Detection of Dark Matter,” *SciPost Phys. Lect. Notes* **53** (2022) 1, arXiv:2109.02696 [hep-ph].
- [13] G. Weidenspointner, M. Varendorff, S. C. Kappadath, K. Bennett, H. Bloemen, R. Diehl, W. Hermsen, G. G.

- Lichti, J. Ryan, and V. Schönfelder, “The cosmic diffuse gamma-ray background measured with COMPTEL,” in *The Fifth Compton Symposium*, M. L. McConnell and J. M. Ryan, eds., vol. 510 of *American Institute of Physics Conference Series*, pp. 467–470. Apr., 2000.
- [14] D. J. Fixsen, E. S. Cheng, J. M. Gales, J. C. Mather, R. A. Shafer, and E. L. Wright, “The Cosmic Microwave Background spectrum from the full COBE FIRAS data set,” *Astrophys. J.* **473** (1996) 576, arXiv:astro-ph/9605054.

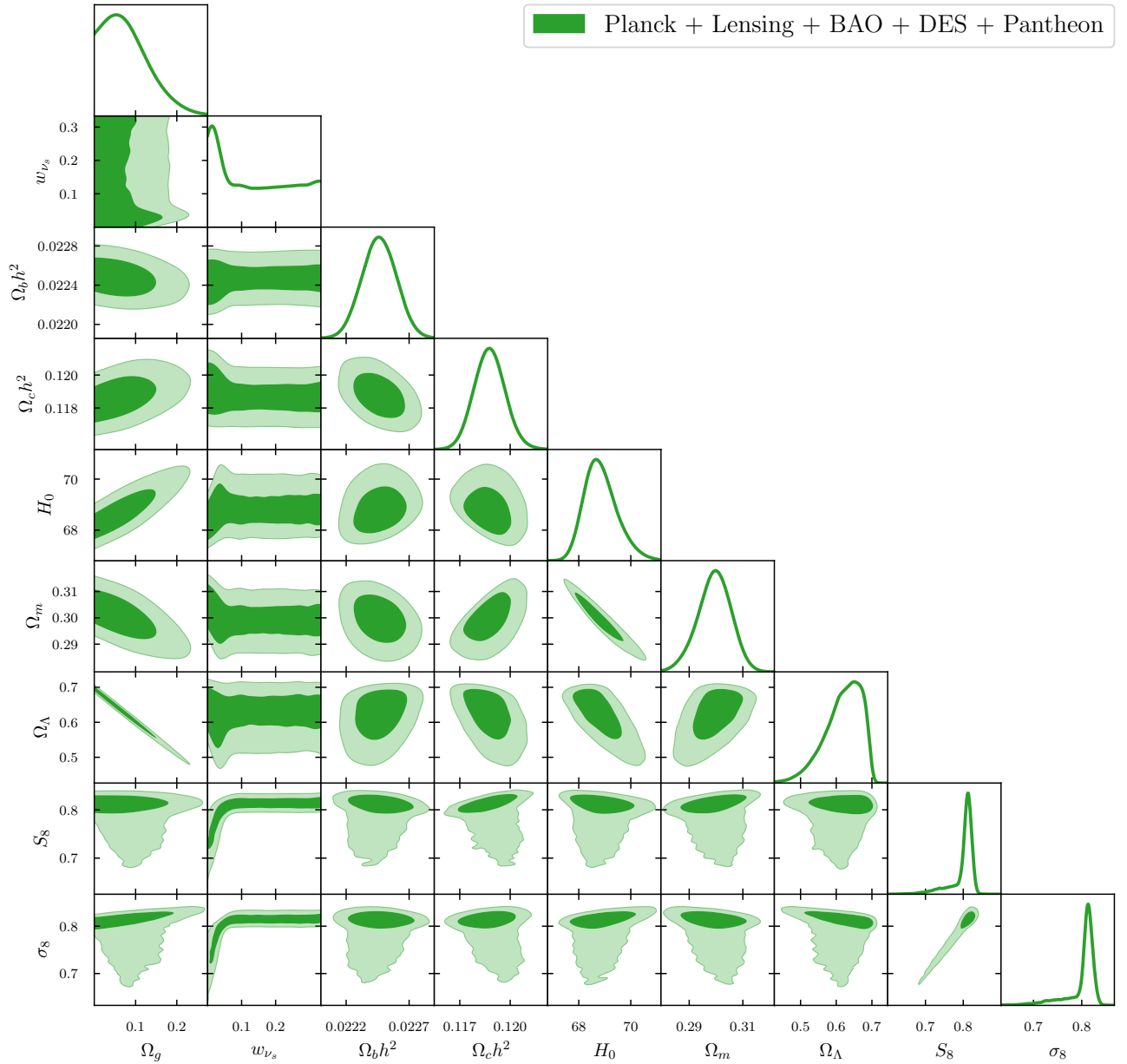


FIG. 20. Similar to Fig. 19, but for the massive ν_s case. These results apply to both the vector and scalar mediator models.

- [15] E. W. Kolb and M. S. Turner, *The Early Universe*, vol. 69. 1990.
- [16] K. J. Bae, A. Kamada, S. P. Liew, and K. Yanagi, “Light axinos from freeze-in: production processes, phase space distributions, and Ly- α forest constraints,” *JCAP* **01** (2018) 054, [arXiv:1707.06418](https://arxiv.org/abs/1707.06418) [hep-ph].
- [17] C. Dvorkin, T. Lin, and K. Schutz, “Making dark matter out of light: freeze-in from plasma effects,” *Phys. Rev. D* **99** no. 11, (2019) 115009, [arXiv:1902.08623](https://arxiv.org/abs/1902.08623) [hep-ph].
- [18] A. H. Guth, “The Inflationary Universe: A Possible Solution to the Horizon and Flatness Problems,” *Phys. Rev. D* **23** (1981) 347–356.
- [19] S. Perlmutter *et al.*, “Measurements of ω and λ from 42 high-redshift supernovae,” *The Astrophysical Journal* **517** no. 2, (Jun, 1999) 565. <https://dx.doi.org/10.1086/307221>.
- [20] A. G. Riess *et al.*, “Bvri light curves for 22 type ia supernovae,” *The Astronomical Journal* **117** no. 2, (Feb, 1999) 707. <https://dx.doi.org/10.1086/300738>.
- [21] N. Suzuki *et al.*, “The Hubble Space Telescope Cluster Supernova Survey. V. Improving the Dark-energy Constraints above $z > 1$ and Building an Early-type-hosted Supernova Sample,” *ApJ* **746** no. 1, (Feb., 2012) 85, [arXiv:1105.3470](https://arxiv.org/abs/1105.3470) [astro-ph.CO].
- [22] **Pan-STARRS1** Collaboration, D. M. Scolnic *et al.*, “The Complete Light-curve Sample of Spectroscopically Confirmed SNe Ia from Pan-STARRS1 and

- Cosmological Constraints from the Combined Pantheon Sample,” *Astrophys. J.* **859** no. 2, (2018) 101, [arXiv:1710.00845 \[astro-ph.CO\]](#).
- [23] D. Brout *et al.*, “The Pantheon+ Analysis: Cosmological Constraints,” *Astrophys. J.* **938** no. 2, (2022) 110, [arXiv:2202.04077 \[astro-ph.CO\]](#).
- [24] **Planck** Collaboration, N. Aghanim *et al.*, “Planck 2018 results. VI. Cosmological parameters,” *Astron. Astrophys.* **641** (2020) A6, [arXiv:1807.06209 \[astro-ph.CO\]](#). [Erratum: *Astron. Astrophys.* 652, C4 (2021)].
- [25] S. Vagnozzi, “New physics in light of the H_0 tension: An alternative view,” *Phys. Rev. D* **102** no. 2, (2020) 023518, [arXiv:1907.07569 \[astro-ph.CO\]](#).
- [26] A. Lewis, A. Challinor, and A. Lasenby, “Efficient computation of CMB anisotropies in closed FRW models,” *Astrophys. J.* **538** (2000) 473–476, [arXiv:astro-ph/9911177](#). <https://github.com/cmbant/CAMB>.
- [27] S. Chabanier, M. Millea, and N. Palanque-Delabrouille, “Matter power spectrum: from Ly α forest to CMB scales,” *Mon. Not. Roy. Astron. Soc.* **489** no. 2, (2019) 2247–2253, [arXiv:1905.08103 \[astro-ph.CO\]](#).
- [28] **Planck** Collaboration, N. Aghanim *et al.*, “Planck 2018 results. I. Overview and the cosmological legacy of Planck,” *Astron. Astrophys.* **641** (2020) A1, [arXiv:1807.06205 \[astro-ph.CO\]](#).
- [29] **eBOSS** Collaboration, B. Abolfathi *et al.*, “The Fourteenth Data Release of the Sloan Digital Sky Survey: First Spectroscopic Data from the Extended Baryon Oscillation Spectroscopic Survey and from the Second Phase of the Apache Point Observatory Galactic Evolution Experiment,” *Astrophys. J. Suppl. Ser.* **235** no. 2, (2018) 42, [arXiv:1707.09322 \[astro-ph.GA\]](#).
- [30] M. Ata *et al.*, “The clustering of the SDSS-IV extended Baryon Oscillation Spectroscopic Survey DR14 quasar sample: first measurement of baryon acoustic oscillations between redshift 0.8 and 2.2,” *Mon. Not. Roy. Astron. Soc.* **473** no. 4, (2018) 4773–4794, [arXiv:1705.06373 \[astro-ph.CO\]](#).
- [31] **DES** Collaboration, M. A. Troxel *et al.*, “Dark Energy Survey Year 1 results: Cosmological constraints from cosmic shear,” *Phys. Rev. D* **98** no. 4, (2018) 043528, [arXiv:1708.01538 \[astro-ph.CO\]](#).
- [32] W. Hu, “Structure formation with generalized dark matter,” *Astrophys. J.* **506** (1998) 485–494, [arXiv:astro-ph/9801234](#).
- [33] H. Kodama and M. Sasaki, “Cosmological Perturbation Theory,” *Prog. Theor. Phys. Suppl.* **78** (1984) 1–166.
- [34] C.-P. Ma and E. Bertschinger, “Cosmological perturbation theory in the synchronous and conformal Newtonian gauges,” *Astrophys. J.* **455** (1995) 7–25, [arXiv:astro-ph/9506072](#).
- [35] R. E. Lopez, S. Dodelson, R. J. Scherrer, and M. S. Turner, “Probing unstable massive neutrinos with current cosmic microwave background observations,” *Phys. Rev. Lett.* **81** (1998) 3075–3078, [arXiv:astro-ph/9806116](#).
- [36] M. Kaplinghat, R. E. Lopez, S. Dodelson, and R. J. Scherrer, “Improved treatment of cosmic microwave background fluctuations induced by a late decaying massive neutrino,” *Phys. Rev. D* **60** (1999) 123508, [arXiv:astro-ph/9907388](#).
- [37] W. Hu and S. Dodelson, “Cosmic Microwave Background Anisotropies,” *Ann. Rev. Astron. Astrophys.* **40** (2002) 171–216, [arXiv:astro-ph/0110414](#).
- [38] D. F. Mota, J. R. Kristiansen, T. Koivisto, and N. E. Groeneboom, “Constraining Dark Energy Anisotropic Stress,” *Mon. Not. Roy. Astron. Soc.* **382** (2007) 793–800, [arXiv:0708.0830 \[astro-ph\]](#).
- [39] T. Koivisto and D. F. Mota, “Dark energy anisotropic stress and large scale structure formation,” *Phys. Rev. D* **73** (2006) 083502, [arXiv:astro-ph/0512135](#).
- [40] A. Lewis and A. Challinor, “Weak gravitational lensing of the CMB,” *Phys. Rept.* **429** (2006) 1–65, [arXiv:astro-ph/0601594](#).
- [41] A. Lewis and S. Bridle, “Cosmological parameters from CMB and other data: A Monte Carlo approach,” *Phys. Rev. D* **66** (2002) 103511, [arXiv:astro-ph/0205436](#). <https://github.com/cmbant/CosmoMC>.
- [42] A. Gelman and D. B. Rubin, “Inference from Iterative Simulation Using Multiple Sequences,” *Statist. Sci.* **7** (1992) 457–472.
- [43] **Planck** Collaboration, N. Aghanim *et al.*, “Planck 2018 results. VIII. Gravitational lensing,” *Astron. Astrophys.* **641** (2020) A8, [arXiv:1807.06210 \[astro-ph.CO\]](#).
- [44] F. Beutler, C. Blake, M. Colless, D. H. Jones, L. Staveley-Smith, L. Campbell, Q. Parker, W. Saunders, and F. Watson, “The 6dF Galaxy Survey: Baryon Acoustic Oscillations and the Local Hubble Constant,” *Mon. Not. Roy. Astron. Soc.* **416** (2011) 3017–3032, [arXiv:1106.3366 \[astro-ph.CO\]](#).
- [45] A. J. Ross, L. Samushia, C. Howlett, W. J. Percival, A. Burden, and M. Manera, “The clustering of the SDSS DR7 main Galaxy sample – I. A 4 per cent distance measure at $z = 0.15$,” *Mon. Not. Roy. Astron. Soc.* **449** no. 1, (2015) 835–847, [arXiv:1409.3242 \[astro-ph.CO\]](#).
- [46] **BOSS** Collaboration, S. Alam *et al.*, “The clustering of galaxies in the completed SDSS-III Baryon Oscillation Spectroscopic Survey: cosmological analysis of the DR12 galaxy sample,” *Mon. Not. Roy. Astron. Soc.* **470** no. 3, (2017) 2617–2652, [arXiv:1607.03155 \[astro-ph.CO\]](#).
- [47] **DES** Collaboration, T. M. C. Abbott *et al.*, “Dark Energy Survey year 1 results: Cosmological constraints from galaxy clustering and weak lensing,” *Phys. Rev. D* **98** no. 4, (2018) 043526, [arXiv:1708.01530 \[astro-ph.CO\]](#).
- [48] **DES** Collaboration, E. Krause *et al.*, “Dark Energy Survey Year 1 Results: Multi-Probe Methodology and Simulated Likelihood Analyses,” [arXiv:1706.09359 \[astro-ph.CO\]](#).
- [49] E. Di Valentino, O. Mena, S. Pan, L. Visinelli, W. Yang, A. Melchiorri, D. F. Mota, A. G. Riess, and J. Silk, “In the realm of the Hubble tension—a review of solutions,” *Class. Quant. Grav.* **38** no. 15, (2021) 153001, [arXiv:2103.01183 \[astro-ph.CO\]](#).
- [50] E. Abdalla *et al.*, “Cosmology intertwined: A review of the particle physics, astrophysics, and cosmology associated with the cosmological tensions and anomalies,” *JHEAp* **34** (2022) 49–211, [arXiv:2203.06142 \[astro-ph.CO\]](#).
- [51] E. Di Valentino, A. Melchiorri, and J. Silk, “Planck evidence for a closed Universe and a possible crisis for cosmology,” *Nature Astron.* **4** no. 2, (2019) 196–203, [arXiv:1911.02087 \[astro-ph.CO\]](#).

- [52] W. Handley, “Curvature tension: evidence for a closed universe,” *Phys. Rev. D* **103** no. 4, (2021) L041301, [arXiv:1908.09139 \[astro-ph.CO\]](#).
- [53] S. Vagnozzi, E. Di Valentino, S. Gariazzo, A. Melchiorri, O. Mena, and J. Silk, “The galaxy power spectrum take on spatial curvature and cosmic concordance,” *Phys. Dark Univ.* **33** (2021) 100851, [arXiv:2010.02230 \[astro-ph.CO\]](#).
- [54] J. Lesgourgues and S. Pastor, “Massive neutrinos and cosmology,” *Phys. Rept.* **429** (2006) 307–379, [arXiv:astro-ph/0603494](#).
- [55] **Planck** Collaboration, P. A. R. Ade *et al.*, “Planck 2013 results. XVI. Cosmological parameters,” *Astron. Astrophys.* **571** (2014) A16, [arXiv:1303.5076 \[astro-ph.CO\]](#).
- [56] W. L. Freedman, “Cosmology at a Crossroads,” *Nature Astron.* **1** (2017) 0121, [arXiv:1706.02739 \[astro-ph.CO\]](#).
- [57] L. Verde, T. Treu, and A. G. Riess, “Tensions between the Early and the Late Universe,” *Nature Astron.* **3** (7, 2019) 891, [arXiv:1907.10625 \[astro-ph.CO\]](#).
- [58] E. Di Valentino *et al.*, “Snowmass2021 - Letter of interest cosmology intertwined II: The hubble constant tension,” *Astropart. Phys.* **131** (2021) 102605, [arXiv:2008.11284 \[astro-ph.CO\]](#).
- [59] M. G. Dainotti, B. De Simone, T. Schiavone, G. Montani, E. Rinaldi, and G. Lambiase, “On the Hubble constant tension in the SNe Ia Pantheon sample,” *Astrophys. J.* **912** no. 2, (2021) 150, [arXiv:2103.02117 \[astro-ph.CO\]](#).
- [60] M. G. Dainotti, B. De Simone, T. Schiavone, G. Montani, E. Rinaldi, G. Lambiase, M. Bogdan, and S. Ugale, “On the Evolution of the Hubble Constant with the SNe Ia Pantheon Sample and Baryonic Acoustic Oscillations: A Feasibility Study for GRB-Cosmology in 2030,” *Galaxies* **10** no. 1, (2022) 24, [arXiv:2201.09848 \[astro-ph.CO\]](#).
- [61] A. L. Lenart, G. Bargiacchi, M. G. Dainotti, S. Nagataki, and S. Capozziello, “A Bias-free Cosmological Analysis with Quasars Alleviating H_0 Tension,” *Astrophys. J. Suppl.* **264** no. 2, (2023) 46, [arXiv:2211.10785 \[astro-ph.CO\]](#).
- [62] G. Bargiacchi, M. G. Dainotti, S. Nagataki, and S. Capozziello, “Gamma-Ray Bursts, Quasars, Baryonic Acoustic Oscillations, and Supernovae Ia: new statistical insights and cosmological constraints,” [arXiv:2303.07076 \[astro-ph.CO\]](#).
- [63] M. G. Dainotti, G. Bargiacchi, M. Bogdan, S. Capozziello, and S. Nagataki, “Reduced uncertainties up to 43% on the Hubble constant and the matter density with the SNe Ia with a new statistical analysis,” [arXiv:2303.06974 \[astro-ph.CO\]](#).
- [64] G. Bargiacchi, M. G. Dainotti, and S. Capozziello, “Tensions with the flat Λ CDM model from high-redshift cosmography,” [arXiv:2307.15359 \[astro-ph.CO\]](#).
- [65] E. O. Colgáin, M. M. Sheikh-Jabbari, R. Solomon, G. Bargiacchi, S. Capozziello, M. G. Dainotti, and D. Stojkovic, “Revealing intrinsic flat Λ CDM biases with standardizable candles,” *Phys. Rev. D* **106** no. 4, (2022) L041301, [arXiv:2203.10558 \[astro-ph.CO\]](#).
- [66] M. Malekjani, R. M. Conville, E. O. Colgáin, S. Pourojaghi, and M. M. Sheikh-Jabbari, “Negative Dark Energy Density from High Redshift Pantheon+ Supernovae,” [arXiv:2301.12725 \[astro-ph.CO\]](#).
- [67] K. C. Wong *et al.*, “H0LiCOW – XIII. A 2.4 per cent measurement of H_0 from lensed quasars: 5.3σ tension between early- and late-Universe probes,” *Mon. Not. Roy. Astron. Soc.* **498** no. 1, (2020) 1420–1439, [arXiv:1907.04869 \[astro-ph.CO\]](#).
- [68] A. G. Riess *et al.*, “A Comprehensive Measurement of the Local Value of the Hubble Constant with 1 km s^{-1} Mpc $^{-1}$ Uncertainty from the Hubble Space Telescope and the SHOES Team,” *Astrophys. J. Lett.* **934** no. 1, (2022) L7, [arXiv:2112.04510 \[astro-ph.CO\]](#).
- [69] S. A. Uddin *et al.*, “Carnegie Supernova Project-I and -II: Measurements of H_0 using Cepheid, TRGB, and SBF Distance Calibration to Type Ia Supernovae,” [arXiv:2308.01875 \[astro-ph.CO\]](#).
- [70] H. Hildebrandt *et al.*, “KiDS+VIKING-450: Cosmic shear tomography with optical and infrared data,” *Astron. Astrophys.* **633** (2020) A69, [arXiv:1812.06076 \[astro-ph.CO\]](#).
- [71] **KiDS** Collaboration, M. Asgari *et al.*, “KiDS-1000 Cosmology: Cosmic shear constraints and comparison between two point statistics,” *Astron. Astrophys.* **645** (2021) A104, [arXiv:2007.15633 \[astro-ph.CO\]](#).
- [72] C. Heymans *et al.*, “KiDS-1000 Cosmology: Multi-probe weak gravitational lensing and spectroscopic galaxy clustering constraints,” *Astron. Astrophys.* **646** (2021) A140, [arXiv:2007.15632 \[astro-ph.CO\]](#).
- [73] **DES** Collaboration, T. M. C. Abbott *et al.*, “Dark Energy Survey Year 3 results: Cosmological constraints from galaxy clustering and weak lensing,” *Phys. Rev. D* **105** no. 2, (2022) 023520, [arXiv:2105.13549 \[astro-ph.CO\]](#).
- [74] **HSC** Collaboration, C. Hikage *et al.*, “Cosmology from cosmic shear power spectra with Subaru Hyper Suprime-Cam first-year data,” *Publ. Astron. Soc. Jap.* **71** no. 2, (2019) 43, [arXiv:1809.09148 \[astro-ph.CO\]](#).
- [75] R. C. Nunes and S. Vagnozzi, “Arbitrating the S8 discrepancy with growth rate measurements from redshift-space distortions,” *Mon. Not. Roy. Astron. Soc.* **505** no. 4, (2021) 5427–5437, [arXiv:2106.01208 \[astro-ph.CO\]](#).
- [76] E. Di Valentino *et al.*, “Cosmology Intertwined III: $f\sigma_8$ and S_8 ,” *Astropart. Phys.* **131** (2021) 102604, [arXiv:2008.11285 \[astro-ph.CO\]](#).
- [77] **Kilo-Degree Survey, Dark Energy Survey** Collaboration, T. M. C. Abbott *et al.*, “DES Y3 + KiDS-1000: Consistent cosmology combining cosmic shear surveys,” [arXiv:2305.17173 \[astro-ph.CO\]](#).
- [78] J. E. Cavanaugh and A. A. Neath, “The Akaike information criterion: Background, derivation, properties, application, interpretation, and refinements,” *Wiley Interdisciplinary Reviews: Computational Statistics* **11** no. 3, (2019) e1460.
- [79] A. A. Neath and J. E. Cavanaugh, “The bayesian information criterion: background, derivation, and applications,” *Wiley interdisciplinary reviews. Computational statistics* **4** no. 2, (2012) 5.
- [80] M. R. Gangopadhyay, M. Sami, and M. K. Sharma, “Phantom dark energy as a natural selection of evolutionary processes âlagenetic algorithm and cosmological tensions,” [arXiv:2303.07301 \[astro-ph.CO\]](#).
- [81] R. R. Caldwell, M. Kamionkowski, and N. N. Weinberg, “Phantom energy and cosmic doomsday,” *Phys. Rev. Lett.* **91** (2003) 071301, [arXiv:astro-ph/0302506](#).

- [82] H. Bondi and T. Gold, “The Steady-State Theory of the Expanding Universe,” *MNRAS* **108** (Jan., 1948) 252.
- [83] F. Hoyle, “A New Model for the Expanding Universe,” *MNRAS* **108** (Jan., 1948) 372.
- [84] R.-G. Cai, Z.-K. Guo, S.-J. Wang, W.-W. Yu, and Y. Zhou, “No-go guide for the Hubble tension: Late-time solutions,” *Phys. Rev. D* **105** no. 2, (2022) L021301, [arXiv:2107.13286 \[astro-ph.CO\]](#).
- [85] R.-G. Cai, Z.-K. Guo, S.-J. Wang, W.-W. Yu, and Y. Zhou, “No-go guide for late-time solutions to the Hubble tension: Matter perturbations,” *Phys. Rev. D* **106** no. 6, (2022) 063519, [arXiv:2202.12214 \[astro-ph.CO\]](#).
- [86] S. Gariazzo, E. Di Valentino, O. Mena, and R. C. Nunes, “Late-time interacting cosmologies and the Hubble constant tension,” *Phys. Rev. D* **106** no. 2, (2022) 023530, [arXiv:2111.03152 \[astro-ph.CO\]](#).
- [87] C. Krishnan, E. O. Colgáin, M. M. Sheikh-Jabbari, and T. Yang, “Running Hubble Tension and a H0 Diagnostic,” *Phys. Rev. D* **103** no. 10, (2021) 103509, [arXiv:2011.02858 \[astro-ph.CO\]](#).
- [88] C. Krishnan, R. Mohayaee, E. O. Colgáin, M. M. Sheikh-Jabbari, and L. Yin, “Does Hubble tension signal a breakdown in FLRW cosmology?,” *Class. Quant. Grav.* **38** no. 18, (2021) 184001, [arXiv:2105.09790 \[astro-ph.CO\]](#).
- [89] J. M. Cline, M. Puel, and T. Toma, “Boosted dark matter from a phantom fluid,” [arXiv:2308.01333 \[hep-ph\]](#).
- [90] G. P. Lepage, “A New Algorithm for Adaptive Multidimensional Integration,” *J. Comput. Phys.* **27** (1978) 192.
- [91] G. P. Lepage, “Adaptive multidimensional integration: VEGAS enhanced,” *J. Comput. Phys.* **439** (2021) 110386, [arXiv:2009.05112 \[physics.comp-ph\]](#).
- [92] O. F. Piattella, *Lecture Notes in Cosmology*. UNITEXT for Physics. Springer, Cham, 2018. [arXiv:1803.00070 \[astro-ph.CO\]](#).
- [93] G. Barenboim, J. Z. Chen, S. Hannestad, I. M. Oldengott, T. Tram, and Y. Y. Y. Wong, “Invisible neutrino decay in precision cosmology,” *JCAP* **03** (2021) 087, [arXiv:2011.01502 \[astro-ph.CO\]](#).
- [94] K. Ichiki, M. Oguri, and K. Takahashi, “WMAP constraints on decaying cold dark matter,” *Phys. Rev. Lett.* **93** (2004) 071302, [arXiv:astro-ph/0403164](#).
- [95] W. Hu, D. Scott, N. Sugiyama, and M. J. White, “The Effect of physical assumptions on the calculation of microwave background anisotropies,” *Phys. Rev. D* **52** (1995) 5498–5515, [arXiv:astro-ph/9505043](#).
- [96] J. Lesgourgues and T. Tram, “The Cosmic Linear Anisotropy Solving System (CLASS) IV: efficient implementation of non-cold relics,” *JCAP* **2011** no. 09, (Sep, 2011) 032–032, [arXiv:1104.2935 \[astro-ph.CO\]](#).